CHEMICAL REVIEWS

Review

Charge Transport in Nanoparticle Assemblies

Amir Zabet-Khosousi, and Al-Amin Dhirani

Chem. Rev., **2008**, 108 (10), 4072-4124 • DOI: 10.1021/cr0680134 • Publication Date (Web): 24 September 2008

Charge Transport in Nanoparticle Assemblies

Amir Zabet-Khosousi and Al-Amin Dhirani*

Lash Miller Chemical Laboratories, University of Toronto, Ontario M5S 3H6, Canada

Received October 22, 2007

Contents

* Corresponding author e-mail: adhirani@chem.utoronto.ca.

1. Introduction

Nanoparticles (NPs) are commonly referred to as "artificial atoms",[1] as they can exhibit atomic-like behaviors. The analogy is highlighted by a result that, just like atoms, electronic energy levels of NPs can be quantized due to fundamental properties of electrons, namely, the discrete nature of electron charge, the wave-like nature of electron propagation, and the quantum mechanical nature of spin. As the size of an NP is reduced, its intrinsic capacitance decreases, and the energy required to charge the particle by an electron increases correspondingly. For example, for an isolated spherical NP of radius R, the single-electron charging energy, E_C, is given by $E_C \approx e^2/2C \approx e^2/8\pi\varepsilon_0\varepsilon_r R$, where C is the NP capacitance, ε_0 is the permittivity of vacuum, and ε_r is the dielectric constant of the NP surroundings. Taking $R \approx 10$ nm, E_C is ~72 meV, higher than the energy provided by thermal fluctuations at room temperature ($k_BT \approx 25$ meV, where k_B is Boltzmann's constant and T is temperature). As a result, the spectrum of NP charging energies can appear discrete as the NP is charged one electron at a time.

Since sizes of NPs are comparable with characteristic wavelengths of electrons, electrons can also exhibit a discrete, atomic-like spectrum of energies due to quantum confinement.[2,3] Energy level spacing, δ, in a metallic NP is given by $4E_F/3N$, where E_F is the Fermi energy of the bulk material (assumed to be the same for the NP) and N is the number of

10.1021/cr0680134 CCC: $71.00
Published on Web 09/24/2008

Amir Zabet-Khosousi received his B.Sc. degree in chemistry from Sharif University of Technology, Tehran, Iran, in 2003. He then moved to Canada, where he started graduate studies in chemical physics under the supervision of Prof. Al-Amin Dhirani at the University of Toronto. He obtained his M.Sc. degree in 2004 and now is a Ph.D. candidate. His research explores electronic properties of nanoscale structures, particularly nanoparticles and single molecules, using break junctions. Amir is a recipient of several awards and fellowships, notably the Silver Medal of International Chemistry Olympiad in 2000, Ontario Graduate Scholarship in 2007, and Ontario Postdoc Fellowship in 2008. He has also been selected as the Distinguished Student of the Year, Iran, 2004.

Al-Amin Dhirani obtained his B.Sc. in physics from University of Alberta in 1986, his M.Sc. in quantum field theory from McGill University in 1991 (Prof. Lam, supervisor), and his Ph.D. in experimental surface physics from University of Chicago in 1996 (Prof. Guyot-Sionnest, supervisor). He pursued postdoctoral studies involving experiment and theory in atom optics at MIT (Prof. Pritchard, supervisor) from 1996−1998. In 1999, he accepted an assistant professorship in the Chemistry Department at University of Toronto, and in 2004, he was promoted to associate professor. He is also cross-appointed to the Physics and Electrical Engineering Departments at University of Toronto. His current research focuses on electronic properties of nanostructured architectures. His awards include Hulda and Maurice Rothschild Fellowship (University of Chicago, 1995), American Physical Society Travel Award (1996), James Franck Symposium Dissertation Award (University of Chicago, 1996), Natural Science and Engineering Research Council Postdoctoral fellowship (MIT, 1997), and the Premier's Research Excellence Award (University of Toronto, 2000).

atoms in the NP. Therefore, δ depends on the NP volume and increases as the NP size is reduced: $\delta \approx R^{-3}$.[2] For semiconducting NPs—also known as "quantum dots" (QDs)—the energy gap between valence and conduction bands depends strongly on the size as well as the shape of NPs.[4] Considering a simple electron-in-a-box model, the band gap of quantum dots scales approximately as R^{-2}.[5]

The analogy between NPs and natural atoms is extended by the fact that both can serve as building blocks for hierarchical assembly of macroscopic structures. That is, just as atoms can be assembled to form various traditional materials, NPs can be assembled to form so-called "artificial materials". Properties of materials are determined by nature, coupling, and arrangements of their individual building blocks ("atoms"). Properties of individual NPs depend on the size, shape, and composition of NPs and, therefore, are tunable using recent advances in chemical synthetic methods. NP couplings can be varied through inter-NP spacing or through the use of molecules to cap or cross-link NPs. Arrangement of NPs is controllable through the assembly process and can exhibit various degrees of order/disorder. A key flexibility of artificial materials is that synthesis of the building blocks is separated from the assembly process: NPs with desired properties can be synthesized by wet chemical methods and subsequently organized into assemblies. Control over properties afforded by NP assemblies is illustrated particularly well by charge transport phenomena. In any mechanism for charge transport in materials in which matter is located at certain sites, key model parameters are site energy levels, intersite couplings, and site spatial distribution (including effects of disorder), all of which can be controlled by the above-mentioned physical parameters. Site energies are determined by NP energy levels, which are controllable through NP size and chemical nature. Intersite coupling and site spatial distribution can be controlled by the assembly procedure. Site spatial disorder can be controllably introduced in otherwise ordered systems by varying NP size distribution. By varying these parameters, assemblies can exhibit a broad range of charge transport behaviors from Arrhenius to hopping to metallic behavior.[6] It is likely that assemblies can exhibit superconductivity as well, since individual NPs can be superconducting provided energy level spacings are not too large. Superconductivity has been observed in 9 nm Al NPs,[7,8] 6 nm NbC NPs,[9] 8 nm Nb NPs,[10] and 20 nm Pb NPs.[11] This control and inherent flexibility in composition and structure afforded by these materials has led to important advances in our understanding of fundamental charge transport phenomena, such as metal−insulator transitions and variable-range hopping (sections 4.4 and 4.5, respectively). In addition, optimizing their properties has led to applications in a number of fields. These range from exotic applications such as conductance switching (transistors)[12] and information-storage[13] to proof-of-principle demonstration of chemical/biological sensing,[14−21] surface-enhanced Raman scattering,[22] conductive coatings,[23] and catalysis.[5,24]

Understanding properties of these materials—and particularly their relationship to structure and composition—is critical if we are to manipulate and optimize their function. In recent decades, there has been a rapidly growing body of literature exploring properties of NP assemblies, improving our understanding of the basic science governing the properties of these materials and providing hope for their applications. Many of these studies have been discussed in articles reviewing synthesis and characterization,[25−33] as well as photophysical[34−42] and thermodynamical[43] properties of both NPs[5,44] and their assemblies.[45−56] In the present article, we provide a complementary review of studies focusing on charge transport through NP assemblies. One of the challenges associated with studies in this area of research is that it involves concepts from several disciplines, including chemistry, materials science, engineering (particularly electronics), and physics and/or physical chemistry.[57] To address

this issue and to make this review more accessible, we also provide a detailed background of physical concepts and experimental methods underpinning these studies.

2. Preparation of Nanoparticle Assemblies

2.1. Assembly Components

2.1.1. Nanoparticles (NPs)

Techniques for preparing NPs have advanced rapidly over recent decades. Synthesis of metal or semiconducting NPs has been the subject of several reviews.[5,25−33,44] NPs are now readily synthesized in chemical laboratories, and many types are commercially available. NPs can be produced with tunable sizes and shapes by methods that are physical (e.g., vapor deposition, laser ablation) or chemical (e.g., metal salt reduction, sol−gel process, micelles, pyrolysis) in nature.[5,33] This review mainly focuses on studies involving chemically synthesized NPs, typically in a size range of ∼1−25 nm. We use the term nanoparticles to refer to such particles.

The most common method for synthesizing metal NPs involves reduction of metal salts (notably $HAuCl_4$, $AgNO_3$, $AgClO_4$, $Ag(CH_3COO)$, $PtCl_4$, $PdCl_4$, $Cu(CH_3COO)_2$, $CoCl_2$, $Co(CH_3COO)_2$, $Ni(CH_3COO)_2$, and Ni(acetylacetone)$_2$)[33] in one-phase or two-phase solutions in the presence of a stabilizer. An example of one-phase NP synthesis involves the reduction of aqueous $HAuCl_4$ by citrate.[58,59] This approach yields NPs that are ∼5 nm or greater in diameter and are electrostatically stabilized in solution by surface charges. In a two-phase method, described by Brust et al.,[60] aqueous metal salts are transferred to a toluene solution containing long-chain alkylammonium bromide surfactants. After isolation of the organic phase, capping molecules (typically alkanethiols) are added to the solution, and subsequently, an aqueous solution of reducing agents is added to nucleate NPs. Resulting NPs have a size range of ∼1−3 nm, are stabilized by a shell of alkanethiolate capping ligands, and can be isolated as a powder. In the absence of thiolate capping groups, the two-phase method yields larger NPs (∼5−8 nm) stabilized with the alkylammonium bromide surfactants. These NPs are only stable in solution and cannot be isolated or redispersed.[61]

Many variations of the metal salt reduction method have been developed for synthesizing NPs of Au, Ag, Pd, Pt, Cu, Co, and Ni.[33] By varying reaction parameters, e.g., concentration and/or structure of capping molecules or reducing agent, the size, shape, and polydispersity of NPs can be controlled. Capping molecules are discussed in the next section. Examples of reducing agents include $NaBH_4$, hydrazine, sodium citrate, potassium bitartarate, dimethyl formamide, ascorbic acid, superhydrides, amines, alcohols, and polyalcohols.[33] Weak reducing agents, such as citrate, tend to yield small NPs, whereas strong reducing agents, such as formamide, tend to yield large NPs.[33] Other methods of synthesizing NPs include sequestering and subsequently reducing metal ions (such as Cu^{2+}, Pd^{2+}, Pt^{2+}, Ni^{2+}, Fe^{3+}, Mn^{2+}, Au^{3+}, and Ru^{3+}) in dendrimers,[31] reducing metal ions in reverse micelles,[5,52] and thermally decomposing metal−carbonyl compounds (e.g., $Co_2(CO)_8$ and $Fe(CO)_5$) in the presence of surfactants (e.g., tributylphosphine).[62]

An established procedure for synthesizing semiconductor NPs is based on the pyrolysis of organometallic precursors in a hot coordinating solvent (usually a mixture of long-chain alkylphosphines, alkylphosphine oxides, alkylamines, etc.) as described by Bawendi and co-workers.[63] For example, CdSe NPs can be synthesized by quickly injecting a mixture of selenium and dimethylcadmium dissolved in trioctylphosphine (TOP) into hot (∼300 °C) trioctylphosphine oxide (TOPO) and subsequently allowing the NPs to grow at a reduced temperature (∼250 °C). This procedure has been used to synthesize a variety of binary semiconducting NPs (ME where M = Zn, Cd, Hg and E = S, Se, Te or M = In, Ga and E = As, P).[28]

It is often desirable to reduce the NP size distribution because polydispersity can increase disoerder of assemblies and broaden ensemble behavior. In size-selective precipitation, a postsynthetic method commonly used to narrow NP size distributions,[28,63,64] a nonsolvent (miscible with the original dispersing solvent) is gradually added to an NP solution. At certain average solvent polarities, larger NPs are no longer soluble in the solvent mixture and precipitate, narrowing the size distributions of both precipitate and supernatant. "Monodisperse" NPs with a size distribution of ≤5%, that is, ±1 lattice constant for a 5 nm NP,[28] can be obtained by redissolving the precipitate and repeatedly using the size-selective precipitation/redissolution steps. The size distribution of NPs during size-selective precipitation has been investigated by optical absorption[63] and mass spectroscopy.[64] Other techniques for narrowing the dispersity of NP size include heating,[65−67] etching,[68,69] annealing,[70] and chromatography.[71−76]

NP surface functionalization can be modified by a ligand-substitution reaction.[28,77] This reaction involves exposing capped-NPs to a stirred solution of alternate capping ligands for a period of time and then precitiating the NPs. Hostetler et al.[78] have performed NMR and IR studies of the dynamics and mechanism of ligand-substitution reaction using Au NPs and various alkanethiols. They have observed that the rate of ligand substitution depends on concentrations of both incoming (R′−SH) and outgoing (R−SH) ligands, and that the rate is higher when outgoing capping ligands have shorter alkanes. On the basis of these observations, they have proposed an associative mechanism in which the incoming ligand penetrates the capping shell in order to participate in the substitution reaction

$$x(\mathrm{R'SH}) + (\mathrm{RS})_m\mathrm{NP} \rightarrow x(\mathrm{RSH}) + (\mathrm{RS})_{m-x}(\mathrm{R'S})_x\mathrm{NP} \quad (1)$$

where x and m are the numbers of incoming and outgoing ligands, respectively. Ligand substitution has been used extensively to generate both metallic and semiconducting NPs with a wide range of chemical functionalities (see below).[41,79−82]

2.1.2. Molecules

Molecules—either as capping ligands or cross-linkers—play an important role in NP assemblies. During the synthesis of NPs, capping ligands can control NP size and can stabilize NPs against aggregation. For example, molecules that bind strongly to the NP cores or that provide great steric hindrance bulk can slow down the rate of NP growth resulting in small NPs. The molecules can influence physical and chemical properties of individual NPs, including solubility, reactivity, stability, and optoelectronic structure.[5] They can also play a key role in NP assemblies by serving as cross-linkers or spacers, thereby controlling interaction between NPs. By using molecules with functionalities (e.g., redox-activity or

biorecognition), the corresponding functionality can be incorporated into an assembly. The important role of molecules in influencing charge transport through NP assemblies is discussed in detail in sections 4−6.

Essentially any mono- or bifunctional molecule that has a tendency to bind with NP core material can be used as a capping ligand or cross-linker, respectively. The most common binding group is thiol used with Au or Ag NPs.[83] Examples of other NP-binding group combinations are as follows: for Au and Ag, amines, phosphanes, phosphines, carboxylates, dithiocarbamates, and xanthates;[44] for Pt and Pd, amines and isocyanides;[33] for Co and Ni, amines, phosphines, phosphine oxides, and carboxylic acids;[62] and for semiconductor NPs, phosphines, phosphine oxides, phosphites, phosphates, amines, and pyridines.[28] The molecules can have a variety of structural motifs and may include saturated or conjugated hydrocarbons,[81,82] polymers or oligomers,[84−86] oligonucleotides (e.g., DNA[87−89]), polyelectrolytes,[90−94] electrochemical-active derivatives (e.g., viologen[91,95−98] and ferrocene[99−107]), dendrimers,[31,108−111] and supramolecules (e.g., bipyridinium cyclophanes[112−115]).

2.2. Assembly Methods

NP films have been prepared and studied in 1D, 2D, or 3D structures. Assemblies are generally prepared from the "bottom-up", where the film structure is controlled via assembly components and assembly method.[28,45−53,56] The latter is as influential as the former in determining material properties. For example, depending on assembly method employed, NP asemblies can exhibit a high degree of order (superlattices), short-range order, or a high degree of disorder, with each type of assembly exhibiting properties that are correspondingly different. Here, we review a number of methods that have been commonly employed in studies involving charge transport through NP assemblies.

2.2.1. Drop-Casting

When a solution of NPs is spread on a solid substrate by drop-casting (or spin-coating), upon evaporation of the solvent, long-range dispersion forces between the NPs or between the NPs and the substrate cause the NPs to self-organize into mono- or multilayer structures.[116] The substrate can be chosen to suit the measurements envisioned. For example, graphite, silicon−nitride substrates, or carbon-coated grids are commonly used for scanning tunneling microscopy (STM) and transmission electron microscopy (TEM). Glass or silicon/silicon-oxide substrates with pre-patterned electrodes can be used for optical or conductivity measurements, where transparent or insulating substrates are required, respectively.

TEM images of drop-cast films of NPs on silicon−nitride substrates typically exhibit well-packed NPs with domain sizes ranging from a few hundred nanometers to several microns. Domain sizes have been shown to depend on NP size distribution, NP concentration, and solvent dewetting or volatility. Korgel et al.,[117,118] using small-angle X-ray scattering (SAXS) and TEM, have observed that size-polydisperse dodecanethiolate-capped Ag NPs with an average diameter of ∼4−8 nm and a size dispersion of >10% did not form ordered superlattices upon solvent evaporation. Monodisperse NPs obtained by size-selective precipitation, on the other hand, condensed into ordered assemblies. Lin et al.[119] have studied the influence of NP concentration and solvent dewetting on superlattice formation. When solutions of dodecanethiolate-capped 5.5 nm Au NPs with narrow size distribution (±5%) were drop-cast on silicon−nitride substrates, the sizes of NP domains depended strongly on the NP concentration (Figure 1). At a low NP concentration of 1.0×10^{12} mL^{-1}, NPs formed isolated domains (Figure 1a). The domains grew with increasing concentration (Figure 1b) and formed compact structures at a concentration of 1.2×10^{13} mL^{-1} (Figure 1c). At higher concentrations, films formed multilayer regions rather than a monolayer with long-range order. In the presence of excess dodecanethiol, NPs did form superlattices with long-range order extending over several microns (Figure 1d). The authors proposed that the excess thiol reduced the evaporation rate of the solvent[120,121] and prevented the solvent from dewetting the surface. The evaporation rate of the solvent can also be modified by adding a second solvent with a lower vapor pressure. Bawendi and co-workers[28] have reported that structures of NP films prepared by drop-casting solutions of 8 nm CdSe NPs capped with TOP/TOPO in mixed hexane/octane solvents depended strongly on the solvent composition. A more volatile solvent mixture (95% hexane/5% octane) produced glassy (disordered) NP arrays, while a less volatile solvent mixture (95% octane/5% hexane) resulted in ordered NP superlattices.

Drop-casting permits control over inter-NP surface-to-surface separation via choices of capping ligands. For example, Murray and co-workers[122,123] have studied drop-cast films of 2.2 nm Au NPs, encapsulated with a series of alkanethiolates with $n = 4-8$, 10, 12, 16, where n is the number of carbon atoms. Densities of these films decreased with increasing n in correspondence with increasing inter-NP separation. The authors observed a ratio of ∼1.2 between inter-NP separations and lengths of single alkanethiolate chains. That is, values of inter-NP separation were considerably smaller than twice the lengths of the alkanethiolate chains, suggesting intercalation of NP ligands. It is also possible to change the inter-NP separation after film formation by ligand substitution. Andres et al.[116] have shown that when films of dodecanethiolate-capped 3.7 nm Au NPs (prepared by spin-coating) were immersed in an acetonitrile solution of 2.0-nm-long aryl dithiol [1,4-di(4-thiophenylethynyl)-2-ethylbenzene], the aryl dithiols displaced the dodecanethiolate capping groups and gave rise to monolayers of covalently linked NPs. The average inter-NP separation increased from 1.3 to 1.7 nm because of the ligand substitution. Similar treatment with 2.2-nm-long aryl diisonitrile [1,4-di(4-isocyanophenylethynyl)-2-ethylbenzene] caused an increase in inter-NP separation from 1.3 to 1.9 nm.

Inter-NP separation can also be modified by annealing NP solids at temperatures well-below the melting temperature of the NP cores, as shown, for example, by Redmond and co-workers.[124−127] They used drop-cast films of 3.8 nm $CoPt_3$ NPs stabilized by 1-adamantanecarboxylic acid and hexadecylamine ligands. TEM images of the as-prepared films exhibited an average inter-NP separation of ∼2.3−2.5 nm. As films were annealed under reducing conditions (5% H_2, 95% N_2, for 1 h at 80−150 °C), film conductivity increased and transitioned from insulating to metallic (i.e., conductivity remained finite upon decreasing temperature to 3 K) (see section 4.4). The authors proposed that these changes in electronic properties of the films were due to a reduction in the inter-NP separation upon thermal annealing. Thermogravimetric, X-ray diffraction (XRD), TEM, and

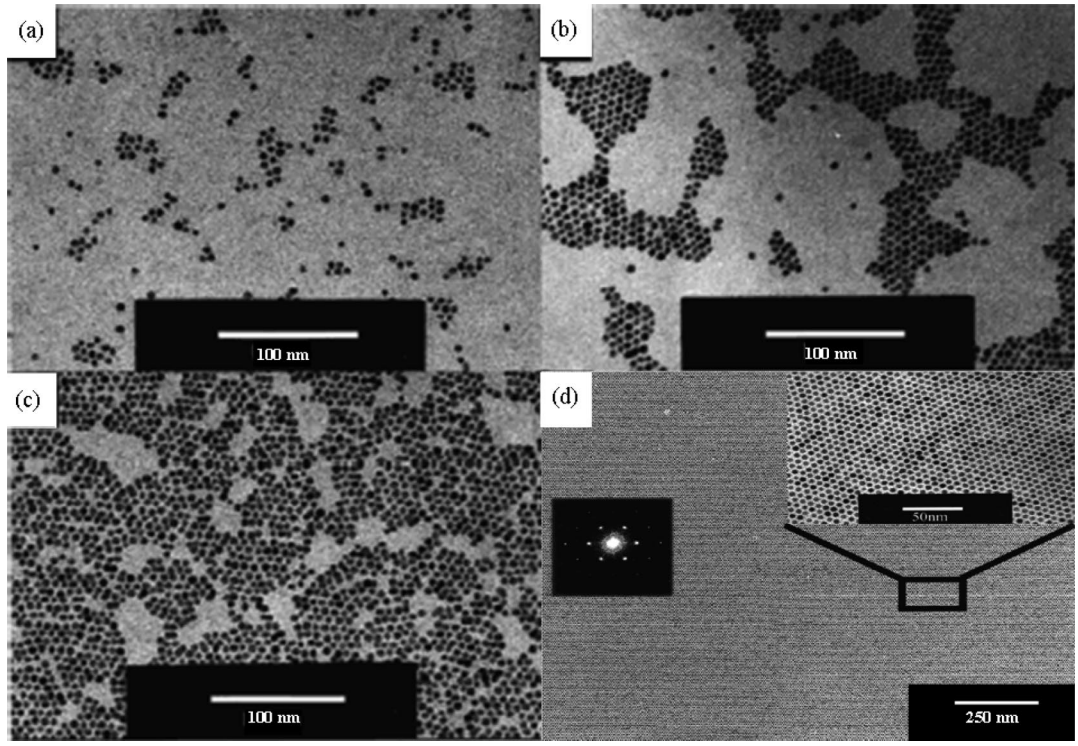

Figure 1. NP patterns formed by depositing 10 μL toluene solutions of dodecanethiolate-capped, 5.5 nm Au NPs on 3 mm × 4 mm silicon nitride substrates. NP concentrations were as follows: (a) 1.0×10^{12}, (b) 4.8×10^{12}, and (c) 1.2×10^{13} mL^{-1}. (d) An NP monolayer exhibiting long-range order formed by depositing 10 μL of 1.2×10^{13} mL^{-1} Au NPs in toluene/dodecanethiol mixture with a thiol volume fraction of 6.3×10^{-3}. An upper right inset shows a magnified view (scale bar = 50 nm). A left inset shows a diffraction pattern obtained by Fourier transforming a portion of the TEM image. Reprinted with permission from ref 119 (Jaeger's group). Copyright 2001 American Chemical Society (http://dx.doi.org/10.1021/jp0102062).

solubility studies of the annealed films showed that the $CoPt_3$ NPs did not exhibit significant oxidation, ligand desorption, or sintering at temperatures below ~200 °C.[125,128] Similar thermal annealing methods have been also employed to reduce inter-NP separation in films of Co,[129] CdSe,[130,131] and PbSe NPs.[132,133]

2.2.2. Langmuir Methods

Langmuir methods can be used to prepare a monolayer of ordered NPs over macroscopic dimensions at an air−water interface. Typically, a solution of NPs with hydrophobic capping groups is first deposited on water in a Teflon (polytetrafluoroethylene, PTFE) trough. Because of their hydrophobic capping, the NPs form a submonolayer film on the surface. Then, the NPs are slowly compressed using a moveable barrier while surface pressure is measured. Heath et al.[134] have employed Langmuir methods to study monolayers of alkanethiolate-capped Au and Ag NPs. They have investigated the effects of NP size, size distribution, and capping ligand length on phase behavior of the monolayers and have found that NPs with sizes of ~2−4 nm capped by ligands with $n \leq 12$ (where n is the number of methylene groups in the alkane chain) can be compressed into 2D close-packed phases (Figure 2). The long-range order of these phases depends on the NP size distribution and the nature of the solvent: narrower distributions and less volatile solvents (e.g., heptane vs hexane) usually lead to increased order. A benefit of the Langmuir approach is that it offers precise control over inter-NP separation. For example, Chen[135] has shown that inter-NP separations of Langmuir monolayers of butanethiolate- or pentanethiolate-capped Au NPs were tunable from >1.0 nm to ~0.8 or 0.9 nm, at which point monolayers began to collapse.

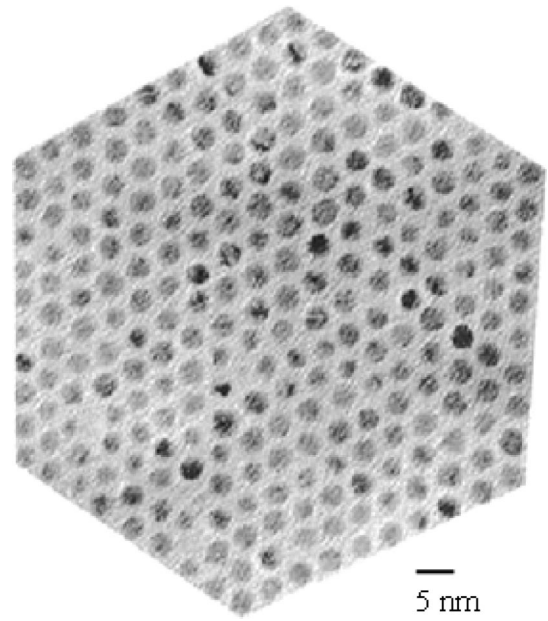

Figure 2. Portion of a TEM micrograph of a film of 2.8 nm dodecanethiolate-capped Ag NPs extracted from a Langmuir trough at a pressure just below that required to collapse the 2D film into a 3D film. Reprinted with permission from ref 134 (Heath's group). Copyright 1997 American Chemical Society (http://dx.doi.org/10.1021/jp9611582).

Monolayers from the Langmuir trough can be transferred onto solid substrates for further characterizations. A Langmuir−Blodgett film is prepared by vertically dipping and withdrawing a substrate in the monolayer at a given surface pressure.[136] A Langmuir−Schaefer film is prepared by bringing a substrate close to the Langmuir monolayer

parallel to the surface of the trough. When the substrate is briefly contacted with the surface, the monolayer is transferred from the surface to the substrate.[137−142] A number of groups have reported use of microcontact printing[143,144] to transfer monolayers of Au,[145−147] Fe_2O_3,[148] or Co[149] NPs from water surfaces onto various solid substrates. In this approach, a uniform monolayer of close-packed NPs is first drop-cast on a water surface and is then transferred intact to a patterened polydimethylsiloxane (PDMS) stamp by the Langmuir−Schaefer method. NP monolayers can then be printed on (both hydrophobic and hydrophilic) substrates by bringing the PDMS stamp in conformal contact with the substrate. This method can be used to produce patterned mono- or multilayered arrays of close-packed NPs.

2.2.3. Cross-Linking Precipitation

Brust et al.[61] have shown using two approaches that 3D assemblies of covalently linked NPs can be produced by directly mixing solutions of NPs and linker molecules. In a first approach, they synthesized ∼2.2 nm diameter Au NPs in the presence of alkanedithiols, instead of alkanethiols, producing precipitates of alkanedithiol-linked NPs. In the second approach, they synthesized Au NPs in the absence of any thiols and obtained larger NPs ∼8 nm in diameter. These "thiol-free" NPs were stable in solution but could not be isolated and redispersed. Upon addition of alkanedithiols, the NPs precipitated as cross-linked networks that could be isolated from the solution and dried as powders. They pressed the dry precipitates into small pellets, whose thicknesses were controllable by adjusting the initial concentration of NPs in the solution. Müller et al.[150,151] prepared films of cross-linked NPs by vacuum-filtering solutions of NP aggregates through nanoporous filter membranes. The NP films could be handled, flexed, or cut into strips.

Leibowitz et al.[152] demonstrated that ligand exchange can also be used to prepare cross-linked NP assemblies. They mixed solutions of alkanethiolate-capped NPs (e.g., decanethiolate-capped Au NP) and excess dithiol cross-linkers (e.g., 1,9-nonanedithiols) and immersed a solid substrate into the mixture. Exchange between the ligand shell of NPs and free dithiol linkers eventually led to precipitation of cross-linked NPs on the surface. Film thickness could be controlled via immersion time. Infrared reflectance spectroscopy of films of cross-linked NPs showed a reduction or an absence of methyl stretching bands, confirming replacement of monothiolate ligands by dithiol linkers. TEM images of the films prepared on carbon-coated copper grids revealed disordered and porous structures.

2.2.4. Stepwise Self-Assembly

In this method, 3D assemblies of linked-NPs are constructed by stepwise immersion of substrates in various solutions. The versatility of this method allows assembly of materials on various substrates, exploiting a variety of interactions such as electrostatic, covalent bonding, hydrogen bonding, or coordinate bonding.[46,153,154] Brust et al.[155,156] were among the first to prepare covalently cross-linked NP-molecule assemblies. They first functionalized the surface of a glass substrate using a monolayer of 3-(mercaptopropyl)trimethoxysilane (MPTMS) and thereby generated a "sticky" surface for the subsequent deposition of Au NPs. Next, they immersed the functionalized substrate into a solution of thiol-free 6 nm Au NPs for ∼12 h to obtain a

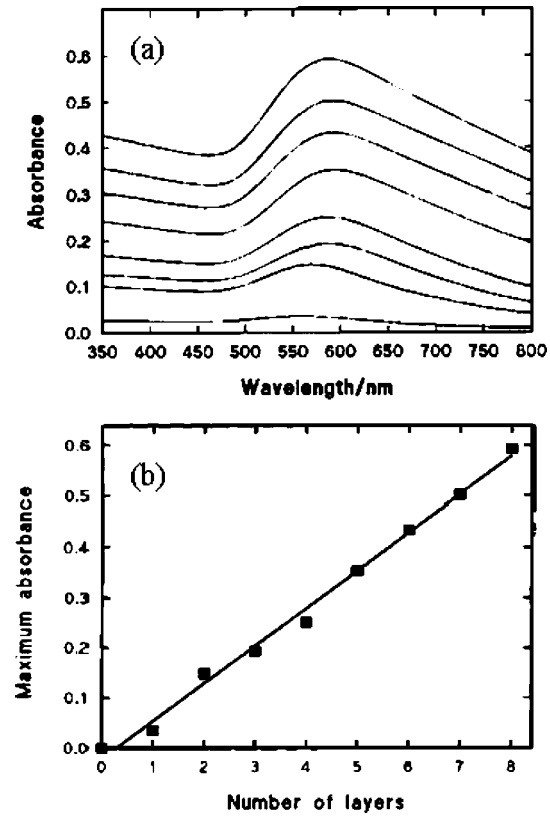

Figure 3. (a) UV/vis spectra of the first eight layers of ∼6 nm Au NPs linked with 1,9-nonanedithiol deposited on glass. (b) Maximum absorbance value (between 550 and 600 nm) of the UV/vis spectra vs the number of deposition cycles. Reprinted with permission from ref 156 (Brust's group). Copyright 1998 American Chemical Society (http://dx.doi.org/10.1021/la980557g).

self-assembled layer of immobilized NPs. They immersed the substrate, after rinsing it with solvents, into a solution of α,ω-alkanedithiols ($HS(CH_2)_nSH$, with $n = 6, 9, 12$) that acted as linkers enabling further deposition of NPs. By repeating immersions into NP and dithiol solutions and rinsing between immersions, they were able to increase the amount of deposited material. A variety of linker molecules with different lengths, structures, and end-groups, including amine, alcohol, isocyanide, and dithiocarbamate, have been used.[12,13,157−167] Exposure times to linker molecule and NP solutions reported in these studies are usually in the ranges of ∼10−15 and ∼30−120 min, respectively.

Growth of NP films can be monitored using UV/vis spectroscopy, scanning electron microscopy (SEM), atomic force microscopy (AFM), or conductance spectroscopy. Brust et al.,[156] for example, have studied UV/vis spectra of the 1,9-nonanedithiol-linked ∼6 nm Au NP films (Figure 3a). They observed that the maximum absorbance of the films (between wavelengths of 550 and 600 nm) increased almost linearly with the number of deposition cycles (Figure 3b), indicating that an approximately constant amount of NPs was added per cycle.

Musick et al.[158] have studied the structure of films of Au and Ag NPs linked with 2-mercaptoethanol ($HSCH_2CH_2OH$) and 2-mercaptoethylamine ($HSCH_2CH_2NH_2$) using SEM and AFM. SEM and AFM images of the films revealed porous and disordered film structures (Figure 4). AFM imaging after the first deposition cycle showed that initially isolated NPs were dispersed over the substrate (Figure 4a). With increasing number of cycles, imaging showed that newly deposited NPs were attached either to previously deposited NPs, forming

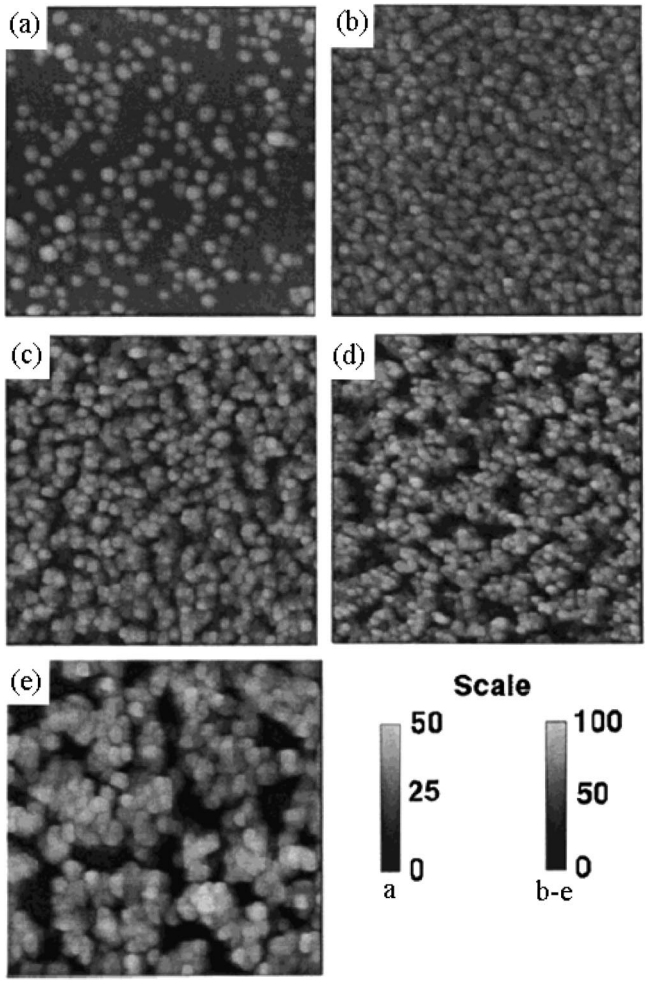

Figure 4. AFM images of $HSCH_2CH_2OH$-linked ~12 nm Au NP films: (a) 1, (b) 3, (c) 5, (d) 7, and (e) 11 deposition cycle(s). Reprinted with permission from ref 158 (Natan's group). Copyright 2000 American Chemical Society (http://dx.doi.org/10.1021/cm990714c).

clusters of linked NPs, or to uncovered regions of the substrate, seeding new clusters (Figure 4 parts b−e). At the so-called percolation threshold, the clusters of linked NPs have grown sufficiently large that they span the film. Well above the percolation threshold, the film exhibits characteristics of bulk cross-linked NP materials (see section 4.4.2).

Snow et al.[160] have studied the roles of linker molecules and immersion time in stepwise self-assembly. They used solutions of hexanethiolate-capped 1.8 nm Au NPs, α,ω-alkanedithiols ($HS(CH_2)_nSH$, $n = 6, 8, 9, 12$) in chloroform, and SiO_2 substrates prepatterned with interdigitated array (IDA) of Au electrodes (see section 3.1.1). Film growth was monitored via changes in current passing between the Au electrodes. Figure 5a shows results for 1,8-octanedithiol-linked NP films. Current generally increased after the NP immersion step but partially dropped after the dithiol immersion step, possibly due to transfer of some NPs from the film to the solution. This in turn suggests that there is an optimum time for immersion in linker solution. The immersion time should be long enough to allow linkers to replace capping groups but not too long to remove the NPs from the film. They found that 2 min dithiol immersion time was a good compromise under their experimental conditions. Figure 5b shows current as a function of time during alternate immersions into NP and dithiol and finally into thiol solutions. During exposures to the NP solution, the current

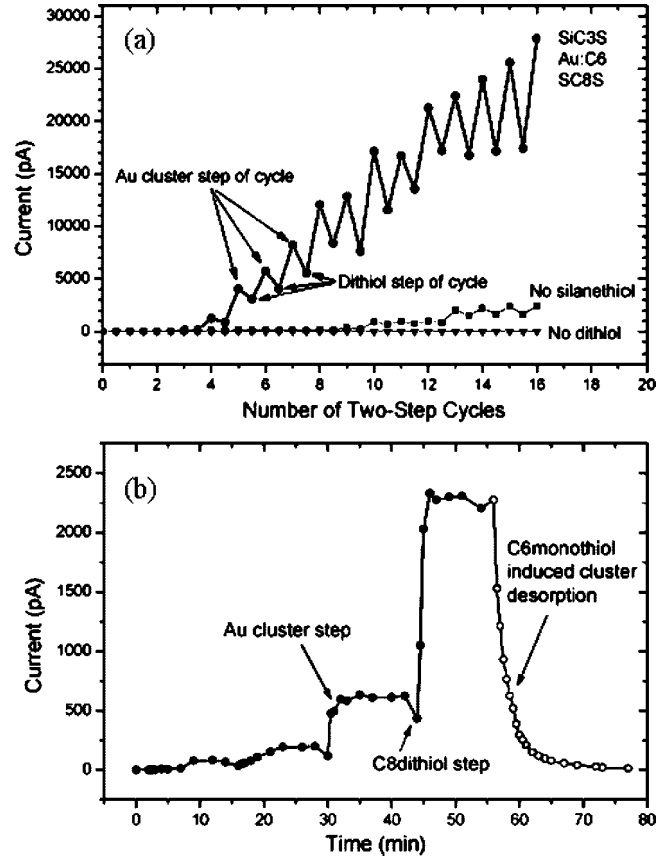

Figure 5. (a) Changes in current after each alternating deposition of hexanethiolate-capped Au NPs and 1,8-octanedithiol linkers onto IDA electrodes. (b) Current vs time as a sample was alternately immersed in solutions of 1,8-octanedithiol and hexanethiolate-capped Au NPs (●) and finally in a solution of hexanethiol (○). Reprinted with permission from ref 160 (Snow's group). Copyright 2002 the Royal Society of Chemistry (http://dx.doi.org/10.1039/b108859a).

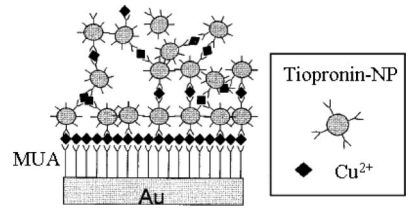

Figure 6. Schematic of an NP multilayer film formed via carboxylate−Cu^{2+}−carboxylate linkage. Reprinted with permission from ref 169 (Murray's group). Copyright 2000 American Chemical Society (http://dx.doi.org/10.1021/la000287d).

increased during the first 2 min to a value that remained relatively constant afterward, indicating that 2 min was sufficient for NP self-assembly. Finally, upon immersing the film into a solution of hexanethiol, the current rapidly dropped to a value approaching zero, suggesting that the NPs detached from the film.

Murray and co-workers[168−173] have demonstrated a method of stepwise self-assembly based on ligand/ion/ligand linkage. They prepared Au NPs capped with a mixture of alkanethiolates and ω-mercapto-carboxylic acids via ligand-substitution reactions.[170] They showed that these NPs can be cross-linked via Cu^{2+}− or Zn^{2+}−carboxylate coordination. Figure 6 shows a schematic of an NP multilayer film. A gold substrate was first functionalized with a monolayer of mercaptoundecanoic acid (MUA). Then the substrate was alternately immersed in an ethanolic solution of $Cu(ClO_4)_2$

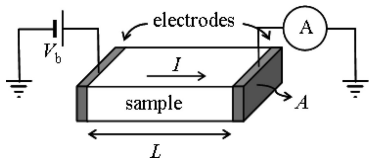

Figure 7. Schematic of a two-probe electrode configuration.

and a basic methanolic solution of tiopronin ($HSCH_2CONHCH_2COOH$)-capped NPs. Substrates were immersed for 5 min and were rinsed with solvents between immersions. Infrared external reflectance spectroscopy[169] and UV/vis spectroscopy confirmed growth of the film.[171]

Electrostatic attraction between positively and negatively charged assembly components can also be used to self-assemble NP films in a stepwise fashion.[153] For example, Liu et al.[90] have prepared NP films on a gold-coated glass substrate by alternatingly immersing the substrate into aqueous solutions of (i) 4.8 nm Au NPs capped with cationic polymers (poly(diallyldimethylammonium chloride)) and (ii) anionic polymers (Poly S-119). They monitored the growth of the NP films by ellipsometry and observed a linear increase of the film thickness with the number of immersion cycles. A feature afforded by this method is that the time-scale to self-assemble a film is on the order of several minutes, much shorter than the ~24 h required to self-assemble a film using covalent interactions.

2.2.5. Comparison of Assembly Methods

Cross-linking precipitation and stepwise self-assembly methods generally produce films that are more stable than those produced using drop-casting and Langmuir methods. In the former, the NPs are held together by strong covalent, coordinative, or ionic bonds, whereas in the latter, NPs interact via relatively weak van der Waals and dispersion forces.[46] Methods based on NP cross-linking are very versatile, enabling assemblies of NPs linked with a variety of molecules or supramolecules such as polymers or oligomers,[84−86] DNA,[87−89] polyelectrolyes,[90−94] viologen,[95−98] ferrocene,[100−103] dendrimers,[108−111] and cyclophanes.[112−115] On the other hand, long-range order is typically not achievable by these methods. Methods using nonlinked NPs (i.e., drop-casting or Langmuir) permit a more ordered film structure.[47] A combination of these methods can be used to produce ordered assemblies of cross-linked NPs. For example, Andres et al.[116] have prepared close-packed arrays of cross-linked Au NPs using a two-step process. They first spin-coated a solution of dodecanethiolate-capped Au NPs onto a substrate and then immersed the substrate in a solution of aryl dithiols to displace dodecanethiolate capping groups (see section 2.2.1). Chen[174] has prepared 2D arrays of cross-linked Au NPs using a Langmuir method by first dispersing a solution of octanethiolate-capped 5 nm Au NPs in hexane onto the water surface, then dispersing a solution of 4,4′-thiobisbenzenedithiol in CH_2Cl_2 on the surface, and finally compressing the film. TEM images of the NP monolayers transferred onto TEM grids exhibited long-range order.

3. Transport Measurements

3.1. Two-Probe Electrode Configuration

In this simplest configuration, a bias voltage (V_b) is applied across two electrodes attached to a sample and the resulting current (I) is measured. According to Ohm's law—often valid for many materials at low voltages and for metals—current is linearly proportional to voltage:

$$I = gV_b = V_b/R \quad (2)$$

where g is the conductance and R is the resistance. Conductivity (σ) is calculated using the relationship

$$\sigma = gL/A \quad (3)$$

where A is the cross-sectional area of the film and L is the distance between electrodes (Figure 7).

For materials not exhibiting ohmic $I-V$ characteristics, commonly differential conductance, dI/dV, is determined as a function of voltage. This can be done either by numerically differentiating the $I-V$ data or by using a lock-in amplifier (LIA). In the LIA approach, a modulation voltage ($\tilde{V}$),

$$\tilde{V} = V_o \cos 2\pi ft \quad (4)$$

is added to the bias voltage, where V_o is a small amplitude, f is the modulation frequency, and t is time. The total voltage, $V_b + \tilde{V}$, is applied across the sample, resulting in a current with both time-independent and sinusoidally varying time-dependent components (direct current, dc, and alternating current, ac, respectively). The total current is then converted or amplified to a proportional voltage (see below) and input into the LIA. The LIA measures the component of the input signal at the frequency f (or some multiple of f if desired) and provides a dc output voltage proportional to $dI/dV(V_b)$ as follows. The current is a function of the total voltage applied to the sample, i.e., $I = I(V_b + \tilde{V})$. Expanding about V_b yields the following:

$$I(V_b + \tilde{V}) = I(V_b) + \frac{dI}{dV}(V_b)\cdot\tilde{V} + \cdots = I(V_b) + \frac{dI}{dV}(V_b)\cdot V_o \cos 2\pi ft + \cdots \quad (5)$$

An LIA's output, measured at frequency f, is proportional to the coefficient of $\cos 2\pi ft$; therefore, apart from known amplification factors, the LIA output is given by $dI/dV(V_b)\cdot V_o$. Harmonic frequencies of $2f$, $3f$,... yield the second, third,... derivatives of I versus V, respectively.

Current may be converted to a voltage by passing the current through an ohmic resistor (known as a gain resistor, R_G) and measuring the voltage (V_{out}) generated across the resistor:

$$V_{out} = IR_G \quad (6)$$

V_{out} can be measured using a multimeter, an oscilloscope, an LIA, an analog-to-digital converter and a computer, etc. A problem associated with simply using a resistor is that voltage measuring devices usually have finite input resistances, which can affect the measurement. To solve this problem, current−voltage converters based on operational amplifiers can be used. Ideal operational amplifiers have infinite input resistances, resulting in V_{out}'s not being affected by measurement circuit.

3.1.1. Interdigitated Array of Electrodes

Interdigitated array (IDA) electrodes (Figure 8) consist of several electrode finger pairs, typically microns in dimension. IDA electrodes are fabricated on insulating substrates such

as Si/SiO_2, glass, or quartz, using photolithographic patterning[175] and are commercially available.

IDA electrodes are suitable for determining conductivities of thin films. Film conductivity, σ, can be calculated using the following equation,[176]

$$\sigma = \frac{L}{(2N-1)lh} g \quad (7)$$

where L is the spacing between electrodes, N is the number of finger pairs, l is the overlapping length of electrodes, h is the film thickness (less than that of IDA electrodes), and g is conductance. Spacing between electrodes is typically a few tens of microns, which is much larger than the sizes of NPs. The large electrode areas yield improved reproducibility by providing averaged film characteristics.[160]

3.1.2. Nanometer-Spaced Electrodes

Nanometer-spaced electrodes are used in studies involving single molecules and NPs or chains of a few NPs. Electrodes with separations of ~10−100 nm can be fabricated using electron-beam lithography and metal evaporation. The electrodes include an adhesion layer of Cr or Ti a few nanometers thick and an overlayer of metal, typically Au, a few tens of nanometers thick.[129,160,177−187] Electrodes with a gap spacing of <10 nm can be created by a number of methods such as mechanical breaking[188−191] or electromigration.[126,166,192−204] In the latter method, a pair of thick electrodes separated by a large gap is fabricated with the aid of shadow masks or lithography. Next, a thin layer of metal that bridges the gap is deposited, resulting in a structure that resembles a fuse. Application of a gradually increasing current induces atomic motion, which in turn gives rise to a controlled break in the metal bridge and a gap as small as a few nanometers in width. The electromigration break-junction approach provides a remarkably simple and robust means for fabricating nanometer-spaced electrodes.

An advantage offered by nanometer-spaced electrodes is that fewer NPs are required to bridge the electrodes, and they enable fabrication of single-NP devices.[177,178,181−183,192−195,197,201] There are also a number of challenges associated with these methods. For instance, the device-to-device variations can be large and require statistical analysis of a large number of samples. In addition, the contact between the electrode and the NP (usually through a linking molecule) should be robust and reproducible. In many cases, atomic-scale details of metal−molecule contacts are not well-known. For a review of recent advances in fabrication of nanometer-spaced electrodes, see ref 205.

3.1.3. Electrodes Deposited Post-Film Fabrication

Electrodes can be deposited on NP films after preparation using sputter-coating,[206] vapor-deposition,[157,161,162,164,165] silver paint contacting,[150,156,159,163,207] indium soldering,[12,13]

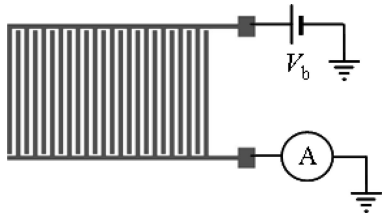

Figure 8. Schematic of IDA electrodes.

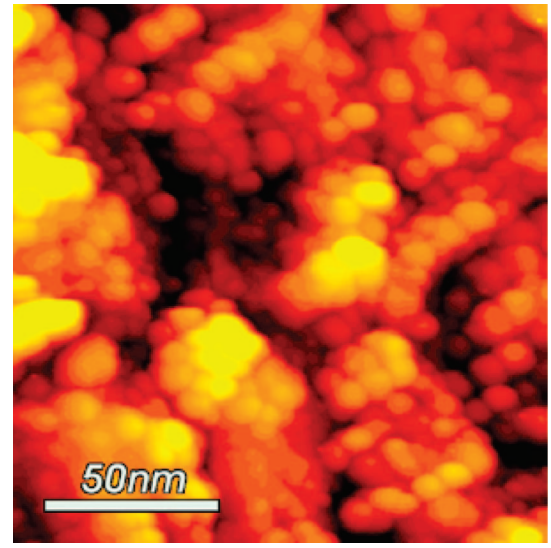

Figure 9. STM image of a multilayer film of ~5 nm Au NPs linked with 1,4-butanedithiol prepared on a doped-silicon/silicon-oxide substrate. Tip bias and current set point are −1.2 V and 0.1 nA, respectively. Reprinted with permission from ref 12 (Dhirani's group). Copyright 2005 American Chemical Society (http://dx.doi.org/10.1021/jp051282y).

or electrodeposition.[159] These methods are relatively simple and cost-effective and do not require high-resolution fabrication equipment. They can be used to probe $I-V$ or $dI/dV-V$ characteristics of the samples at various temperatures. However, these methods may give rise to variations in sample−electrode interfaces due to diffusion of electrode material into the sample or due to interface heating, depending on the method. Therefore, it is important to distinguish the role of contacts from that of the sample. An approach for eliminating the contributions from contact resistances is described in section 3.3.

3.1.4. Scanning Tunneling Microscopy and Its Variations

In scanning tunneling microscopy, a bias voltage is applied between a sharp conductive tip and a noninsulating sample, and the two are brought into close proximity of each other. At a sufficiently small tip−sample separation (a few nm or less), a detectable tunneling current flows (see section 4.1). The tunneling current depends exponentially on the tip−sample separation. For example, using typical metals as tip and sample, in vacuum a ~1 Å increase in the tip−sample separation decreases the current by ~1 order of magnitude. This sensitive dependence of tunneling current on separation forms the basis for imaging in the scanning tunneling microscope (STM).[208] Figure 9 shows an example STM image of a multilayer film of ~5 nm Au NPs prepared on a doped-silicon/silicon-oxide substrate.

STM can also be used to perform spectroscopy. In scanning tunneling spectroscopy, the tip is usually held at a fixed position with respect to the sample, and current, differential conductance, etc. are measured as a function of the tip−sample bias. Spectroscopic data provide information about local electronic characteristics of the sample such as density of states.[138,139] Variations of imaging and spectroscopic modes have also been developed. For example, it is possible to perform spectroscopy as a function of voltage at different locations on a surface and to plot the spectroscopic data as a series of images at different voltages.

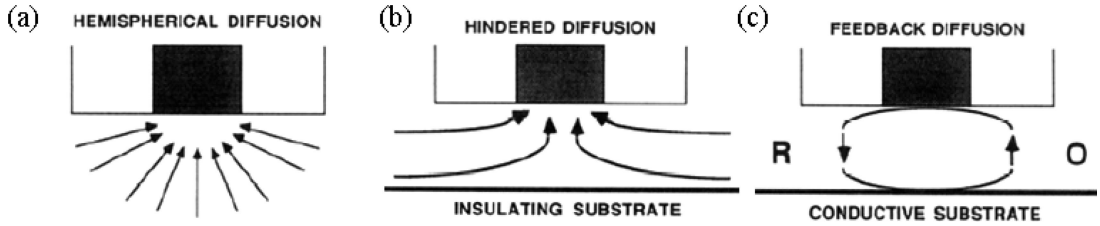

Figure 10. Basic principles of SECM: (a) far from the substrate, diffusion leads to a steady-state current; (b) near an insulating substrate, hindered diffusion leads to a current suppression; (c) near a conducting substrate, feedback diffusion leads to a current enhancement. Reprinted with permission from ref 222 (Bard's group). Copyright 1990 American Chemical Society.

A conductive-probe atomic force microscope (CP-AFM)[209] provides another means to study electrical properties of materials. In an atomic force microscope (AFM), a sharp tip attached to an end of a flexible cantilever is brought close to a sample. A force (F) between the tip and the sample surface leads to a deflection of the cantilever (z). The deflection is measured and used to determine F according to Hooke's law,

$$F = -kz \tag{8}$$

where k is the spring constant of the cantilever. Cantilever deflection is typically detected by reflecting a laser beam off the cantilever and monitoring the changes in position of the reflected beam using photodiodes. The force can be used to generate a feedback signal to control tip−sample separation. In CP-AFM, the tip is coated with a conducting film (usually Au). A bias applied between the conductive tip and the sample generates a measured current as in STM. However, CP-AFM differs from STM in that the position of the tip is controlled using feedback based on force.[210] CP-AFMs have been used to measure conductances of a variety of systems, including Au NP multilayers,[211] semiconducting NPs,[212] carbon nanotubes,[213] and molecular self-assembled monolayers.[214−219]

Scanning electrochemical microscopy (SECM)[220] permits surface characterization of a substrate immersed in a solution of redox-active electrolyte. In SECM, an ultramicroelectrode (UME) typically serves as the tip, and its position with respect to a substrate can be varied. Voltage is applied between the tip and a reference electrode, and current is measured between the tip and a counterelectrode. In contrast with tunneling current, SECM current arises from redox of species at the UME tip. When the tip is far from the substrate, the current is driven by the diffusion of redox species between the solution and the tip (Figure 10a). When the tip is brought close to the substrate, the vicinity and the nature of the substrate perturbs the current. An insulating substrate can hinder diffusion of redox species toward the tip and thereby reduce the current (Figure 10b): the closer the tip is to the substrate, the smaller is the current. In contrast, a conducting substrate can increase the current by regenerating a portion of the reacted species at its surface. The regenerated species can react again at the tip and increase the tip current (Figure 10c). Therefore, SECM offers a means for determining the insulating or conducting nature of substrates and can be used to probe lateral conductivity of the substrates.[142,221]

3.2. Three-Terminal Electrode Configuration

Figure 11 is a schematic illustration of a three-terminal electrode configuration with source, drain, and gate electrodes. Source and drain electrodes are directly connected to the sample and enable measurements of current (or

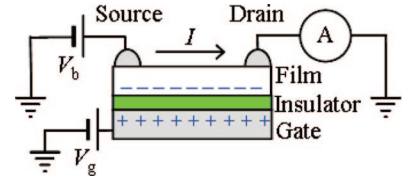

Figure 11. Schematic of a three-terminal electrode configuration.

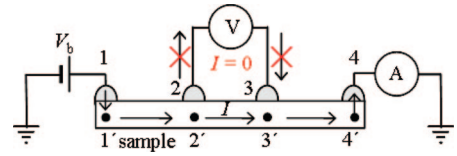

Figure 12. Schematic of a four-probe electrode configuration.

differential conductance) as a function of bias voltage, V_b. The third gate electrode is separated from the sample via an intervening insulating layer. A voltage, V_g, applied to the gate electrode creates an electric field across the insulating layer that can affect current flowing between the source and the drain. The insulating layer should be sufficiently thick so as to prevent significant leakage current. Typical examples of gate electrodes are doped silicon[12,13,178,180,187] and aluminum,[195] both of which have oxides that can serve as excellent insulators. The three-terminal electrode configuration is analogous to that in conventional field-effect transistors and can be used to implement electronically actuated conductance changes. These applications are discussed in section 6.2.1.

3.3. Four-Probe Electrode Configuration

As discussed earlier in section 3.1.3, a challenge associated with standard $I-V$ measurements is that the measured total resistance includes contributions from both the sample and electrode−sample contacts. Electrode−sample contacts generate resistances that are in series and, therefore, sum with the sample resistance. In many cases of interest, contact resistances are significant and must be distinguished from the sample resistance. This can be done using a four-probe measurement technique as illustrated in Figure 12. The overall resistance measured between electrodes 1 and 4 is $R_{14} = R_{11'} + R_{1'4'} + R_{44'}$, where $R_{1'4'}$ is the resistance of the sample between points 1′ and 4′, and $R_{11'}$, $R_{22'}$, $R_{33'}$, and $R_{44'}$ are the contact resistances at electrodes 1−4, respectively. In the four-probe method, a known voltage, V_b, is applied between electrode 1 and 4, and both the current, I, flowing through the sample and the voltage between electrodes 2 and 3, V_{23}, are measured. Ideally, the voltage measurement draws no current. Therefore, the currents between points 2,2′ and 3,3′ are zero, and the voltages at points 2 and 3 are equal to

Table 1. Electrical Properties of 2D NP Assemblies[a]

NP (2*R*, nm)	molecule[b]	*s*, nm	σ, Ω^{-1} cm^{-1}	*T*-dependence[c] (E_a, meV)	prep. method[d]	ref
Au (3.7)	**1**	1.9		A (97)	SC	Andres et al.[116]
Au (2.9 ± 0.8)	$C_{12}S$		5×10^{-6}	A (70)	LB	Bourgoin et al.[136]
"	**2**		5×10^{-3}	A (55)	"	"
Ag (2.6)	C_5S	0.5 ± 0.2		M	LS	Medeiros-Ribeiro et al.[138]
"	C_6S	0.5 ± 0.2		M	"	"
"	$C_{10}S$	1.1 ± 0.2		nM	"	"
Ag (2.7)	C_5S	>1.1		nM	LS	Kim et al.[139]
"	C_6S	1.1		nM	"	"
Ag (4.8)	C_8S	1.2		M	"	"
Ag (6.6)	$C_{12}S$	2.0		nA	"	"
Ag (7.8)	C_8S	variable		A (15−35)	LS	Sampaio et al.[140]
"	$C_{10}S$	"		"	"	"
Au (2.2−2.9)	$C_{12}S$	1.2 ± 0.1		nA	DC	Parthasarathy et al.[271]
Ag (4.0 ± 0.2)	C_6S	variable		MIT	Langmuir	Quinn et al.[221]
Ag (7 ± 0.56)	$C_{12}S$	0.8	3×10^{-2}	nA	LS	Beverly et al.[141]
Ag (7 ± 0.56)	"	"	6×10^{-2}	"	"	"
Ag (7 ± 0.63)	"	"	1.5×10^{-2}	"	"	"
Ag (7 ± 0.64)	"	"	2.4×10^{-3}	"	"	"
Ag (7 ± 0.70)	"	"	1.2×10^{-3}	"	"	"
Ag (7 ± 0.96)	"	"	1.2×10^{-4}	"	"	"
Au (2 ± 0.2)	C_4S	1.01	1.6×10^{-3}		Langmuir	Chen[135]
"	"	0.90	2.7×10^{-3}		"	"
"	"	0.87	3.3×10^{-3}		"	"
"	"	0.84	3.7×10^{-3}		"	"
"	"	0.82	4.1×10^{-3}		"	"
"	"	0.80	5.0×10^{-3}		"	"
"	C_5S	1.23	8.2×10^{-4}		"	"
"	"	1.14	8.2×10^{-4}		"	"
"	"	1.06	8.2×10^{-4}		"	"
"	"	1.02	1.1×10^{-3}		"	"
"	"	0.98	1.3×10^{-3}		"	"
"	"	0.95	3.5×10^{-3}		"	"
"	"	0.92	6.8×10^{-3}		"	"
Au (4.6−6.5)	$C_{12}S$	1.5−2.6		A (38)	DC	Parthasarathy et al.[272]
Au (1.6 ± 0.16)	C_6S	0.9	1×10^{-5}		LS	Liljeroth et al.[142]
"	$C_{12}S$	1.4	6×10^{-6}		"	"
Au (6.6 ± 0.8)	$C_{12}S$	2.5	2×10^{-3}		"	"
"	"	1.8	5×10^{-3}		"	"
"	"	1.5	8×10^{-3}		"	"
"	"	1.3	1×10^{-2}		"	"

[a] *R* = NP radius, *s* = inter-NP separation, σ = conductivity, and E_a = activation energy. [b] $C_nS = CH_3(CH_2)_{n-1}SH$; $C_nS_2 = HS(CH_2)_nSH$; **1** = 1,4-di-(4-isocyanophenylethynyl)-2-ethylbenzene; and **2** = 2,5″-bis(acetylthio)-5,2′,5′,2″-terthienyl. [c] A = Arrhenius; nA = non-Arrhenius; M = metallic; nM = nonmetallic; and MIT = metal−insulator transition. [d] DC = drop-casting; LB = Langmuir−Blodgett; LS = Langmuir−Schaefer; and SC = spin-casting.

those at points 2′ and 3′, respectively. Given V_{23} ($=V_{2'3'}$) and *I*, the resistance of the sample between points 2′ and 3′ is determined by $R_{2'3'} = V_{2'3'}/I = V_{23}/I$. Thus, contributions from the contact resistances are eliminated.

4. Electronic Properties

NP assemblies represent a new class of granular materials. Granular materials consist of grains embedded in insulating matrices and exhibit electronic properties that depend on architecture and composition of the materials.[6,223,224] Conventional granular films are usually prepared by deposition, e.g., thermal evaporation, sputtering, chemical vapor deposition, electroless deposition, etc., and are typically disordered.[223] Electronic properties of granular films have been extensively studied, and three distinct regimes have been typically observed:[223] (i) an *insulating regime*, where the volume fraction of grains is small and the grains form isolated islands; (ii) a *bulk regime*, where the concentration of grains is large enough that the isolated islands merge and form continuous pathways through the film; and (iii) a *transition regime*, where a transition from insulating to bulk regimes occurs at a critical concentration of grains (percolation threshold). Above the threshold, at least one sample spanning pathway is established throughout the film. Charge transport mechanisms in these regimes, however, have not yet been fully understood, and efforts in this area are ongoing.

NP assemblies provide a controlled platform to systematically explore charge transport in granular materials by permitting studies of structure−property relationships. NP properties (e.g., size, shape, and composition), inter-NP separation, and material structure are independently controllable, since steps for synthesizing building blocks (i.e., NPs and molecular spacers) and steps for assembling materials are decoupled. Because of a broad range of choices for the building blocks and the manner in which they can be arranged into materials, a wide range of material properties has been realized. Examples are summarized in Tables 1 and 2 for 2D and 3D assemblies, respectively. A majority of these assemblies consist of metal NPs, in particular Au or Ag NPs, the focus of this review. For a review on electron transport in assemblies of semiconducting NPs, see ref 225.

Although our understanding of charge transport through NP assemblies is still evolving, several phenomena are known to be particularly important given the structure of the assemblies. These include tunneling, single-electron

Table 2. Electrical Properties of 3D NP Assemblies[a]

NP ($2R$, nm)	molecule[b]	s, nm	σ, Ω^{-1} cm^{-1}	T-dependence[c] (E_a, meV)	prep. method[d]	ref
Au (2.4 ± 0.2)	C_8S	1.31	1.8×10^{-5}	A (100)	DC	Terrill et al.[122]
"	$C_{12}S$	1.48	2.3×10^{-7}	A (166)	"	"
"	$C_{16}S$	1.83	2.8×10^{-9}	A (197)	"	"
Au (2.2)	C_5S_2	1.11[e]	6.7×10^{-6}	A (140)	CL	Bethell et al.[155]
"	C_6S_2	1.30[e]	3.6×10^{-7}	A (120)	"	"
"	BDMT	1.08[e]	6.7×10^{-6}	A (100)	"	"
Au (8 ± 2)	BDMT	1.08[e]	7.7×10^{-2}	A (20)	"	"
"	$C_{12}S_2$	1.89[e]	1.3×10^{-3}	A (30)	"	"
"	C_6S_2	1.30[e]	1.5×10^{-1}	A	SSA	"
"	C_9S_2	1.50[e]	1.2×10^{-2}	"	"	"
"	$C_{12}S_2$	1.89[e]	6.6×10^{-4}	"	"	"
Au (11)	$HS(CH_2)_2OH$		2×10^{3}		SSA	Musick et al.[158,206]
Au (4.8 ± 1.6)	PDDA/Poly S-119		2×10^{5}		ionic SSA	Liu et al.[90]
Au (1.7)	$C_{12}S$	1.52[e]	2×10^{-9}	nA	DC	Snow et al.[176]
Au (2.3)	"	"	1×10^{-8}	"	"	"
Au (3.1)	"	"	5×10^{-8}	"	"	"
Au (4.6)	"	"	2×10^{-7}	"	"	"
Au (6.0)	"	"	1×10^{-6}	"	"	"
Au (7.2)	"	"	3×10^{-6}	"	"	"
Pd (2.4)	phenanthroline			A (20)	DC	Simon et al.[486]
"	**3**			A (50)	CL	
Au (6)	C_9S_2	1.5[e]		A (20)	SSA	Brust et al.[156]
Au (2)	C_9S_2	1.5[e]	10^{-3}	A (140)	CL IDA	Leibowitz et al.[152]
Au (5)	"	"	10^{-1}	A (30)	"	"
Co (10 ± 0.5)	oleic acid	2		A (10)	DC/TA	Black et al.[129]
Au (13)	24-mer DNA	11.5	$10^{-3}-10^{-5}$	A (7.4)	CL	Park et al.[88]
"	48-mer DNA	11.5	"	A (7.5)	"	"
"	72-mer DNA	11.5	"	A (7.6)	"	"
Au (2.2 ± 0.7)	C_4S	0.52[e]	8.0×10^{-2}	A (96)	DC	Wuelfing et al.[123]
"	C_5S	0.65[e]	5.0×10^{-2}	A (78)	"	"
"	C_6S	0.77[e]	8.0×10^{-3}	A (68)	"	"
"	C_7S	0.90[e]	5.0×10^{-3}	A (69)	"	"
"	C_8S	1.02[e]	1.6×10^{-3}	A (95)	"	"
"	$C_{10}S$	1.27[e]	1.3×10^{-4}	A (91)	"	"
"	$C_{12}S$	1.52[e]	8.0×10^{-5}	A (166)	"	"
"	$C_{16}S$	2.02[e]	1.3×10^{-6}	A (197)	"	"
Pb (20 ± 4)	C_5COOH	1.1		S	DC	Weitz et al.[11]
"	C_7COOH	1.5		S	"	"
"	$C_{11}COOH$	2.2		I	"	"
"	$C_{17}COOH$	2.8		I	"	"
Au (2.9)	p-HSC_6H_4COOH		2.5×10^{-6}	A (63)	DC	Evans et al.[399]
Au (3.2)	p-HSC_6H_4OH		7.8×10^{-7}	A (52)	"	"
Au (3.6)	p-$HSC_6H_4CH_3$		6.1×10^{-4}	A (78)	"	"
Au (6.0)	p-$HSC_6H_4NH_2$		7.8×10^{-2}	A (22)	"	"
Ag (3.5)	$C_{12}S$	1.6	6×10^{-7}	nA	DC	Doty et al.[175]
Ag (4.5)	"	"	4×10^{-7}	nA	"	"
Ag (4.8)	"	"	6×10^{-7}	nA	"	"
Ag (5.5)	"	"	8×10^{-7}	nA	"	"
Ag (7.7)	"	"	5×10^{-7}	nA	"	"
Au (7 ± 1)	C_2S_2	0.81[e]		M	SSA	Fishelson et al.[159]
"	C_5S_2	1.1[e]		A (5)	"	"
"	C_8S_2	1.46[e]		A (15)	"	"
Au (15)	C_4S_2	1.02[e]		MIT	SSA	Trudeau et al.[161]
Au (2.2)	PhC_4S	1.42 ± 0.18	1.5×10^{-4}	A (42)	DC	Wuelfing et al.[240]
"	PhC_2S	1.02 ± 0.19	2.6×10^{-3}	A (91)	"	"
Au (3.0)	PhC_2S	1.06 ± 0.09	7.2×10^{-3}	A (64)	"	"
"	$CH_3C_6H_4SH$	0.66 ± 0.08	1.3×10^{-2}	A (59)	"	"
Au (8)	C_2S_2	0.81[e]	9×10^{-1}	nA	CL	Müller et al.[151]
"	C_4S_2	1.02[e]	3×10^{-1}	"	"	"
"	C_8S_2	1.46[e]	4×10^{-2}	"	"	"
"	$C_{12}S_2$	1.89[e]	1×10^{-2}	"	"	"
"	$C_{15}S_2$	2.23[e]	5×10^{-4}	"	"	"
Au (22 ± 3)	C_4S_2	1.02[e]		M	SSA	Trudeau et al.[162]
Au (1.4)	**4**	1.1[e]		nA (95)[f]	CL	Torma et al.[207]
"	**5**	1.6[e]		nA (110)[f]	"	"
"	**6**	2.3[e]		nA (120)[f]	"	"
"	**7**	1.5[e]		nA (140)[f]	"	"
"	**8**	0.7[e]		nA (160)[f]	"	"
"	**9**	1.9[e]		nA (200)[f]	"	"
"	**10**	2.8[e]		nA (230)[f]	"	"
"	**11**	3.1[e]		nA (260)[f]	"	"
Au (1.6 ± 0.8)	$C_4S/MUA/Cu^{2+}$	1.52 ± 0.22	2×10^{-4}		SSA	Zamborini et al.[172,173]
"	$C_8S/MUA/Cu^{2+}$	1.80 ± 0.33	9×10^{-6}		"	"
"	$C_{12}S/MUA/Cu^{2+}$	2.02 ± 0.39	5×10^{-7}		"	"
Au (4.0 ± 0.8)	C_6S_2	1.30[e]	3.7×10^{-2}	A (47.7)	SSA	Joseph et al.[404]
"	C_9S_2	1.5[e]	2.1×10^{-3}	A (54.2)	"	"
"	$C_{12}S_2$	1.89[e]	2.3×10^{-4}	A (56.6)	"	"
"	$C_{16}S_2$		4.8×10^{-5}	A (58.9)	"	"
Au (4.0 ± 0.8)	PPI-G1		6.8×10^{-2}	A (40.2)	SSA	Joseph et al.[111]
"	PPI-G2		1.7×10^{-2}	A (44.8)	"	"
"	PPI-G3		9.7×10^{-3}	A (50.5)	"	"

Table 2. Continued

NP ($2R$, nm)	molecule[b]	s, nm	σ, Ω^{-1} cm^{-1}	T-dependence[c] (E_a, meV)	prep. method[d]	ref
"	PPI-G4		3.9×10^{-3}	A (54.6)	"	"
"	PPI-G5		1.0×10^{-3}	A (61.1)	"	"
"	$C_{16}S_2$		4.8×10^{-5}	A (58.9)	"	"
Au (1.6 ± 0.7)	C_7S/MUA/Ag+	3.2	7.8×10^{-5}		SSA	Leopold et al.[410]
"	C_7S/MUA/Cu^{2+}	3.6	1.1×10^{-5}		"	"
"	C_7S/MUA/Zn^{2+}	3.8	3.0×10^{-6}		"	"
"	C_7S/MUA/La^{3+}		1.2×10^{-5}		"	"
Au (4.0 ± 0.8)	BDMT	0.77[e]	1.1×10^{-1}	A (59.7)	SSA	Wessels et al.[163]
"	cHDMT	0.82[e]	1.2×10^{-2}	A (58.8)	"	"
"	DMAAB	1.48[e]	2.4×10^{-3}	A (65)	"	"
"	DMAAcH	1.49[e]	1.1×10^{-4}	A (71)	"	"
"	PBDT	1.07[e]	1.2×10^{1}	M	"	"
"	cHBDT	0.96[e]	2.4×10 °	A (13.8)	"	"
CdSe (5.4 ± 0.27)	1,4-$NH_2C_6H_4NH_2$	0.7		nA (30)[f]	DC/CL/TA	Yu et al.[131]
$CoPt_3$ (10.2 ± 0.9)	ACA/$C_{16}N$	2.1	2.5×10^{-3}	A (7)	DC/TA	Beecher et al.[124]
$CoPt_3$ (3.8 ± 0.34)	ACA/$C_{16}N$	2.2	10^{-4}	A (3)1	DC/TA	Beecher et al.[125]
"	"		10^{-1}	nA	"	"
"	"		10^{1}	M	"	"
$CoPt_3$ (10.2 ± 1.0)	ACA/$C_{16}N$	2.8		A (7)	DC/TA	Quinn et al.[126]
$CoPt_3$ (6.8 ± 0.68)		2.9		A (12)	"	"
$CoPt_3$ (3.8 ± 0.38)		2.7		A (32)	"	"
PbSe (6.3)	C_7N_2			nA	DC/CL/TA	Wehrenberg et al.[132]
Au (6.5 ± 1.5)	C_4S_2	1.02[e]		A (6)	SSA	Suganuma et al.[12]
Au (4.8 ± 1.2)	C_4S_2	1.02[e]		nA	SSA	Dunford et al.[164]
Au (5.3 ± 0.9)	BDMT	0.77[e]		nA	SSA	Xu et al.[185]
Au (5.5 ± 0.28)	$C_{12}S$	2.5		nA (27.6)[f]	LB/SSA	Tran et al.[296]
PbSe (5.5 ± 0.28)	oleic acid	0.7		nA (38)[f]	DC/TA	Romero et al.[133]
Au (2.0 ± 0.7)	C_3S_2	0.844	2.89×10^{-2}	A (6.18)	CL IDA	Wang et al.[263]
"	C_5S_2	1.101	6.84×10^{-3}	A (6.79)	"	"
"	C_8S_2	1.488	7.93×10^{-4}	A (8.14)	"	"
"	C_9S_2	1.616	3.32×10^{-4}	A (8.83)	"	"
"	$C_{10}S_2$	1.745	3.12×10^{-4}	A (8.81)	"	"
Au (4.0 ± 0.5)	C_3S_2	0.844	1.03×10^{-1}	A (2.19)	"	"
"	C_5S_2	1.101	2.26×10^{-2}	A (2.51)	"	"
"	C_8S_2	1.488	6.38×10^{-4}	A (3.15)	"	"
"	C_9S_2	1.616	3.38×10^{-4}	A (3.29)	"	"
"	$C_{10}S_2$	1.745	2.10×10^{-4}	A (3.30)	"	"
Au (5.0 ± 0.8)	C_2S_2	0.81[e]		M	SSA	Zabet-Khosousi et al.[166]
"	C_3S_2	0.9[e]		M	"	"
"	C_4S_2	1.02[e]		M	"	"
"	C_5S_2	1.11[e]		M or nA (9.2)[f]	"	"
"	C_6S_2	1.30[e]		nA (13.6)[f]	"	"
"	C_8S_2	1.46[e]		nA (16.7)[f]	"	"
"	C_9S_2	1.5[e]		nA (18.1)[f]	"	"
"	$C_{10}S_2$	1.6[e]		nA (18.8)[f]	"	"
Au (1.1)	PhC_2S	0.60	6.1×10^{-9}	A (485)	DC	Choi et al.[360]
Au (1.6)	C_6S	0.46	2.9×10^{-5}	A (80)	"	"
Au (4.1 ± 0.5)	oligothiopene 3mer	1.6	3.0×10 °	nA (21)[f]	CL	Taniguchi et al.[86]
"	oligothiopene 9mer	3.3	1.2×10^{-2}	nA (45)[f]	"	"

[a] R = NP radius, s = inter-NP separation, σ = conductivity, and E_a = activation energy. [b] $C_nS = CH_3(CH_2)_{n-1}SH$; $C_nS_2 = HS(CH_2)_nSH$; ACA = 1-adamantanecarboxylic acid; BDMT = 1,4-$C_6H_4(CH_2SH)_2$; cHDMT = 1,4-$C_6H_{10}(CH_2SH)_2$; cHBDT = Na_2[1,4-$C_6H_{10}(NHCS_2)_2$]; DMAAB = 1,4-$C_6H_4(NHCOCH_2SH)_2$; DMAAcH = 1,4-$C_6H_{10}(NHCOCH_2SH)_2$; MUA = $HS(CH_2)_{10}COOH$; PBDT = Na_2[1,4-$C_6H_4(NHCS_2)_2$]; PDDA = poly(diallyldimethylammonium chloride); PPI-G1 = poly(propyleneimine) dendrimer-generation one; **3** = 4,4′-diamino-1,2- diphenylethane; **4** = 4,4′-thiobis(benzenethiol); **5** = dimer(2,8-dithio-6-hydroxypurine); **6** = dimer(4,4′-thiobis(benzenethiol)); **7** = dimer(1,5-dithionaphthaline); **8** =$(C_6H_5)_3P$;**9**=$(C_6H_5)_2PC_6H_4SO_3H$/4,4′-$H_2NC_6H_4CH_2CH_2C_6H_4NH_2$;**10**=$(C_6H_5)_2PC_6H_4SO_3H$/4,4′-$H_2NC_6H_4-C\equiv C-C_5H_4-C\equiv C-C_5H_4-C\equiv C-C_6H_4-NH_2$; **11** = thiolate-functionalized heptacyclopentylsilsesquioxane. [c] A = Arrhenius; nA = non-Arrhenius; M = metallic; S = superconducting; I = insulating; and MIT = metal−insulator transition. [d] DC = drop-casting; CL = cross-linking; SSA = stepwise self-assembly; LB = Langmuir−Blodgett; and TA = thermal-annealing. [e] Theoretical values. [f] Activation energies obtained from Arrhenius plots.

charging, hopping, varying wave function overlap, spatial and charge disorder, percolation effects, scattering, etc. These processes and their roles in influencing assembly electronic behavior are reviewed in this section.

4.1. Tunneling

Tunneling enables charge to flow between weakly coupled sites, that is, where wave functions are mainly localized on each site. It can be an important charge transport mechanism in NP assemblies. A treatment of this process starting from Schroedinger's equation is provided in Appendix A. Here, we consider in detail a system consisting of two closely spaced 1D metal electrodes separated by an insulator with dielectric constant ε_r and subjected to a potential energy difference. This simple model system yields valuable physical insight into tunneling.[226−228]

4.1.1. Metal−Insulator−Metal Junctions

Tunneling is an elastic process; that is, the electron's initial and final energies are equal. Also, electrons must leave from a filled state of one electrode and enter an empty state of the other electrode to satisfy Pauli's exclusion principle. The probability of finding a filled energy state in a metal electrode is given by the Fermi−Dirac distribution,

$$f(E) = \frac{1}{1 + e^{(E-\mu)/k_B T}} \quad (9)$$

where μ is the chemical potential. At $T = 0$ K, the Fermi−Dirac distribution becomes a step function and μ represents the highest occupied energy (or the Fermi energy, E_F) of the electrode. Figure 13 shows the Fermi−Dirac distributions for gold (E_F = 5.5 eV) at 0 and 298 K. The combined probability of finding a filled state in one electrode and an empty state in the other electrode, both with energy E, is then $f(E) \times [1 - f(E)]$, assuming that the electrodes are identical.

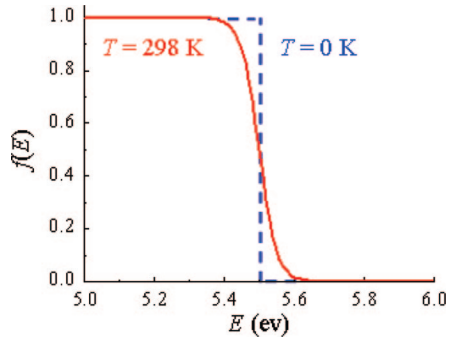

Figure 13. Fermi−Dirac distribution for Au at $T = 0$ K (dashed blue line) and $T = 298$ K (solid red line).

When a positive bias voltage ($V_b > 0$) is applied to an electrode, its chemical potential is shifted to $\mu - eV_b$. The Fermi−Dirac distribution for the electrode is then expressed by

$$\frac{1}{1+e^{[E-(\mu-eV_b)]/k_BT}} = \frac{1}{1+e^{[(E+eV_b)-\mu]/k_BT}} = f(E+eV_b) \tag{10}$$

The probability of finding filled and empty states in the electrodes thus changes to $f(E) \times [1 - f(E + eV_b)]$.

Figure 14 shows an energy diagram of a junction composed of two identical metal electrodes. Electrons tunneling between the electrodes encounter a potential energy barrier whose height, when $V_b = 0$, is given by

$$U = \phi + E_F - E \tag{11}$$

where work function, ϕ, is defined as the difference between the Fermi and vacuum energy levels (Figure 14a). Work functions for metals are typically in the order of a few eV. For $V_b > 0$ (Figure 14b), the barrier height at a distance x within the barrier varies linearly with x:

$$U(x) = \phi + E_F - E - eV_b x/L \tag{12}$$

Note that U adopts appropriate values at $x = 0$ and L.

In a proximity of a metal electrode, an electron polarizes the electrode's surface and creates an image with an opposite charge that in turn exerts an attractive force on the electron. In a tunnel-junction geometry, image charges themselves generate image charges in the other electrode, and an electron is affected by all of the resulting forces. Simmons[229] has discussed in detail the influence of image forces on the shape of a potential barrier between planar electrodes. He showed that the image force reduces the height and the width of the barrier, and the image potential can be approximated by

$$U_{image} = -1.15\frac{e^2 \ln 2}{16\pi\varepsilon_r\varepsilon_0}\frac{L}{x(L-x)} \tag{13}$$

where ε_0 is the permittivity of vacuum and ε_r is the dielectric constant of the insulating material between electrodes. The modified barrier height is then expressed as

$$U(x) = \phi + E_F - E - \frac{eV_b x}{L} - 1.15\frac{e^2 \ln 2}{16\pi\varepsilon_r\varepsilon_0}\frac{L}{x(L-x)} \tag{14}$$

As a first approximation, one can replace the barrier height by an average value given by[226]

$$\overline{U} = \frac{1}{L}\int_0^L U(x)\,dx \tag{15}$$

At room temperature, thermal fluctuations in electron energy are on the order of $k_BT \approx 25$ meV, much smaller than typical barrier heights. Therefore, except at high temperatures or voltages, charge transport between electrodes is forbidden classically. Electrons can, however, tunnel through the potential barrier (see Appendix A). The tunneling transmission probability, $|T|^2$, in the limit of a thick barrier, decays exponentially with the barrier width (L),

$$|T|^2 \approx e^{-2\kappa L} \tag{16}$$

where κ is the decay constant. κ depends on the barrier height as follows,

$$\kappa = \frac{\sqrt{2m\overline{U}}}{\hbar} \tag{17}$$

where m is the mass of electron and $\hbar$ is Planck's constant. Assuming that the electrodes are clean and made of gold and approximating the barrier height with the work function ($\phi \approx 5.1$ eV), we find $\kappa \approx 1.1$ Å^{-1} and $|T|^2 \approx e^{-2.2\ L/Å} \approx 10^{-L/Å}$. Therefore, the tunneling transmission probability drops by ~1 order for every 1 Å increase in the barrier width.

The rate of electron tunneling from electrode 1 to 2 at energy E, $\Gamma_{1\to2}(E)$, can be obtained using Fermi's golden rule,

$$\Gamma_{1\to2}(E) = 2\frac{2\pi}{\hbar}\rho(E)\rho(E+eV_b)|T(E)|^2 f(E)[1-f(E+eV_b)] \tag{18}$$

where ρ represents the density of states of the electrodes and the factor of 2 arises from the spin degeneracy of electrons. Integrating the contributions from all energies, we

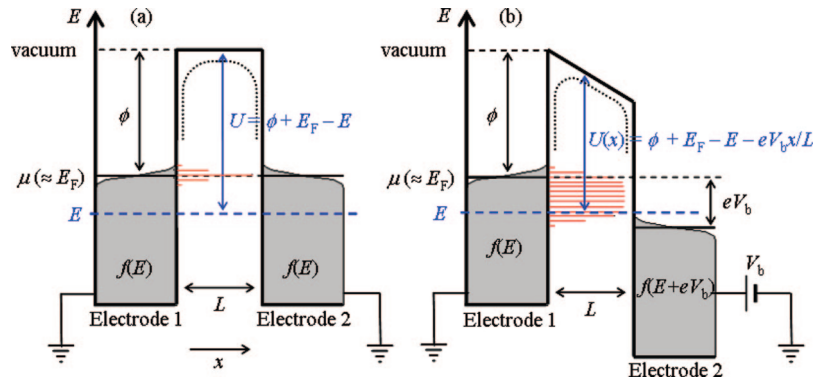

Figure 14. Energy diagrams for a tunnel junction composed of two electrodes at (a) $V_b = 0$ and (b) $V_b > 0$. Red lines represent energy states available for electron tunneling from electrode 1 to 2. Dotted lines show effects of image forces on the potential barriers.

get an expression for the total tunneling rate from electrode 1 to 2:

$$\Gamma_{1\to2} = 2\frac{2\pi}{\hbar}\int_0^{+\infty} \rho(E)\rho(E+eV_b)|T(E)|^2 f(E)[1-f(E+eV_b)]\,dE \quad (19)$$

Similarly, the rate of electron tunneling from electrode 2 to 1 is given by

$$\Gamma_{2\to1} = 2\frac{2\pi}{\hbar}\int_0^{+\infty} \rho(E)\rho(E+eV_b)|T(E)|^2 [1-f(E)]f(E+eV_b)\,dE \quad (20)$$

The net rate of electron tunneling between the two electrodes, Γ, can be obtained by subtracting eq 20 from eq 19: $\Gamma = \Gamma_{1\to2} - \Gamma_{2\to1}$. The tunneling current (i.e., the rate of charge flow) between the electrodes is then given by $I = e\Gamma$:

$$I = \frac{4\pi e}{\hbar}\int_0^{+\infty} \rho(E)\rho(E+eV_b)|T(E)|^2[f(E)-f(E+eV_b)]\,dE \quad (21)$$

At low bias voltages ($eV_b \ll E_F$) and at room temperature, energy levels close to the Fermi level dominate in tunneling. Therefore, we can simplify the expression for current (eq 21) by approximating the density of states and the tunneling transmission with their respective values at E_F:

$$I \approx \frac{g_0}{e}\int_0^{+\infty}[f(E)-f(E+eV_b)]\,dE \quad (22)$$

where

$$g_0 = \frac{4\pi e^2}{\hbar}\rho(E_F)^2|T(E_F)|^2 \quad (23)$$

The integral in eq 22 can be solved analytically (see Appendix C) and is equal to eV_b. The tunneling current at low bias then becomes

$$I = g_0 V_b \quad (24)$$

Equation 24 indicates that g_0 is the tunneling conductance at low bias:

$$dI/dV_b = g_0 \quad (25)$$

Since g_0 depends on $|T(E_F)|^2 \approx \exp(-2\kappa L)$, the tunneling conductance drops exponentially with electrode separation,

$$g_0 \propto \exp(-\beta L) \quad (26)$$

where $\beta = 2\kappa \approx 2.2$ Å^{-1} for clean Au electrodes. Note that g_0 does not exhibit explicit temperature dependence, and therefore, tunneling conduction is often characterized by its temperature independence.

At large biases, higher order voltage terms in the current expression become significant. For example, bias reduces the barrier height according to eq 12 and modifies $|T(E_F)|^2$. By taking this into account, one obtains an exponential dependence of tunneling current on bias (see Appendix B for derivation),

$$I(V_b) \propto e^{-2\kappa_0 L}\sinh\left(\frac{eV_b}{2\xi}\right) \quad (27)$$

where $\kappa_0 \equiv (2m\phi)^{1/2}/\hbar$ is the decay constant at zero bias and $\xi \equiv \phi/\kappa_0 L$.

4.1.2. Metal−Molecule−Metal Junctions

The discussion in section 4.1.1 can also be applied in a junction in which a molecule is placed between the electrodes. In this case, the effective barrier height for tunneling depends on the alignment of the Fermi level of the electrodes with respect to the highest occupied and lowest unoccupied orbitals of the molecule (HOMO and LUMO). If conduction is dominated by electron (or hole) transport, then the effective height, ϕ_{eff}, can be approximated by $E_{LUMO} - E_F$ (or $E_F - E_{HOMO}$).[230] Barrier heights for metals with molecules are usually smaller than those for clean metal electrodes, and this leads to smaller values of β. For example, Frisbie and co-workers[217−219] have studied $I-V$ characteristics of self-assembled monolayers of alkanethiols with various chain lengths on Au substrates using CP-AFM and observed $\beta \approx 0.9$ Å^{-1}. They have also found that monolayers of oligophenylene thiols exhibit higher conductances with a smaller value of $\beta \approx 0.4$ Å^{-1}, likely due to smaller HOMO−LUMO energy gaps and closer positioning of the Fermi level to frontier orbitals in conjugated oligophenylene thiols than in saturated alkanethiols.[231]

Treatments of charge transport through molecular junctions taking into account molecular orbitals have been reviewed in a number of articles.[57,232−235] One treatment that has been extensively studied is based on a traditional molecular model of charge transfer in donor−bridge−acceptor (D−B−A) systems.[236] This "superexchange" model was originally proposed by McConnell[237] to describe the rate of charge-transfer reactions in solution. In the superexchange model, charge transfer is mediated by virtual states, namely, D^+-B^--A or $D-B^+-A^-$ for electrons or holes, respectively. The rate of charge transfer, k_{CT}, is given by

$$k_{CT} \approx \exp(-\beta' r_{DA}) \quad (28)$$

where r_{DA} is the distance between the donor and the acceptor,

$$\beta' = \frac{2}{a}\ln\left(\frac{\Delta E_B}{V_B}\right) \quad (29)$$

a is the length of the bridge unit, ΔE_B is the energy of the mediating states (D^+-B^--A or $D-B^+-A^-$) relative to the ground state (D−B−A), and V_B is the coupling energy between two adjacent units. Using typical values of $\Delta E_B/V_B = 10$ and $a = 5$ Å, eq 29 gives $\beta' = 0.92$ Å^{-1}.[232]

Nitzan[238] has derived an approximate relationship between k_{CT} and molecular conductance under a number of assumptions (e.g., that the electronic structure of the molecule does not considerably change upon attaching to the electrodes):

$$g \approx \frac{8e^2}{\pi^2\Gamma_D\Gamma_A}\left(\frac{k_{CT}}{DOS}\right) \quad (30)$$

where DOS represents a Franck−Condon weighted density of vibronic states and Γ_D and Γ_A are, respectively, widths of the donor and the acceptor levels due to their couplings to the electrodes. The latter depend on the finite lifetime of an electron on the molecule adsorbed on the metal surface. Using typical values of $\Gamma_D = \Gamma_A \approx 0.5$ eV, eq 30 yields

$$g \approx 5\times10^{-19}\frac{k_{CT}}{DOS} \quad (31)$$

The agreement between eq 31 and experimental values is quite remarkable.[57] Smalley et al.[239] have measured the rate of charge transfer through ferrocene-terminated alkanethiolate

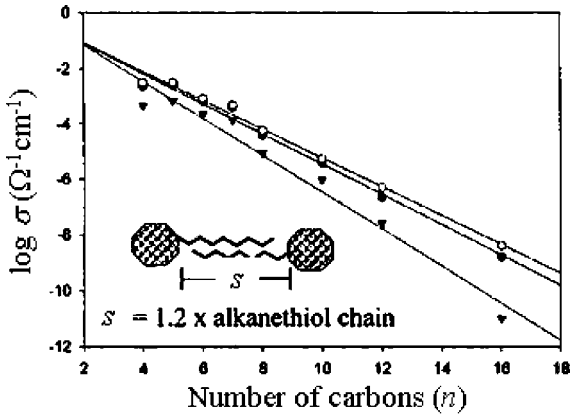

Figure 15. Conductivities of films of $CH_3(CH_2)_{n-1}S$-capped 2.2 nm Au NPs at 70 (○), 30 (●), and −60 °C (▼) vs n. The inset is a schematic illustrating interdigitation of capping ligand chains in the NP films. Reprinted with permission from ref 123 (Murray's group). Copyright 2000 American Chemical Society (http://dx.doi.org/10.1021/ja002367+).

monolayers on gold electrodes using an electrochemical approach. For $n = 9$, they measured $k_{CT} \approx 10^4$ s^{-1}. Using DOS $\approx 7 \times 10^{-6}$ $(eV)^{-1}$,[57] one obtains $g \approx 7 \times 10^{-10}$ $\Omega^{-1} = (1.4\ G\Omega)^{-1}$, which is consistent with the value reported by Frisbie and co-workers using CP-AFM.[217]

4.1.3. Tunneling in NP Assemblies

A number of studies have demonstrated the importance of tunneling in films of weakly coupled NPs. Murray and co-workers[122,123] have studied electronic conductivities of 3D films of 2.2 nm Au NPs capped with a variety of alkanethiolates. They prepared NP films by drop-casting solutions of $CH_3(CH_2)_{n-1}S$-capped NPs onto IDA electrodes. Figure 15 shows that film conductivities, σ, at various temperatures exhibited an exponential dependence on n,

$$\sigma \approx \exp(-\beta_n n) \tag{32}$$

where β_n is the decay constant per n. This observation suggests that film conductivity is dominated by electron tunneling between NPs, and the length of the capping molecules determines the inter-NP surface-to-surface separation, s. Since s is proportional to n, σ can also be written as

$$\sigma \approx \exp(-\beta s) \tag{33}$$

where β is the decay constant per unit length. Typical observed values of β and β_n were ~1.0 $Å^{-1}$ and ~1.2, respectively. These values are consistent with those reported in single-molecule tunneling studies (section 4.1.2).

A number of groups have also explored NP assemblies incorporating conjugated molecules. Wuelfing et al.[240] have studied conductivities of films of Au NPs capped with arenethiolates. Films were prepared by drop-casting NP solutions on IDA electrodes. Wessels et al.[163] have studied conductivities of films of Au NPs cross-linked with a variety of saturated and conjugated molecules. Films were constructed using a stepwise self-assembly method. In both studies, film conductivities did not exhibit a clear exponential dependence on inter-NP separations (Figure 16a). However, an exponential relationship was observed when conductivities were plotted as a function of the number of saturated carbon−carbon bonds (n_{sat}),

$$\sigma \approx \exp(-\beta_n n_{sat}) \tag{34}$$

with $\beta_n \approx 1$ (Figure 16b). When saturated molecules were replaced by conjugated molecules with the same skeleton, e.g., 1,4-cyclohexanedimethylthiol (cHDMT) by 1,4-benzenedimethylthiol (BDMT), film conductivities increased by ~1 order of magnitude. Similar differences between conductivities of conjugated versus saturated molecules have been reported in studies involving metal−molecule−metal junctions (see section 4.1.2). Studies on this subject are ongoing in the rapidly growing field of molecular electronics.[205,231,241−243]

4.2. Single-Electron Charging

Given potentially small sizes of NPs, single-electron charging can strongly influence electronic properties of NP assemblies. When an electron tunnels to (from) an NP, it charges (discharges) the NP. At absolute zero, the energy required to do so must be provided by a sufficiently large external bias, otherwise current cannot flow. That is, below a voltage threshold, current and conductance are zero. This is known as "Coulomb blockade" (CB). As the temperature increases, electrons are able to overcome the Coulomb blockade thermally, and current and conductance increase.

We can gain insight into the role of single-electron charging by considering a simple system where a single metallic NP is attached to two metal electrodes via tunnel junctions (Figure 17). Current−voltage characteristics of this system can be described by a semiclassical, so-called "orthodox" theory.[228,244−246] In the orthodox theory, each junction j ($j = 1, 2$) is modeled as a parallel combination of

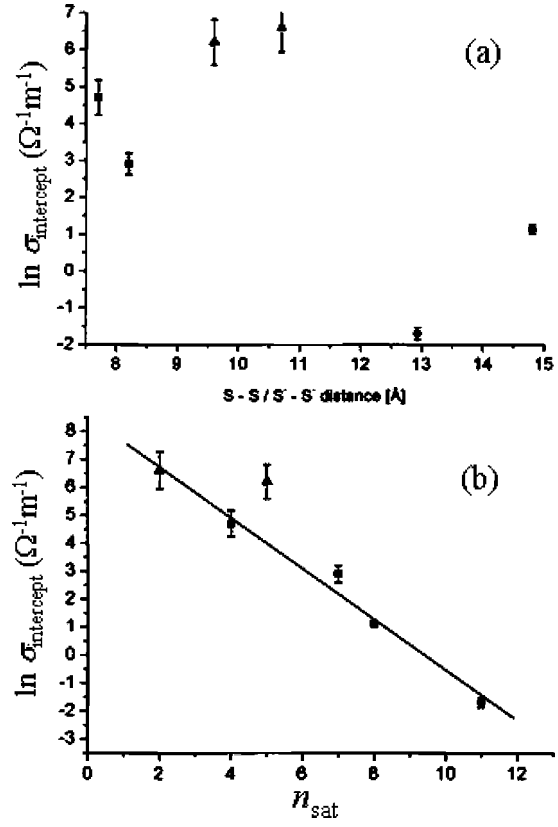

Figure 16. (a) Plot of $\ln(\sigma_{intercept})$ for multilayer films of cross-linked NPs as a function of the length of the linker molecules. (b) Plot of $\ln(\sigma_{intercept})$ as a function of the number of saturated bonds in the linker molecules. $\sigma_{intercept}$ was calculated from extrapolating plots of σ vs $1/T$ to very high temperatures. Reprinted with permission from ref 163 (Wessels' group). Copyright 2004 American Chemical Society (http://dx.doi.org/10.1021/ja0377605).

a capacitance, C_j, and a resistance, R_j. The junction capacitances determine the voltage, V_j, dropped across each junction,

$$V_j = \frac{C_1 C_2}{C_j C_\Sigma} V_b \tag{35}$$

where $C_\Sigma = C_1 + C_2$. According to eq 22, R_j controls the electron tunneling rate ($\Gamma_j^\pm$, where $\pm$ refers to electrons tunneling on/off the NP) for the corresponding junction:

$$\Gamma_j^\pm = \frac{1}{e^2 R_j} \int_0^{+\infty} f(E)[1 - f(E - \Delta E_j^\pm)]\, dE \tag{36}$$

$\Delta E_j^\pm$ is the change in the energy of the system as the electron tunnels through junction j and is given by (see Figure 18)

$$\Delta E_1^\pm = \Delta U^\pm \mp eV_1, \quad \Delta E_2^\pm = \Delta U^\pm \pm eV_2 \tag{37}$$

where $\Delta U^\pm$ is the energy required to change the charge of the NP, Q, by $\pm 1e$:

$$\Delta U^\pm = \frac{(Q \pm e)^2}{2C_\Sigma} - \frac{Q^2}{2C_\Sigma} = \frac{\pm 2Qe + e^2}{2C_\Sigma} = (\pm 2Q/e + 1)E_C \tag{38}$$

and $E_C = e^2/2C_\Sigma$ is the single-electron charging energy of a neutral NP.

Solving the integral in eq 36 (see Appendix C), we get the following:

$$\Gamma_j^\pm = \frac{1}{e^2 R_j} \frac{(-\Delta E_j^\pm)}{1 - \exp(\Delta E_j^\pm / k_B T)} \tag{39}$$

At absolute zero, this reduces to

$$\Gamma_j^\pm(0\text{K}) = \begin{cases} -\Delta E_j^\pm / e^2 R_j & \Delta E_j^\pm < 0, \\ 0 & \Delta E_j^\pm \geq 0 \end{cases} \tag{40}$$

Therefore, at $T = 0$ K, the condition under which the tunneling rates are nonvanishing is $\Delta E_j^\pm < 0$. Assuming a symmetric double junction, i.e., $R_1 = R_2$ and $C_1 = C_2$, and taking $Q = 0$ (no initial charge on the NP), this condition and eqs 37 and 38 give $-E_C < eV_b/2 < E_C$. Thus, we obtain a threshold voltage of Coulomb blockade, V_{CB}, for a symmetric double junction:

$$|V_{CB}| = 2E_C/e \tag{41}$$

The current at $T = 0$ K is then given by

$$I = e(\Gamma_1^+ - \Gamma_1^-) = e(\Gamma_2^- - \Gamma_2^+) = \begin{cases} \dfrac{V - |V_{CB}|}{2R} & V > |V_{CB}|, \\ 0 & -|V_{CB}| < V < |V_{CB}|, \\ \dfrac{V + |V_{CB}|}{2R} & V < -|V_{CB}| \end{cases} \tag{42}$$

We note that, when deriving eq 42, we did not consider multielectron charging of the NP. Multielectron charging can give rise to stepwise increases in the current at certain higher voltages at which these charging processes become energetically favorable. These steps in current are known as "Coulomb staircase". Coulomb blockade and often Coulomb staircases have been observed in studies involving individual NPs using nanometer-separated electrodes,[177,178,181,182,192−195,197] STM,[246−259] or electrochemical methods.[260−262] For example, Figure 19 shows an $I-V$ curve of a single Au NP device at 4.2 K. The device was fabricated by evaporating Au grains on nanometer-separated Au electrodes created by electromigration. The $I-V$ curve exhibits both a Coulomb blockade gap around zero bias and steps at higher voltages. Fit to the data shows that the $I-V$ characteristics can be well-described using the orthodox model.[245]

As the temperature increases, the tunneling rate inside the CB region becomes nonzero. At zero bias and a temperature range of $0 < k_B T \ll E_C$, the tunneling rate (eq 39) becomes

$$\Gamma_j^\pm(0\text{V}) = \frac{E_C}{e^2 R_j} \exp\left(-\frac{E_C}{k_B T}\right) \tag{43}$$

One can show that zero-bias conductances in this temperature range also follow an Arrhenius behavior with an activation energy equal to E_C (see Appendix D for a derivation). Conductance about zero volts inside the CB region arises essentially from electrons that have energies higher than $E_C + E_F$. The number of these electrons can be calculated using the Fermi−Dirac distribution:

$$\int_{E_C+E_F}^{\infty} f(E)\, dE = \int_{E_C+E_F}^{\infty} \frac{dE}{1 + \exp[(E - E_F)/k_B T]} \propto \int_{E_C+E_F}^{\infty} e^{-(E-E_F)/k_B T}\, dE = k_B T\, e^{-E_C/k_B T} \approx e^{-E_C/k_B T} \tag{44}$$

In the above equation, the Fermi−Dirac distribution is approximated by the Boltzmann distribution. Also, the temperature dependence of the pre-exponential term, $k_B T$, is neglected compared with that of the exponential, $\exp(-E_C/k_B T)$.

A number of studies of NP arrays have reported observing single-electron charging effects. Brust and co-workers[61] and Zhong and co-workers[152,263] have studied conductivities of 3D films of Au NPs cross-linked with various alkanedithiols. Brust et al. prepared small pellets by pressing precipitates of dithiol-linked 2.2 and 8 nm Au NPs. The smaller NPs were cross-linked during synthesis, and larger NPs were cross-linked after synthesis. Zhong and co-workers used a cross-linking/precipitation method to prepare films of decanethiolate-capped 2, 4, or 5 nm Au NPs cross-linked by α,ω-alkanedithiols ($HS(CH_2)_nSH$, $n = 3$, 5, 8, 9, and 10). Films were precipitated on IDA electrodes. The two studies found that films exhibited Arrhenius behavior from room temperature down to ~100 and ~210 K, respectively. Films made of smaller NPs exhibited larger activation energies and smaller conductivities, as expected. Brust et al.[155,156] and Fishelson et al.[159] studied multilayer films of 6−8 nm Au NPs cross-linked by $HS(CH_2)_nSH$ ($n = 5$, 6, 8, 9, and 12) and observed similar behavior. Quinn et al.[126,127] studied conductances of films of 10.2, 6.8, and 3.8 nm diameter $CoPt_3$ NPs. NPs were stabilized by 1-adamantanecarboxilic acid and hexadecylamine ligands. They prepared films by drop-casting NP solutions on IDA electrodes and then mildly thermally annealing the films to reduce inter-NP separation to ~2.8 nm. Conductances of these films exhibited Arrhenius behavior. They reported activation energies of ~28−34 meV for 3.8 nm, ~12−13 meV for 6.8 nm, and ~7 meV for 10.2 nm NPs. The energies scaled with NP size, with the smallest NP having the largest activation energy.

The dependence of activation energies on NP size suggests that they arise from charging of NPs. Obtaining an exact expression for the charging energy for NP arrays is a

nontrivial problem and requires numerical calculation of the capacitance of the NP ensemble, taking into account cross-capacitances since charges on one NP can polarize neighboring NPs. A simple approach is to approximate the neighboring NPs as a conducting continuum separated from the central NP by an insulating shell, as shown in Figure 20.[223]

In this approximation, the capacitance of the NP is

$$C = 4\pi\varepsilon_0\varepsilon_r\left(\frac{1}{R} - \frac{1}{R+s}\right)^{-1} = 4\pi\varepsilon_0\varepsilon_r\frac{R(R+s)}{s} \quad (45)$$

and the charging energy can be expressed as

$$E_C = \frac{e^2}{8\pi\varepsilon_0\varepsilon_r}\left(\frac{1}{R} - \frac{1}{R+s}\right) = \frac{e^2}{8\pi\varepsilon_0\varepsilon_r}\frac{s}{R(R+s)} \quad (46)$$

Equation 46 predicts that E_C increases as R decreases

$$\frac{\Delta E_C}{E_C} = -\Delta R\left(\frac{1}{R} + \frac{1}{R+s}\right) \approx -2\frac{\Delta R}{R} \quad (R \gg s) \quad (47)$$

as observed.

The dependence of the charging energy on the length of molecular spacers is more complex. Molecular spacers can affect the charging energy through two parameters in eq 46: the inter-NP separation, s, and the dielectric constant, ε_r. As s increases, E_C increases,

$$\frac{\Delta E_C}{E_C} = \Delta s\left(\frac{1}{s} - \frac{1}{R+s}\right) = \Delta s\left(\frac{R}{s(R+s)}\right) \approx \frac{\Delta s}{s} \quad (R \gg s) \quad (48)$$

and as ε_r increases, E_C decreases:

$$\frac{\Delta E_C}{E_C} = -\frac{\Delta\varepsilon_r}{\varepsilon_r} \quad (49)$$

Zabet-Khosousi et al.[166] studied conductances of multilayer films of $HS(CH_2)_nSH$-linked Au NPs. Films were deposited in a stepwise fashion onto nanometer-separated Au electrodes. For $n \geq 5$, films exhibited Arrhenius behavior at temperatures higher than ~100 K, with activation energies increasing with n as predicted by eq 48. Wang et al.[263] measured activation energies of films of decanethiol-capped 2 or 4 nm Au NPs prepared by cross-linking/precipitation using $HS(CH_2)_nSH$ (n = 3, 5, 8, 9, 10) and IDA electrodes. Activation energies increased with n in very good agreement with eq 48. Murray and co-workers[122,123] studied conductivities of films of $CH_3(CH_2)_{n-1}S$-capped 2.2 nm Au NPs with various n in a temperature range of ~270−340 K. The films were prepared by drop-casting solutions of capped NPs onto IDA electrodes. All films exhibited Arrhenius behavior. Activation energies generally increased with n, exhibiting a trend predicted by eq 48. Murray and co-workers have also compared the observed activation energies to the predictions of Marcus theory of electron transfer. According to Marcus theory,[264,265] the free energy of activation, ΔG_a, for an electron-transfer reaction is given by

$$\Delta G_a = \frac{\lambda}{4}\left(1 + \frac{\Delta G^\circ}{\lambda}\right)^2 \quad (50)$$

where ΔG° is the standard free energy of the reaction (and equals zero for a self-exchange reaction) and λ is an "outer-sphere" reorganization energy due to the repolarization of the surrounding dielectric medium. For charge transfer between two spheres, the theory gives

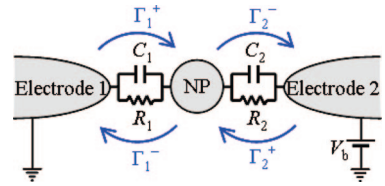

Figure 17. Schematic and equivalent circuit of a double tunnel junction system composed of an NP between two electrodes.

$$\Delta G_a = \frac{\lambda}{4} = \frac{e^2}{16\pi\varepsilon_0}\left(\frac{1}{2R_1} + \frac{1}{2R_2} - \frac{1}{R_1+R_2+s}\right)\left(\frac{1}{\varepsilon_{op}} - \frac{1}{\varepsilon_s}\right) \quad (51)$$

where R_1 and R_2 are radii of the spheres, $R_1 + R_2 + s$ is the center-to-center separation, and ε_{op} and ε_s are, respectively, the optical and static dielectric constants of the medium. Murray and co-workers have found that, although eq 51 can qualitatively describe the observed trend in the variations of activation energies with inter-NP separation, it yields values that are generally much smaller than those observed.[123,240]

Wuelfing et al.[240] and Wessels et al.[163] studied films of Au NPs comprising conjugated molecular spacers to explore the role of molecular chemical structure on charging energy. They did not observe a clear relationship between activation energies and the structure of molecular spacers predicted by the above simple model (eq 46). For example, multilayer films of Au NPs cross-linked with 1,4-cyclohexanedimethylthiol and benzenedimethanethiol exhibited similar activation energies (the molecules have similar sizes); yet, films of phenylethylthioate-capped Au NPs exhibited activation energies higher than films of phenylbutanethiolate-capped NPs, even though the inter-NP separation in the latter system ($s \approx 1.4$ nm) is larger than that in the former ($s \approx 1.0$ nm).

Torma et al.[207] studied the influence of chemical binding on activation energies of covalently and noncovalently linked 1.4 nm Au NPs. In the latter, the NPs were linked via van der Waals or ionic interactions. They prepared NP films by pressing precipitates of linked NPs into pellets and used silver paint to make electrical contacts to the top and bottom of the pellets. The films exhibited Arrhenius behavior in a temperature range of ~200−300 K. In the case of noncovalently linked NPs, activation energies showed a linear relation with inter-NP separation with minor dependence on the chemical nature of linker molecules (i.e., degree of conjugation, structure, etc.). On the other hand, when NPs were covalently linked by dithiols, activation energies were characteristically lower but did not exhibit a uniform dependence on inter-NP separation (see Figure 21).

Differences in conductances of chemically bonded versus nonbonded molecules have also been reported in single-molecule studies. For example, Lindsay and co-workers[214,215] have measured conductances of alkanedithiols inserted into an alkanethiolate monolayer on Au(111) surface. The free thiol groups of the alkanedithiols were bound to Au NPs by immersing the monolayer in a solution of 2 nm triphenylphosphine-capped Au NPs. Using CP-AFM, they observed that the bound alkanedithiols exhibited higher conductances and smaller tunneling decay constant than the nonbonded alkanethiols. In view of the widely varying results, further studies are necessary to clarify the influence of molecular spacers on charging energies of NP assemblies.

One of the challenges associated with rationalizing electron transport in NP assemblies is that these systems are usually

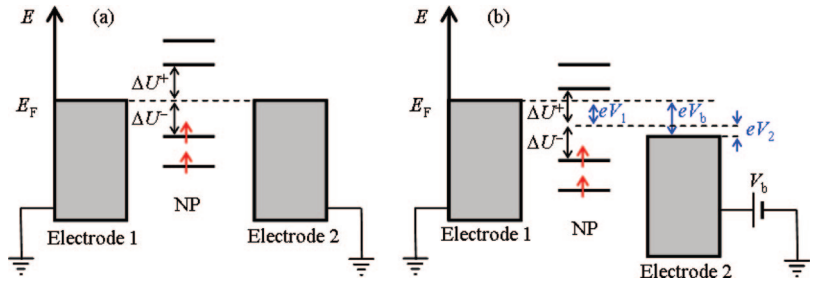

Figure 18. Energy diagram for a double-tunnel junction system composed of an NP between two metal electrodes at (a) $V_b = 0$ and (b) $V_b > 0$. Red arrows denote electrons on the NP.

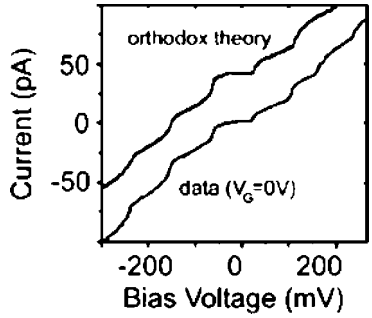

Figure 19. $I-V$ curve for a single NP device at 4.2 K, along with an orthodox model fit (offset for clarity). The device was fabricated by evaporating Au grains on nanometer-separated Au electrodes created by electromigration. Reprinted with permission from ref 195 (Ralph's group). Copyright 2004 American Institute of Physics (http://dx.doi.org/10.1063/1.1695203).

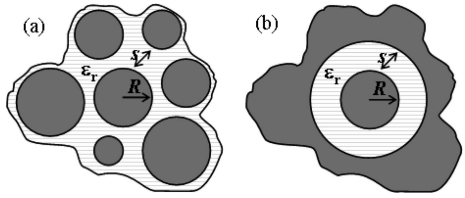

Figure 20. (a) Conducting NP of radius R separated from neighboring NPs by an average distance s. The NPs are embedded in an insulating medium with dielectric constant ε_r. (b) NP in (a) is modeled as a sphere separated from a conducting surrounding by an insulating shell with thickness s and dielectric constant ε_r.

disordered. Viewing adjacent NPs in an assembly as being connected by local conductances, g,

$$g \approx e^{-\beta s}\, e^{-E_C/k_B T} \tag{52}$$

the assembly can be modeled as a series−parallel combination of local conductances, where structural disorder can give rise to variations in s, E_C, and, therefore, g. Even for a perfectly ordered NP assembly, disorder can arise from background charges that can generate local fields and shift NP charging energies. The effect of certain types of disorder on the conductance of tunnel junction arrays has been investigated using Monte Carlo simulations in 1D and 2D.[266−270] In these simulations, disorder was incorporated by taking into account random background charges as well as variations in NP size and capacitances between adjacent NPs. These studies have proposed a scaling law for $I-V$ characteristics of the arrays,

$$I \propto (V - V_T)^{\zeta} \tag{53}$$

where V_T is a Coulomb blockade voltage threshold below which current is zero and ζ is a scaling exponent that depends on array dimensionality. Such a scaling law was predicted

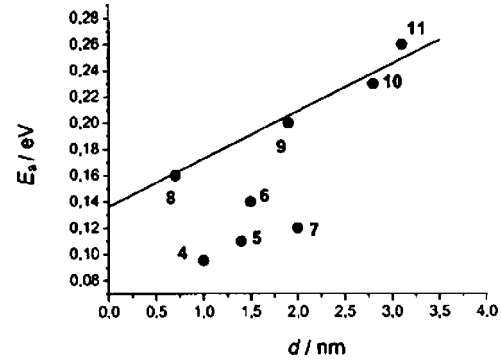

Figure 21. Activation energy vs inter-NP separation for covalently (4−7) and noncovalently (8−11) linked NP films (for structures of linker molecules, see Table 2). Reprinted with permission from ref 207 (Schmid's group). Copyright 2003 Wiley-VCH Verlag GmbH & Co. KGaA (http://dx.doi.org/10.1002/ejic.200390143).

by Middleton and Wingreen (MW) for $T = 0$ K.[266] Theory predicts that $\zeta = 1$ and 5/3 for infinite 1D and 2D arrays, respectively, and numerical simulations indicate that $\zeta \approx 2$ for finite 2D arrays.[266]

A number of groups have observed the MW scaling law using weakly coupled NP assemblies. Reported values of ζ include the following: $\zeta = 2.25 \pm 0.1$ for monolayers of close-packed dodecanethiolate-capped Au NPs (2.2−6.5 nm) prepared by drop-casting (see Figure 22a);[271,272] $\zeta = 3.5$ for 3D films of Pd/Sn NPs (2 nm Pd core protected by a tin oxide envelope) prepared by depositing NPs on nanometer-separated electrodes;[273] and $2.2 < \zeta < 2.8$ for films containing a few close-packed monolayers of 1.4 nm Au,[274] 10 nm Co,[129] 3.8 and 10.2 nm $CoPt_3$,[124,125] or 5.5 nm PbSe[133] NPs prepared by drop-casting and often subsequent annealing to reduce inter-NP separation. Since ζ is related to the dimension of the array, observed sample-dependent variations in ζ can provide information about the array's overall structure: if only one (or a small number of) preferred pathway(s) contribute to conduction, then one expects $\zeta \approx 1$ as the device is essentially 1D, etc. For example, Xu et al.[185] have observed $\zeta = 1.7$ for multilayer films of BDMT-linked 5.3 nm Au NPs constructed on 20-nm-spaced electrodes. This value of ζ suggests that current in these films is mainly passing through quasi-1D pathways.

One can also obtain voltage thresholds, V_T, from fitting $I-V$ data to the scaling law. Parthasarathy et al.[271] have observed that V_T of spatially ordered monolayers of dodecanethiolate-capped Au NPs scaled with the number of NPs bridging electrodes, but V_T of disordered monolayers varied from sample to sample since the number of bridging NPs was poorly defined (see Figure 22b). A number of studies have also reported that V_T decreases linearly with increasing temperature (Figure 23).[133,272,275,276] Parthasarathy et al.[272]

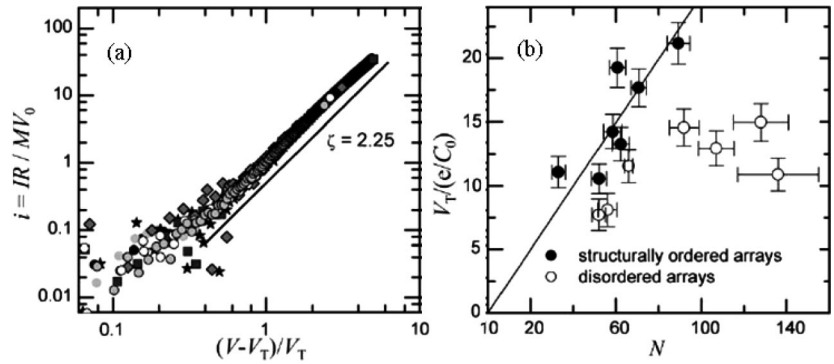

Figure 22. (a) Log−log plot of normalized current vs voltage beyond threshold. Data were obtained using close-packed monolayers of dodecanethiolate-capped Au NPs. M is the width of the array, V_0 is a single-NP Coulomb blockade voltage, and R is a fitting parameter. (b) Threshold voltage, V_T, in units of V_0, versus array length. N is the number of NPs bridging electrodes. A fit to $V_T = \alpha N V_0$ gives $\alpha = 0.25$ for structurally ordered arrays. Reprinted with permission from ref 271 (Jaeger's group). Copyright 2001 American Physical Society (http://dx.doi.org/10.1103/PhysRevLett.87.186807).

have developed a percolation-based model to explain the observed V_T-T relationship. The model assumes that, at a finite temperature T, a fraction of junctions $p(T)$ can overcome their charging energies via thermal fluctuations ($\sim k_B T$) and behave as ohmic junctions. $p(T)$ is expected to increase with T. At some temperature, T^*, the fraction $p(T^*)$ becomes large enough that a percolating pathway of ohmic junctions will be created through the array. V_T for such a pathway is zero. V_T for $T < T^*$ then can be expressed as

$$V_T(T) = V_T(0)[1 - p(T)/p(T^*)] \quad (54)$$

$p(T^*)$ is given by the percolation threshold (p_c) of the underlying lattice of the array. For example, for a 2D hexagonal close-packed (hcp) lattice, $p_c \approx 0.347$. They derived an expression for $p(T)$ based on the distribution of charging energies in the array: $p(T) \approx 4.8 k_B T/\bar{E}_C$, where $\bar{E}_C$ represents an average of charging energies in the array. Thus, the T-dependence of V_T can be expressed as

$$V_T(T) = V_T(0)[1 - \alpha T] \quad (55)$$

where $\alpha = 4.8 k_B/p_c \bar{E}_C$. Equation 55 agrees well with experimental data.[133,272] For $T > T^*$, V_T vanishes and conductance at 0 V exhibits Arrhenius behavior.[272]

4.3. Varying Wave Function Overlap

Single-electron charging effects can be exhibited by a junction (or an array of junctions) if junction conductance, g, is smaller than the quantum of conductance, $g_Q = 2e^2/h \approx (13\ \text{k}\Omega)^{-1}$. This requirement ensures that charges can flow by tunneling and yet are sufficiently localized so that charge states of the junction are well-defined. In terms of the energy-time uncertainty principle, the (dis)charging time due to tunneling, $\tau \approx RC$, must be sufficiently long that the corresponding uncertainty in energy is smaller than the charging energy, $E_C = e^2/2C$. That is, for short times ($g > g_Q$), the uncertainty in energy is sufficiently large to overcome the charging energy. Single-electron charging effects are then suppressed as quantum couplings become strong and charges become delocalized.[277] This result has been experimentally demonstrated. A number of studies of tunnel junction arrays have reported transitions from Coulomb blockade to ohmic or superconducting behavior at $g \approx g_Q$.[278−280] For example, Geerligs et al.[280] have observed that charging effects are strongly suppressed in aluminum tunnel junctions when tunneling resistances are near or below 10 kΩ. Junctions with higher resistances exhibited Coulomb blockade. Orr et al.[278] have studied a crossover to superconductivity in ultrathin 2D films of Sn evaporated on alumina substrates. Films with sheet resistance of 3.6 kΩ were superconducting at 3.5 K, whereas films with sheet resistance of 10 kΩ were not.

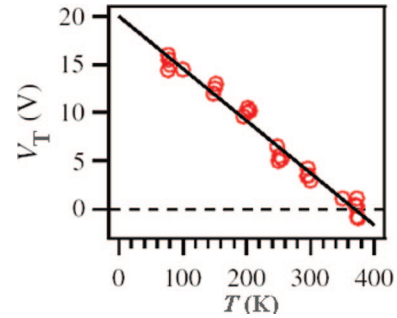

Figure 23. Temperature dependence of voltage threshold for films of ~5.5 nm PbSe NPs. Solid line is a fit to data. Reprinted with permission from ref 133 (Drndic's group). Copyright 2005 American Physical Society (http://dx.doi.org/10.1103/PhysRevLett.95.156801).

Such quantum coupling transitions are expected for NP assemblies when wave function overlap between NP becomes sufficiently strong. Liu et al.[281] have studied $CH_3(CH_2)_{n-1}S$-capped 1.7 nm Au NPs as a function of the inter-NP separation ($n = 6, 9, 12, 15$) using valence-band photoemission spectroscopy (Figure 24). For $n \geq 9$, they observed a low density of states at the NP Fermi level. This can be due to the large charging energy of the small NPs. For $n = 6$, however, they observed an increase in the density of states at the Fermi level. The increase can be attributed to electron delocalization for sufficiently small inter-NP separation.

The transition to delocalized behavior can also be observed optically. Heath and co-workers[47,282−284] studied linear and nonlinear optical response of $CH_3(CH_2)_{n-1}S$-capped Ag NP monolayers as a function of inter-NP separation. They utilized a Langmuir trough to compress NP monolayers from $\delta/2R \approx 1.7$ to 1.1, where R is the NP radius and δ is the center-to-center NP separation ($\delta = 2R + s$). They found that, for $\delta/2R > 1.3$, linear optical responses (e.g., reflectance) could be well-described by a classical coupling model involving changes in polarizability[283] or dielectric constant.[284] For smaller values of $\delta/2R$, predictions of the classical model diverged strongly from experimental observations (Figure 25a). Nonlinear response (e.g., second-order susceptibility) exhibited an exponential dependence on $\delta/2R$,

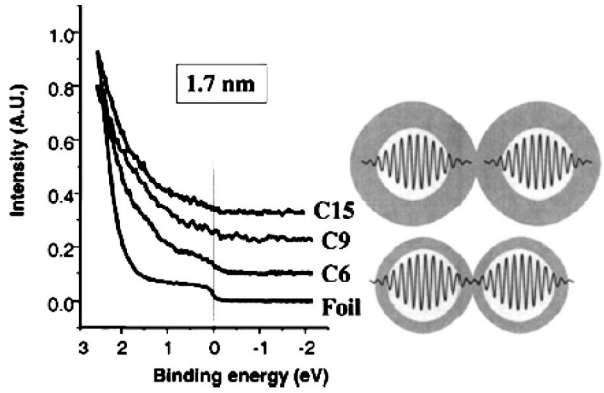

Figure 24. Effect of inter-NP separation (as determined by the length of alkyl chains in the NP ligand) on the density of states of $CH_3(CH_2)_{n-1}S$-capped 1.7 nm Au NPs. The spectrum of a pure gold foil is shown for comparison. Reprinted with permission from ref 281 (Salmeron's group). Copyright 2005 American Physical Society (http://dx.doi.org/10.1103/PhysRevB.72.155430).

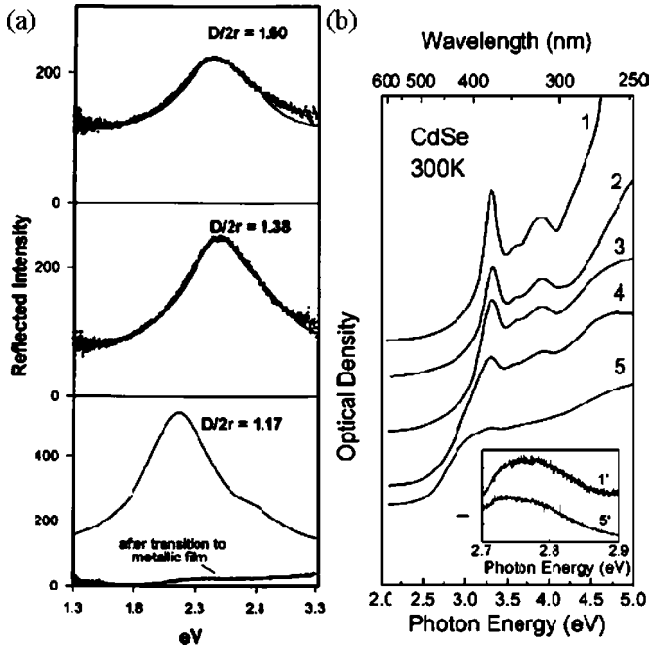

Figure 25. (a) Comparison of reflectance spectra of compressed Langmuir monolayers of Ag NPs at three values of $\delta/2R$. Predictions of a classical model are shown as solid lines and experimental data as points. Reprinted with permission from ref 283 (Heath's group). Copyright 1998 American Chemical Society (http://dx.doi.org/10.1021/jp981315s). (b) Absorption spectra of 1.6 nm CdSe NPs. Spectra are shown in order of increasing NP concentration from top to bottom. Spectra 1−4 were obtained using NP/poly(ethylene glycol) composite films with polymer volume fractions of 37%, 18%, 3%, 1%, respectively. Spectrum 5 was obtained using a close-packed film of CdSe NPs. Reprinted with permission from ref 285 (Gaponenko's group). Copyright 1999 American Physical Society (http://dx.doi.org/10.1103/PhysRevB.60.1504).

implying strong quantum coupling between NPs. For $\delta/2R < 1.2$, optical properties of the monolayer resembled those of a thin metallic Ag film. The transition to delocalized behavior was reversible upon increasing the inter-NP separation. Artemyev et al.[285,286] have studied optical properties of CdSe NP films at 300 K. They prepared NP films on quartz substrates by drop-casting pyridine solutions containing 1.6 nm CdSe NPs and varying amounts of poly(ethylene glycol). The inter-NP distance in the films was varied from ~0.6 to 1 nm by changing the relative concentration of CdSe NPs and polyethylene glycol. Figure 25b shows the absorption spectra of the films. At large inter-NP distances, the spectra exhibit a finite number of discrete bands due to quantum confinement in NPs. At small inter-NP distances, the spectra become smooth, resembling those of bulk semiconductors. Bawendi and co-workers[28] have reported similar observations using films of pyridine-capped CdSe NPs. As the distance between NPs was reduced by applying a vacuum and gently heating the films, the optical absorption spectra approached that for the bulk CdSe. These observations point to a transition from individual (localized) to collective (delocalized) electronic states of NPs.

4.4. Metal−Insulator Transition (MIT)

Materials are classified as metals or nonmetals depending on the behavior of their conductance as $T \rightarrow 0$.[287] For nonmetals, conductance tends to zero; for metals, it tends to a finite value. This can be rationalized given their electronic band structures. In nonmetals, the energy bands are either completely filled or completely empty, and in metals, at least one band is partially filled. The latter can participate in conduction.

Partially filled bands in nonmetals can be generated by exciting electrons over the energy gap, E_g, between the highest occupied (valence) band and the lowest unoccupied (conduction) band. At nonzero T, there is a finite probability that some electrons will overcome the energy gap through thermal activation. Therefore, the conductivity of nonmetals tends to increase with temperature. Conductivity of a metal, on the other hand, tends to decline with increasing temperature. According to the Drude theory of metals, the conductivity of a metal is given by[287]

$$\sigma = \frac{ne^2\tau}{m} \tag{56}$$

where n is the density of conducting electrons and τ is mean free time. τ is determined by electron scattering, which can be categorized as elastic (e.g., impurity or defect scattering) and inelastic (e.g., electron−electron or electron−phonon scattering). The mean free time associated with these processes can be written as (Matthiessen's rule)

$$\frac{1}{\tau} = \frac{1}{\tau_{\text{elastic}}} + \frac{1}{\tau_{\text{inelastic}}} \tag{57}$$

and the conductivity of metals can be written as

$$\sigma^{-1} = \sigma_0{}^{-1} + \sigma(T)^{-1} \tag{58}$$

At very low temperatures, τ_{elastic} dominates since it is independent of temperature. At higher temperatures, $\tau_{\text{inelastic}}$ becomes significant and gives rise to a temperature-dependent conductivity. Assuming that the rate of inelastic scattering due to electron−phonon interactions increases as $\sim k_B T$, metallic conductivity decreases as $\sim 1/k_B T$ and resistivity increases linearly with T.[287] Note that not all metals exhibit this trend at all temperatures; that is, it is possible for a material to exhibit finite conductivity as $T \rightarrow 0$ (metallic behavior) and decreasing resistivity with increasing T at some temperatures (for example, see section 4.4.2).

Studies of molecularly linked metal−NP assemblies show evidence of metal−insulator transitions (MITs) as a function of inter-NP separation. Zabet-Khosousi et al.[166] have studied resistances of multilayer films of $HS(CH_2)_nSH$-linked 5 nm Au NPs. They prepared films on nanometer-separated electrodes using a stepwise self-assembly method and

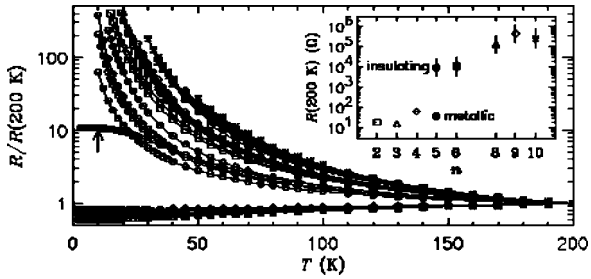

Figure 26. Normalized resistances of multilayer films of $HS(CH_2)_nSH$-linked Au NPs vs temperature. Inset: Resistance of the films at 200 K as a function of n. Reprinted with permission from ref 166 (Dhirani's group). Copyright 2006 American Physical Society (http://dx.doi.org/10.1103/PhysRevLett.96.156403).

measured resistance, R, of the films with various n ($n = 2-6$, 8, 9, 10) as a function of temperature (Figure 26). R at $T = 2$ K and $T = 200$ K as well as trends in R vs T all pointed to an MIT occurring at $n = 5$. As T approached 2 K, two distinct types of behaviors were observed: films with $n \leq 4$ exhibited resistances tending to a finite value, indicating metallic behavior, whereas films with $n \geq 6$ exhibited rapidly increasing resistance, indicating nonmetallic behavior. Both types of behaviors were observed among various films with $n = 5$. At intermediate temperatures, films with $n \leq 4$ and $n \geq 6$ exhibited positive and negative values of dR/dT, respectively, consistent with metallic and nonmetallic behaviors. Again for $n = 5$, both behaviors were observed. The inset of Figure 26 shows resistance of the films at 200 K as a function of n. From $n = 2$ to $n = 5$, resistance changed by <1 order of magnitude for metallic films; from metallic to insulating films, with $n = 5$, resistance jumped by ~2 orders; thereafter, for $5 \leq n \leq 10$, resistance changed by another ~2 orders for nonmetallic films, growing exponentially with n. The latter is consistent with a tunneling mechanism as expressed by eq 32.

Quinn et al.[125,127] studied an MIT in $CoPt_3$ NP assemblies by tuning inter-NP separation. They prepared multilayer films of 3.8 nm $CoPt_3$ NPs on IDA electrodes by drop-casting. The NPs were stabilized with 1-adamantanecarboxylic acid and hexadecylamine ligands initially, and inter-NP separation was varied by thermal annealing. As-prepared films exhibited high resistances exceeding 1 TΩ at room temperature. After annealing under reducing conditions (5% H_2, 95% N_2 for 1 h; see section 2.2.1), films generally exhibited decreased inter-NP separation and film resistances. Films annealed at 80 °C exhibited room-temperature resistances, R_{RT}, on the order of ~100 MΩ, thermally activated behavior between 3−300 K, and rapidly climbing R as T decreased near 3 K (Figure 27a). At $T = 3$ K, these films also displayed Coulomb blockade in $I-V$ characteristics. Films annealed at 100 °C exhibited $R_{RT} \approx 190$ kΩ and linear $I-V$ characteristics at all measured temperatures. R vs T data of these films displayed two regions (Figure 27b): a region of positive dR/dT for 80 K < T < 300 K, and another of negative dR/dT for 4 K < T < 80 K. As T approached 3 K, R's tended to finite values, implying that these films were metallic by definition. Increasing the annealing temperature to 150 °C produced films with $R_{RT} \approx 1$ kΩ. These films exhibited linear $I-V$ curves, positive dR/dT for 4 K < T < 300 K, and R's that tended to finite values at 4 K (Figure 27c), consistent with metallic behavior.

Heath and co-workers have studied electronic properties of Ag NP monolayers using impedance spectroscopy[137] and scanning tunneling spectroscopy (STM).[138,139] Figure 28 shows impedance spectra of a propanethiolate-capped 3.5 nm Ag NPs in a Langmuir trough at various compressions. For $\delta/2R > 1.3$, spectra could be modeled using an equivalent RC circuit. For $1.2 < \delta/2R < 1.3$, characteristic RC time constants decreased rapidly with decreasing inter-NP separation. Such behavior is consistent with an increasing tunneling rate between NPs. Below $\delta/2R = 1.2$, the film exhibited a transition from an RC- to an inductive-type of behavior, suggesting a transition to metallic conductance. Figure 29 shows results of STM studies using monolayers of decanethiolate and hexanethiolate-capped 2.6 nm Ag NPs. The monolayers were prepared using a Langmuir trough and were transferred onto graphite substrates. Inter-NP separations in these monolayers were ~1.1 and 0.6 nm for $n = 10$ and 6, respectively. Figure 29 shows that normalized conductances of the NP monolayers strongly depend on $\delta/2R$. At $\delta/2R \approx 1.4$, normalized conductance at 0 V vanishes at low temperatures. At $\delta/2R \approx 1.2$, its value at 0 V is equal to 1 and is temperature independent from 300 to 20 K. Since tunneling conductance in STM at low bias is proportional to $\rho_{tip}(E_F)\rho_{sample}(E_F)$ (see eq 23), normalized conductance, defined as $(dI/dV)(V/I)$, provides a good approximation to the local density of states (LDOS). At 0 V, insulators exhibit a vanishing LDOS. Metals exhibit a finite LDOS and a normalized conductance equal to 1. Quinn et al.[221] and Liljeroth et al.[142] observed signatures of an MIT in Langmuir monolayers of alkanethiolate-capped Ag and Au NPs using scanning electrochemical microscopy (SECM). SECM offers a means of distinguishing between insulating and conducting substrates since they give rise to a decrease or an increase in SECM current, respectively (see section 3.1.4). Figure 30 shows SECM approach curves using hexanethiolate-capped 4 nm Ag NP monolayers obtained at various Langmuir trough surface pressures. At surface pressures below and above 42 mN m^{-1}, respectively, the monolayers exhibited a decrease and increase in SECM current as the SECM tip approached the monolayers. Such a transition was reversible upon changing the surface pressure.

4.4.1. Mott−Hubbard MIT

One of the foundations of our understanding of MITs is the Mott−Hubbard model, proposed originally in a context of a lattice of hydrogen atoms.[288] Consider such a lattice at absolute zero and with variable lattice spacing, s. In the limit $s \rightarrow \infty$, overlap between atomic wave functions is negligible, and electrons are localized on individual atoms. For conduction to occur, electrons have to transfer between neutral atoms, creating positively and negatively charged ions. This transfer requires an energy, U, due to the difference between the ionization energy (IE) and the electron affinity (EA) of hydrogen atoms. U is the energy cost of having electrons on the same site and is known as the Hubbard energy.[289] Because of this energy cost, conduction at 0 K is suppressed, and the lattice is insulating. For finite s, the overlap between atomic wave functions is nonzero and gives rise to energy bands as per the band theory of solids. The widths, Δ_i, of energy bands, i, depend on the magnitude of overlap integrals between atomic wave functions and increase as interatomic spacing decreases.[287] The energy gap for conduction, E_g, then reduces to $E_g = U - (\Delta_1 + \Delta_2)/2$ (see Figure 31). As s decreases further, the bandwidths Δ_1 and Δ_2 increase until, at $U \approx (\Delta_1 + \Delta_2)/2$, the energy gap for conduction disappears, and the lattice becomes metallic. The Mott−Hubbard model applied to a lattice of hydrogen atoms predicts onset

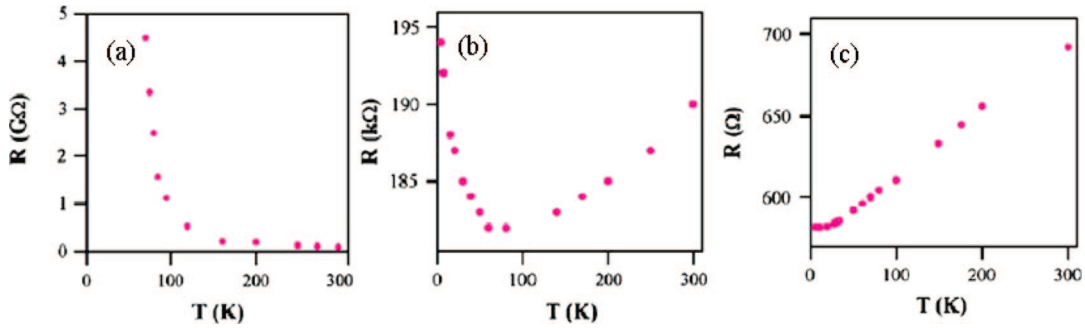

Figure 27. Typical resistance−temperature data for $CoPt_3$ NP films annealed at (a) 80 °C, (b) 100 °C, and (c) 150 °C. The films were prepared by drop-casting 3.8 nm $CoPt_3$ NPs on IDA electrodes at room temperature. Reprinted with permission from ref 127 (Redmond's group). Copyright 2005 Elsevier (http://dx.doi.org/10.1016/j.progsolidstchem.2005.11.048).

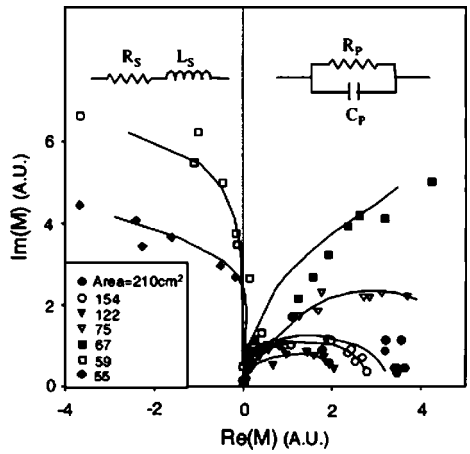

Figure 28. Plot of the frequency-dependent dielectric modulus, *M*, in the complex plane, for a Langmuir monolayer of propanethiolate-capped 3.5 nm Ag NPs at various surface pressures. Insets show equivalent circuits of the monolayer in metallic and nonmetallic limits, respectively. Reprinted with permission from ref 137 (Heath's group). Copyright 1998 American Physical Society (http://dx.doi.org/10.1103/PhysRevLett.80.3807).

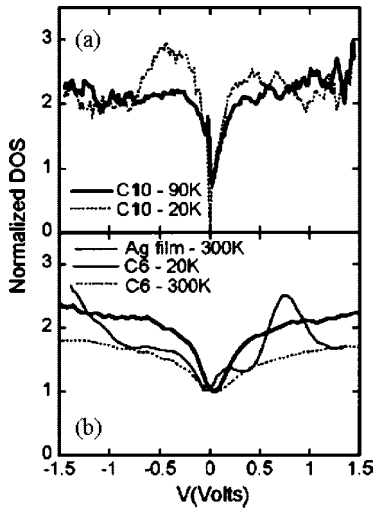

Figure 29. Normalized density of states (DOS) vs voltage for films of (a) decanethiolate-capped and (b) hexanethiolate-capped 2.6 nm Ag NPs at different temperatures. Reprinted with permission from ref 138 (Heath's group). Copyright 1998 American Physical Society (http://dx.doi.org/10.1103/PhysRevB.59.1633).

of metallic behavior at $s \approx 4.5a_0$,[290] where a_0 is the Bohr radius appearing in hydrogen atom wave functions, $\psi_H(r)$. For a 1-s state, $\psi_H(r) \approx \exp(-r/a_0)$.

An analogous Mott−Hubbard MIT can be realized in NP assemblies where NPs serve as artificial atoms. Here, the

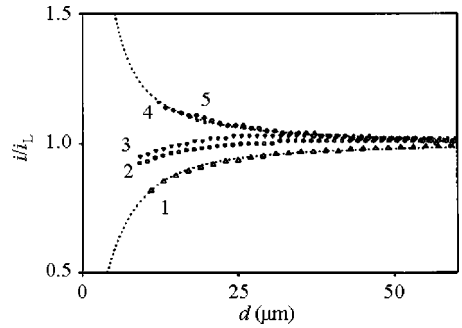

Figure 30. SECM approach curves obtained using a hexanethiolate-capped 4 nm Ag NP monolayer at various Langmuir trough pressures: (1) 0 mN m^{-1} (open barrier position); (2) 11 mN m^{-1}; (3) 22 mN m^{-1}; (4) 42 mN m^{-1}; and (5) 56 mN m^{-1} (closed barrier position). *i* and i_L are the tip current at a given tip−substrate distance (*d*) and in the bulk, respectively. Dotted lines represent theoretical fits assuming substrates are insulating (lower) or conducting (upper). Reprinted with permission from ref 221 (Bard's group). Copyright 2001 American Chemical Society (http://dx.doi.org/10.1021/jp010970o).

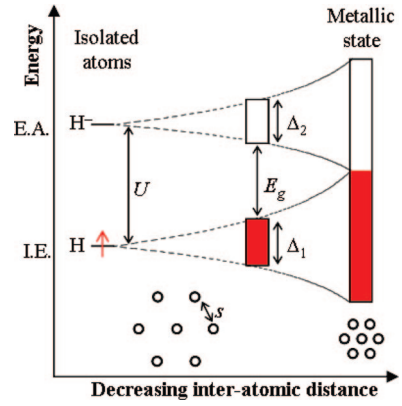

Figure 31. Evolution of energy levels in a lattice of hydrogen atoms during MIT.

energy gap arises from the NP charging energy (i.e., Coulomb gap). The energy bands arise from the overlap between NP wave functions: $\psi(r) \approx \exp(-\kappa r)$ and $\kappa \approx (2m^*\phi)^{1/2}/\hbar$ where m^* is an effective mass of electrons. The wave function decay constant, κ, provides a useful length scale in the Mott−Hubbard criterion for the MIT: $a_0 \approx 1/\kappa$. Zabet-Khosousi et al.[166] have applied the Mott−Hubbard model to describe the MIT exhibited by multilayer films of $HS(CH_2)_nSH$-linked Au NPs at $n = 5$ (see Figure 26). Taking $\phi \approx 1.4$ eV and $m^* \approx 0.4 \times$ mass of electron reported for gold−alkanedithiolate−gold tunnel junctions,[291] they obtained $\kappa \approx 4$ nm^{-1}. Applying the Mott−Hubbard criterion, they estimated a critical NP separation for MIT to be ~4.5/

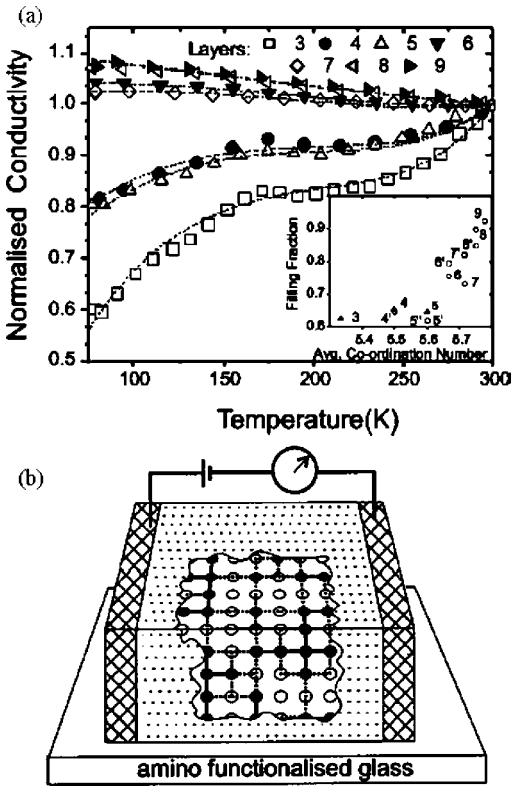

Figure 32. (a) Normalized conductivity vs temperature for 1,4-butanedithiolate-linked Au NP multilayer films with 3−9 layers. Dashed lines are fits obtained using an effective-medium approximation model. (b) Lattice model for disordered arrays of NPs. Filled and open circles denote occupied sites and voids, respectively. Solid lines indicate metallic paths, and dashed lines indicate tunneling/thermionic paths. Reprinted with permission from ref 161 (Dhirani's group). Copyright 2002 American Institute of Physics (http://dx.doi.org/10.1063/1.1495838).

$(4\ \mathrm{nm}^{-1}) = 1.1$ nm, which is consistent with the inter-NP separation using 1,5-pentanedithiol linkers and observation of the transition at $n = 5$.

4.4.2. Percolation-Driven MIT

In order to exhibit global metallic behavior, an assembly of metal NPs must cross a percolation threshold. At this point, strongly coupled NPs that form metallic clusters combine to form at least one continuous, sample-spanning metallic pathway. Although at or just above the transition, the sample may be dominated by nonmetallic conduction, as T tends to 0 K, nonmetallic pathways shut down, and at $T = 0$ K, conductance remains nonzero. Below the threshold, however, metallic clusters are isolated, and overall, the assembly is nonmetallic.

Natan and co-workers[158,206] and Dhirani and co-workers[161,162,164] have studied percolation effects in strongly coupled NP films. In these studies, NP films were prepared by stepwise self-assembly using sufficiently short cross-linker molecules (2-mercaptoethanol, 2-mercaptoethylamine, or 1,4-butanedithiol) to ensure strong inter-NP coupling. Films exhibited conductivities that depended strongly on the number of NP/linker exposure cycles. Above a threshold (typically six exposure cycles), films exhibited high conductivities and metallic behavior. Below, conductivities were thermally activated (Figure 32a). The transition is consistent with a percolation-driven MIT.

Trudeau et al.[161] have modeled the percolation-driven MIT by treating the NP film as a lattice of sites that are connected by random-valued conductances. They then used an effective-medium approximation[292] to model effective bulk conductance. Figure 32b shows details of the model. NPs and voids are represented by filled and empty sites, respectively. A pair of adjacent sites is considered to be connected by conductances that are metallic (g_m), insulating (g_i), or thermally activated (g_t), if they are both filled, both empty, or composed of one of each type, respectively. Denoting the fraction of filled sites in the lattice by p, the probability distribution of conductances is then given by[293]

$$f(g_\alpha, p) = p^2\delta(g_\alpha - g_m) + 2p(1-p)\delta(g_\alpha - g_t) + (1-p)^2\delta(g_\alpha - g_i) \quad (59)$$

where δ represents Dirac's delta function and $\alpha = m$, i, or t. In an effective-medium approximation, the effective conductance of the lattice, g_{eff}, can be obtained by solving the following equation,

$$\sum_{\alpha=g,t,i} \frac{f(g_\alpha, p)(g_{\mathrm{eff}} - g_\alpha)}{g_\alpha + g_{\mathrm{eff}}(z/2 - 1)} = 0 \quad (60)$$

where z is the coordination number of the lattice (e.g., $z = 4$ for square and $z = 6$ for cubic lattices in 2D and 3D, respectively). [161] Using appropriate temperature dependencies for g_m, g_i, and g_t, they obtained fits to the data (fits are shown in Figure 32a). Their results showed that, as p increased, g_{eff} vs T exhibited signs of increased contributions from locally metallic transport. At $p = p_m \approx 0.65-0.70$, a sample-spanning metallic pathway was formed. Just beyond p_m, a combination of metallic and thermally activated transport was observed, with the latter even dominating despite the films' being fundamentally metallic. Combinations of activated and metallic transports NP films have also been observed in a number of other studies.[162,175,176]

4.4.3. Metallic Behavior

Conductivities of Au NPs assemblies are generally lower than that of bulk Au ($\sigma_{\mathrm{Au}} = 4.5 \times 10^5\ \Omega^{-1}\mathrm{cm}^{-1}$).[294] Liu et al.[90] have reported $\sigma = 2 \times 10^5\ \Omega^{-1}\ \mathrm{cm}^{-1} \approx 1/2\ \sigma_{\mathrm{Au}}$, the highest value reported. Films consisted of 15 layers of 4.8 nm Au NPs assembled using an ionic layer-by-layer method. The Au NPs were encapsulated with cationic polymer molecules, poly(diallyldimethylammonium chloride), and then attached to anionic polymer molecules, poly S-119, via electrostatic attractions. Other studies have reported conductivities in the $\sim 10^1-10^3\ \Omega^{-1}\ \mathrm{cm}^{-1}$ range.[158,163] Beecher et al.[125] have observed $\sigma \approx 10^1\ \Omega^{-1}\ \mathrm{cm}^{-1}$ for thermally annealed films of 3.8 nm $CoPt_3$ NPs, over 3 orders of magnitude smaller than that of bulk Pt films ($\sigma_{\mathrm{Pt}} = 9.4 \times 10^4\ \Omega^{-1}\ \mathrm{cm}^{-1}$).[294] The temperature coefficients of resistance, $\mathrm{TCR} \equiv (1/R)(\mathrm{d}R/\mathrm{d}T)$, observed in metallic NP assemblies are also lower than those in bulk metals. For example, Zabet-Khosousi et al.[166] have observed $\mathrm{TCR} \approx 0.001-0.002\ \mathrm{K}^{-1}$ for films of $HS(CH_2)_nSH$-linked Au NPs ($n = 2$ to 5) and $0.0023\ \mathrm{K}^{-1}$ for a 15 nm thick evaporated Au film at 200 K. TCR of bulk Au at 200 K is $0.0055\ \mathrm{K}^{-1}$.[294] Beecher et al.[125] have observed $\mathrm{TCR} \approx 0.001\ \mathrm{K}^{-1}$ for thermally annealed 3.8 nm $CoPt_3$ NP films at 300 K. TCR for bulk Pt at 300 K is $0.0038\ \mathrm{K}^{-1}$.[294]

The observation of lower σ and TCR in NP films compared with corresponding bulk metals suggests that electron-scattering processes are strongly enhanced in NP assemblies.[125,162,166] Elastic electron-scattering decreases zero-

temperature conductivity of samples (σ_0 in eq 58), which in turn gives rise to smaller values of TCR. Elastic scattering is strong since sizes of NPs are typically much smaller than the mean free path, l, of electrons in the bulk material. For example, in a film of 5 nm Au NPs, the time scale for elastic scattering can be estimated as $\tau_{elastic} \approx l/v_F \approx (5 \times 10^{-9}$ m)/(1.4×10^6 m/s) = 3.6 fs, where v_F is the Fermi velocity of electrons in gold. For bulk gold, $l = 41$ nm and $\tau_{elastic} \approx$ 29 fs at 300 K.[295] At 300 K, the time scale for inelastic scattering due to phonons is $\tau_{inelastic} \approx \hbar/k_BT \approx 25$ fs. Therefore, temperature-independent elastic scattering dominates the conductivity of metallic NP films.

4.4.4. Superconducting NP Assemblies

Very little work has been done in the area of superconducting NP assemblies. Wietz et al.[11] studied magnetic susceptibilities of films of lead NPs capped with carboxylic acids ($C_nH_{2n-2}O_2$). They prepared the films by drop-casting solutions of the NPs onto quartz tubes. Inter-NP separation distances were tuned from ~1.1 to ~2.6 nm by varying the length of ligands (from $n = 6$ to $n = 18$). Magnetic susceptibility measurements of the films exhibited a variety of behaviors ranging from insulating to superconducting depending on the inter-NP spacing. Below a superconducting transition temperature, T_C, bulk Pb becomes a perfect diamagnet; that is, it excludes magnetic field except near the surface (Meisner effect). Magnetometry studies of C_{18}-capped Pb NPs with diameters ranging from 15 to 70 nm have shown that only NPs larger than 45 nm exhibit a Meisner effect.[11] Therefore, films made of 20 nm Pb are expected to exhibit magnetic flux exclusion only when coupling between NPs is sufficiently strong and charge becomes delocalized. They observed that films of 20 nm Pb NPs with $n = 12$ or 18 ($s > 2.0$ nm) exhibited no diamagnetic response regardless of applied magnetic field or temperature. This indicates weak inter-NP coupling and insulating film behavior. However, films of 20 nm Pb NPs with $n = 6$ and 8 ($s \approx 1.1$ and 1.5 nm, respectively) exhibited diamagnetic responses below T_C for bulk Pb (7.2 K). Films with $n = 6$ exhibited the strongest diamagnetic response (Figure 33).

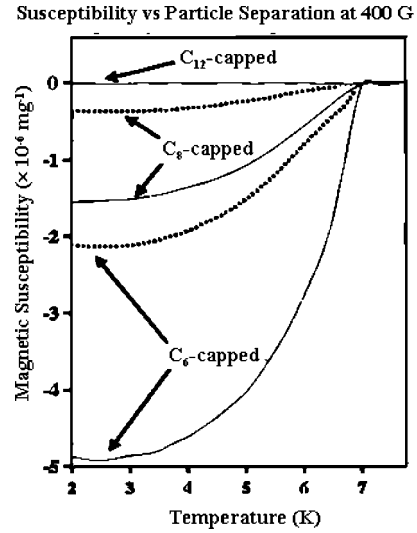

Figure 33. Plots of magnetic susceptibility at 400 G vs temperature using various Pb NP films. The plots are mass-normalized to 1 mg of sample. Reprinted with permission from ref 11 (Heath's group). Copyright 2000 American Chemical Society (http://dx.doi.org/10.1021/jp000238+).

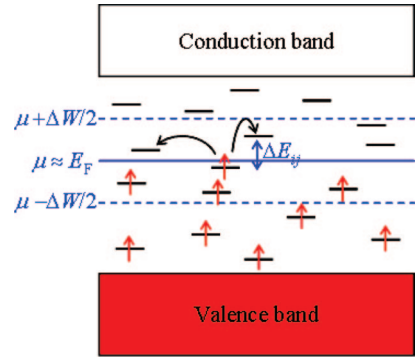

Figure 34. Schematic energy diagram for a doped semiconductor. Short horizontal lines show localized states due to dopant sites. Red arrows represent electrons. Black arrows show electron hopping from an occupied site to an empty site. Dashed lines represent an energy band of width ΔW around the Fermi level.

4.5. Non-Arrhenius Behavior

Several charge transport studies of NP assemblies in the nonmetallic regime have reported deviations from Arrhenius behavior. Observed $g-T$ relationships in these systems can be modeled as

$$g \approx \exp\left[-\left(\frac{T_0}{T}\right)^{\nu}\right] \tag{61}$$

where T_0 is a constant and ν ranges from 0 to 1. $\nu = 1$ represents the Arrhenius behavior. $\nu = 1/2$ has often been observed in studies of NP assemblies[6,131−133,139,141,164,166,185,296−298] and traditional granular films.[223,299−305] In this section, we review models proposed to explain this fractional-ν behavior.

4.5.1. Variable-Range Hopping

A model for explaining fractional-ν behavior exhibited by doped semiconductors was first proposed by Mott (Figure 34).[306] According to this model, carrier charges are localized on dopant sites, i, with energies E_i. Carriers can generate current by acquiring energy thermally and hopping to another site with energy gap $\Delta E_{ij} = E_j - E_i$. Hopping to the nearest-neighbor site is not always the most favorable process, since there is a larger probability of finding sites at larger distances, r_{ij}, that present lower ΔE_{ij}. A countervailing consideration is that it is more difficult to tunnel to sites at larger r_{ij}. Optimization of these two processes leads to a fractional-ν as follows.

Consider a system with a constant density of localized states (ρ number of localized states per unit energy per unit volume) near the Fermi level: $\rho(E) = \rho(E_F)$. Note that "volume" in general may vary with dimension: in 1D, it is a length; in 2D, it is an area; etc. Suppose a charge hops from an occupied state i ($E_i < E_F$) to an empty state j ($E_j > E_F$) within a small band ΔW: $E_j - E_i \leq \Delta W$. The concentration of states (ΔN, number of states per unit volume) in the bandwidth ΔW is given by

$$\Delta N = \rho(E_F)\Delta W \tag{62}$$

Therefore, the average separation between sites i and j is

$$r_{ij} \approx \Delta N^{-1/D} = [\rho(E_F)\Delta W]^{-1/D} \tag{63}$$

where D is the dimensionality of the system.

The probability of tunneling from site i to j is $P_{\text{tunnel}} \approx \exp(-2\kappa r_{ij})$, where κ is the tunneling decay constant. The probability of acquiring an energy, ΔW, thermally is given by the Boltzmann distribution, $P_{\Delta W} \approx \exp(-\Delta W/k_B T)$. The probability of hopping is then given by the product of these two probabilities, since an electron at site i needs to absorb energy ΔW *and* tunnel elastically to site j:

$$P_{\text{hop}} = P_{\text{tunnel}} P_{\Delta W} \approx e^{-2\kappa r_{ij}} e^{-\Delta W/k_B T} \approx \exp\left[-2\kappa r_{ij} - \frac{1}{k_B T \rho(E_F) r_{ij}^D}\right] \quad (64)$$

P_{tunnel} decreases exponentially with r_{ij}, and $P_{\Delta W}$ increases with r_{ij}. Maximizing $P_{\text{hop}}(r_{ij})$ gives rise to an optimum hopping distance, r_{hop},

$$\frac{dP_{\text{hop}}(r_{ij})}{dr_{ij}} = 0 \Rightarrow r_{\text{hop}} \approx \left(\frac{D}{2\kappa\rho k_B T}\right)^{\nu} \quad (65)$$

where $\nu = 1/(D+1)$. The conductivity given by the optimized hopping probability then has a temperature dependence of the form given by eq 61, where $T_0 \approx \kappa^D/k_B\rho(E_F)$. Equation 65 shows that r_{hop} varies with temperature and decreases as $T^{-\nu}$. Such a transport mechanism is known as variable-range hopping (VRH). In nearest-neighbor hopping (NNH), the hopping length, given by the distance between nearest neighbors, does not vary with temperature, and conductivity exhibits Arrhenius behavior. For bulk (3D) doped semiconductors near MIT, the so-called "$\nu = 1/4$ law" has been confirmed experimentally.[307]

In a system where Coulomb interactions are important, Efros and Shklovskii (ES)[308] showed that a $\nu = 1/2$ behavior arises. They argued that, in the presence of Coulomb interactions, the energy increase associated with electron hopping from a filled site i ($E_i < E_F$) to an empty site j ($E_j > E_F$) is

$$\Delta_{ij} = E_j - E_i - \frac{e^2}{4\pi\varepsilon r_{ij}} > 0 \quad (66)$$

where the last term is the Coulomb attraction of an electron−hole pair located at sites j and i, ε is the permittivity of the system, and Δ_{ij} is the net energy change associated with the charge transfer process. If the change were not positive, it could occur spontaneously, and site j would not be above the Fermi level, contrary to our assumptions. The inequality $\Delta_{ij} > 0$ requires that the two sites i and j be separated by a distance

$$r_{ij} > \frac{e^2}{4\pi\varepsilon\Delta E_{ij}} \quad (67)$$

where $\Delta E_{ij} = E_j - E_i$. If both E_i and E_j are close to the Fermi level, then ΔE_{ij} is small, and r_{ij} is large. In other words, the concentration of sites close to E_F should be very low and in particular has to vanish at the Fermi level. According to eq 67, the concentration of sites within a bandwidth ΔW cannot exceed $\Delta N \approx r_{ij}^{-3} = (4\pi\epsilon)^3\Delta W^3/e^6$. The density of states $\rho(\Delta W) = \Delta N/\Delta W$ in the ES model is then bounded by

$$\rho(\Delta W) = \alpha\frac{(4\pi\varepsilon)^3\Delta W^2}{e^6} \quad (68)$$

where α is a numerical coefficient. Therefore, $\rho(\Delta W)$ vanishes at least as $\sim\Delta W^2$, when $\Delta W \to 0$.

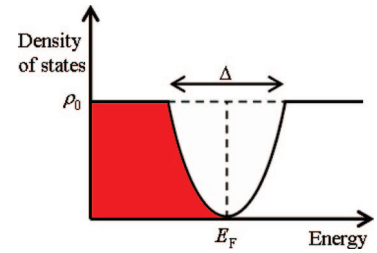

Figure 35. Density of states vs energy for a doped semiconductor exhibiting a soft Coulomb gap. The gap width is Δ.

The reduction of density of states near the Fermi level results in a "soft" Coulomb gap, since the density of states vanishes only at E_F (Figure 35). The width of the Coulomb gap (Δ) can be estimated by setting $\rho(\Delta) = \rho_0$, where ρ_0 is the density of states without taking into account the Coulomb interaction. A soft Coulomb gap has been observed in the density of states of boron-doped silicon below MIT using tunneling spectroscopy.[309]

We can use eq 68 and modify the Mott−VRH model to determine the temperature dependence of conductivity. Whereas in the Mott−VRH model, ΔN near the Fermi level is proportional to ΔW (eq 62), in the ES−VRH model, the presence of Coulomb interactions generates a corresponding ΔN given by

$$\Delta N = \int_0^{\Delta W} \rho(E)\, dE = \alpha\frac{(4\pi\varepsilon)^3}{e^6}\int_0^{\Delta W} E^2\, dE = \frac{\alpha}{3}\frac{(4\pi\varepsilon)^3}{e^6}\Delta W^3 \quad (69)$$

The average separation between sites r_{ij} (in 3D) is then equal to

$$r_{ij} = \left(\frac{3}{4\pi\Delta N}\right)^{1/3} = \left(\frac{9}{4\pi\alpha}\right)^{1/3}\frac{e^2}{4\pi\varepsilon\Delta W} \quad (70)$$

Following the above derivation for Mott−VRH using eq 70 rather than eq 63, we finally obtain

$$g \approx \exp\left[-\left(\frac{T_0^{\text{ES}}}{T}\right)^{1/2}\right] \quad (71)$$

where

$$T_0^{\text{ES}} = \beta\frac{e^2\kappa}{4\pi\varepsilon k_B} \quad (72)$$

and β is a numerical coefficient. Numerical calculations have yielded $\beta = 2.8$ for 3D systems.[310] The optimum hopping distance, r_{hop}, and hopping energy gap, ΔW_{hop}, are given by

$$r_{\text{hop}} = \frac{1}{4\kappa}\left(\frac{T_0^{\text{ES}}}{T}\right)^{1/2} \quad (73)$$

$$\Delta W_{\text{hop}} = \frac{k_B}{2}(T_0^{\text{ES}}T)^{1/2} \quad (74)$$

T_0^{ES} can be obtained from fitting the ES−VRH model to experimental data. Other parameters such as κ, r_{hop}, and ΔW_{hop} can then be calculated from T_0^{ES}.

For the ES−VRH model to hold, a number of conditions have to be satisfied.[311] (i) Since the model assumes that the probability of absorbing ΔW_{hop} is given by the Boltzmann distribution, $\Delta W_{\text{hop}} > k_B T$. This corresponds to $T_0^{\text{ES}} > 4T$. (ii) There is also an upper limit on acceptable values of

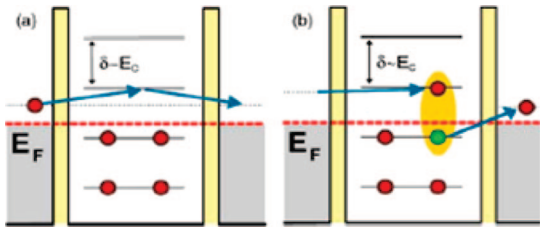

Figure 36. Schematic energy diagram for cotunneling processes: (a) elastic cotunneling, entering and exiting electrons have the same energy; (b) inelastic cotunneling, the entering and exiting electrons have different energies. During the inelastic cotunneling, an electron−hole excitation is generated in the grain. Reprinted with permission from ref 317 (Beloborodov's group). Copyright 2007 American Physical Society (http://dx.doi.org/10.1103/PhysRevB.75.052302).

ΔW_{hop}. The ES model only applies when hopping occurs between sites inside the soft Coulomb gap. In other words, ΔW_{hop} should be smaller than Δ. Outside of the Coulomb gap, the density of states is constant, and conductivity is described by the Mott's model. The critical temperature (T_C) for a transition from ES− to Mott−VRH is determined from the condition $\Delta W_{hop} = \Delta$ and is given by $T_C = 4\Delta^2/k_B{}^2T_0$. (iii) The hopping distance, r_{hop}, should be significantly larger than the distances between neighboring sites, s. As $r_{hop} \rightarrow s$, nearest-neighbor hopping dominates. The hopping distance is then fixed and activated Arrhenius behavior will be observed.

A number of studies of granular materials have observed $\nu = 1/2$. However, the applicability of the ES−VRH model to these systems has been debated in literature (for reviews, see refs 311, 312, and 313). In granular materials, the charging energies of grains can easily exceed k_BT under experimental conditions. Therefore, there is a "hard" Coulomb gap (or Hubbard energy gap) at the Fermi level,making the density of states at the Fermi level zero. The ES model, however, yields a soft gap.[310,314] Another problem is that fit parameters using the model usually yield physically unreasonable values. For example, the VRH model requires that the hopping distance be sufficiently large to allow the tunneling electrons to sample a reasonable number of grains located at various distances. Because of the rapid decay of wave functions in insulating media, tunneling over such large distances is not realistic. Several experimental studies on NP assemblies have reported hopping distances, r_{hop}, and localization lengths, $\xi = 1/\kappa$, that are as large as hundreds of nanometers, too large to be consistent with tunneling required by hopping.[133,164,166,185,296−298]

4.5.2. Cotunneling

To allow for a long-ranged hopping process in granular media, some recent studies have considered a possibility that charges may bypass the Coulomb blockade barrier via "cotunneling".[296,315−318] Cotunneling can be visualized as two concurrent events:[319] tunneling of an electron into a grain and the simultaneous escape of another electron from the same grain (Figure 36). There are two distinct cotunneling mechanisms: elastic and inelastic. Energies of entering and exiting electrons are the same in the former and different in the latter. Beloborodov et al.[318] have shown that the probability of elastic cotunneling can be expressed as $P_{elastic} \approx \exp(-2r/\xi_{elastic})$ where r is the hopping distance and $\xi_{elastic}$ is a localization length and is given by $\xi_{elastic} \approx 2L/\ln(E_C\pi/g\delta)$. Here L is the grain size, g is the intergrain conductance, and δ is the energy level spacing of the grain. Following the derivation for the ES model, they obtained a $\nu = 1/2$ T-dependence with $T_0 \approx e^2/\varepsilon k\xi_{elastic}$. They have found somewhat more complex expression for the probability of inelastic cotunneling. It, however, leads to a similar result, namely, $T_0 \approx e^2/\varepsilon k\xi_{inelastic}(T)$, with the localization length $\xi_{inelastic}(T)$ being weakly T-dependent: $\xi_{inelastic}(T) \approx 2L/\ln(E_C{}^2/16\pi gT^2)$. These mechanisms have yet to be explored experimentally.[296]

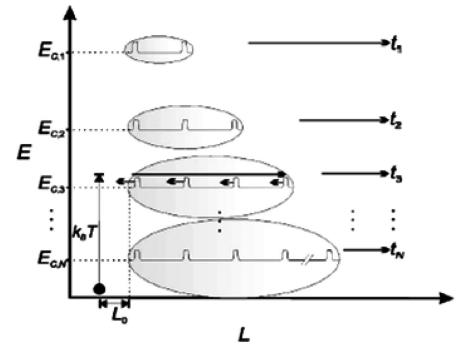

Figure 37. Illustration of a typical process in the QLH model. An electron can absorb energy $\sim k_BT$ and tunnel a distance L_0 to a neighboring cluster with charging energy $E_{C,3}$. As the electron traverses a quasi-1D path along the L coordinate, it has a transmission probability, Γ, at each scattering site. Both E_C and total transmission, $t_n = \Gamma^{nL}$, decrease with increasing cluster size. Reprinted with permission from ref 164 (Dhirani's group). Copyright 2005 American Physical Society (http://dx.doi.org/10.1103/PhysRevB.72.075441).

4.5.3. Quasi-Localized Hopping

Dunford et al.[164] observed $\nu = 1/2$ behavior near the percolation MIT in multilayer films of 1,4-butanedithiolate-linked Au NPs and proposed a different, so-called quasi-localized hopping (QLH) model to account for their observations. Hopping distances, r_{hop}, and localization lengths, $\xi = 1/\kappa$, obtained by fitting the ES model to data (taking $\varepsilon_r = 2.34$) were remarkably large, on the order of $\sim 10^2$ nm and $\sim 10^3$ nm, respectively. Empirically, r_{hop} and ξ seemed to correlate well with estimated sizes of clusters of linked NPs rather than tunneling distances. Also, r_{hop} and ξ exhibit an increasing trend as films approach the MIT. NP clusters also are expected to exhibit a growing trend as more NPs are added to the film, until, at the percolation threshold, the clusters form sample-spanning pathways. In contrast, in a model involving localized hopping sites, one would expect that hopping distances should decrease closer to MIT because of the increase of the density of sites.

Electrons in clusters are "quasilocalized"; that is, they must overcome a barrier to leave the cluster but are itinerant within the cluster. Dunford et al.[164] used a QLH model to derive a $\nu = 1/2$ law in analogy with the ES−VRH model. They proposed that charge flows by optimizing two competing mechanisms: one involving a cluster-charging energy barrier that scales as $\sim 1/L$, where L is the cluster size, and another involving conductance that drops exponentially with L. Cluster-charging energy is expected to be given by $E_C \approx e^2/4\pi\varepsilon L$. They considered electron scattering, likely arising from defects or NP surfaces within clusters, as a potential source of the exponential dependence on L (Figure 37). If the transmission probability at a scattering site is Γ (<1), and if there are n scattering sites per unit length, then the transmission probability through a cluster is $\Gamma^{nL} = \exp(-2L/$

ξ_{QLH}), where $\xi_{QLH} = 2/[n\ln(1/\Gamma)]$. Taking $g \approx \exp(-2L/\xi_{QLH} - e^2/4\pi\varepsilon L k_B T)$ and optimizing with respect to L generates a $\nu = 1/2$ T-dependence with $T_0 = 2e^2/\pi\varepsilon k_B \xi_{QLH}$. Dunford et al.[165] confirmed the importance of scattering from NP surfaces within clusters in a further study focusing on the magneto-conductance of these films.

4.5.4. NP Assemblies as Networks of Random Resistances

Another approach to explain observed $\nu = 1/2$ models NP films as networks of random resistances.[307,310,320−323] Each pair of NPs (i,j) is viewed as being equivalent to a resistance

$$R_{ij} = R_0 \, e^{2\kappa s_{ij}} \, e^{E_{ij}/k_B T} \quad (75)$$

where s_{ij} is the inter-NP separation and E_{ij} is an activation energy. Disorder-driven variations in s_{ij} and E_{ij} can cause large (orders of magnitude) variations in R_{ij}. The resistance of the resulting network can be estimated using a path of least resistance bridging the network. Such a path can be found by the following procedure.

Choose a value of resistance, R, and consider any two NPs as connected if $R_{ij} \leq R$. Otherwise, consider the NPs as disconnected, and set $R_{ij} \rightarrow \infty$. The fraction of connected NPs in the network is denoted by p. If R is very small, then only a small fraction of NPs are connected. So, as $R \rightarrow 0$, $p \rightarrow 0$. As R is increased, p increases. As $R \rightarrow \infty$, all NPs become connected and $p \rightarrow 1$. There is a critical resistance, R_c, for which the connected NPs form a continuous pathway of least resistance spanning the network. The resistance of this path can be approximated by the highest R_{ij}. The fraction of connected NPs at R_c corresponds to the percolation threshold of the network, p_c. The percolation threshold is a characteristic of the network and only depends on its geometry (e.g., dimensionality, coordination number). To find R_c, one needs to know the distribution of R_{ij} in the network. Denoting this distribution by $f(R_{ij})$, R_c can be determined from the equation

$$\int_0^{R_c} f(R_{ij}) \, dR_{ij} = p_c \quad (76)$$

Müller et al.[150,151] have shown that, by choosing square distribution functions for $2\kappa s_{ij} \equiv \lambda_{ij}$ and $E_{ij}/k_B T \equiv \varepsilon_{ij}$ (f_λ and f_ε, respectively), a $\nu = 1/2$ law can be obtained that fits experimental data. They chose

$$f_\lambda(\lambda_{ij}) = \begin{cases} \dfrac{1}{\Delta\lambda} & \text{for } \lambda_M - \dfrac{\Delta\lambda}{2} \leq \lambda_{ij} \leq \lambda_M + \dfrac{\Delta\lambda}{2} \\ 0 & \text{otherwise} \end{cases} \quad (77)$$

and

$$f_\varepsilon(\varepsilon_{ij}) = \begin{cases} \dfrac{1}{\Delta\varepsilon} & \text{for } \varepsilon_M - \dfrac{\Delta\varepsilon}{2} \leq \varepsilon_{ij} \leq \varepsilon_M + \dfrac{\Delta\varepsilon}{2} \\ 0 & \text{otherwise} \end{cases} \quad (78)$$

where $\lambda_M = 2\kappa s_M$ and $\varepsilon_M = E_M/k_B T$ are mean values, and $\Delta\lambda$ and $\Delta\varepsilon$ are widths of the f_λ and f_ε distributions, respectively. $f(R_{ij})$ is then obtained by

$$f(R_{ij}) = (1 - p_v)\int_0^\infty \int_0^\infty f_\lambda(\lambda_{ij}) f_\varepsilon(\varepsilon_{ij}) \delta\left(\lambda_{ij} + \varepsilon_{ij} - \ln\frac{R_{ij}}{R_0}\right) d\lambda_{ij} \, d\varepsilon_{ij} \quad (79)$$

where p_v is the fraction of voids. By solving eq 76 for R_c and assuming that the f_λ and f_ε are wide distributions, i.e., $\Delta E = 2E_M$ and $\Delta s = 2s_M$, they found $R_c \approx \exp[(T_0/T)^{1/2}]$, where $T_0 = 16 p_c \kappa s_M E_M/(1 - p_v)k_B$. For narrow distributions, they obtained an Arrhenius behavior: $R_c \approx \exp[2\kappa s_M + p_c E_M/(1 - p_v)k_B T]$. Figure 38 shows fits of the model to g vs $1/T$ data for films of 4 nm Au NPs cross-linked by 1,2-ethanedithiol or 1,8-octanedithiol. Films were prepared by filtering solutions of cross-linked NP aggregates through porous membranes.

5. Electrochemical Properties

In this section, we review studies involving electrochemical methods for exploring electron transport through NP assemblies. We describe quantized charging of NPs in solution and in solid phases as well as redox processes probed using NP-modified electrodes.

5.1. Quantized Charging of NPs in Solutions

5.1.1. Quantized Double-Layer Charging

Murray and co-workers[261,262] were the first to show that solutions of Au NPs can exhibit quantized electrochemical charging behavior. They used 0.1 mM solutions of highly monodisperse hexanethiolate-capped 1.6 nm Au NPs in 2:1 toluene/acetonitrile with 0.05 M tetrahexylammonium perchlorate. They studied electrochemical response of the NPs by cyclic voltammetry (CV) and differential pulsed voltammetry (DPV) using a Pt microelectrode and an Ag wire reference electrode. CV and DPV scans of NP solutions exhibited several (up to 10) regularly spaced current peaks at room temperature (Figure 39). Later, Quinn et al.[324] prepared solutions of 1.6 nm Au NPs with improved size dispersity and resolved 15 regularly spaced DPV peaks at room temperature (Figure 40, upper curve).

The peaks in the electrochemical data can be rationalized by quantized double-layer (QDL) charging of NPs in solution near the electrode surface.[82] Generally, application of a potential in the electrolyte solution is accompanied by formation of an ionic double layer.[77,325−327] Given that NPs

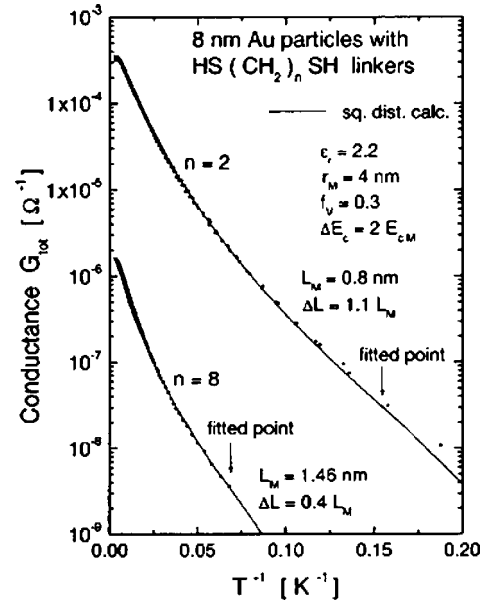

Figure 38. Calculated and measured values of conductance versus $1/T$ for two films of 4 nm Au NPs cross-linked by 1,2-ethanedithiol or 1,8-octanedithiol. Reprinted with permission from ref 150 (Müller's group). Copyright 2002 American Physical Society (http://dx.doi.org/10.1103/PhysRevB.66.075417).

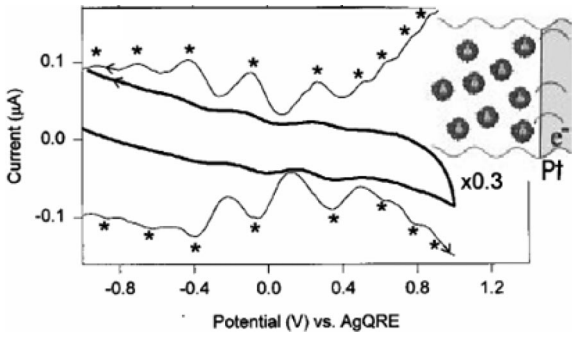

Figure 39. CV (thick line, 100 mV/s) and DPV (thin line, 20 mV/s, 25 mV pulse) obtained using 0.1 mM hexanethiolate-capped 1.6 nm Au NPs in 2:1 toluene/acetonitrile/0.05 M Hx_4NClO_4 at 298 K. A 7.9×10^{-3} cm^2 Pt electrode and Ag wire quasi-reference electrode were used. Current peaks are indicated by *, and top and bottom curves are negative and positive scans, respectively. Reprinted with permission from ref 261 (Murray's group). Copyright 1997 American Chemical Society (http://dx.doi.org/10.1021/ja972319y).

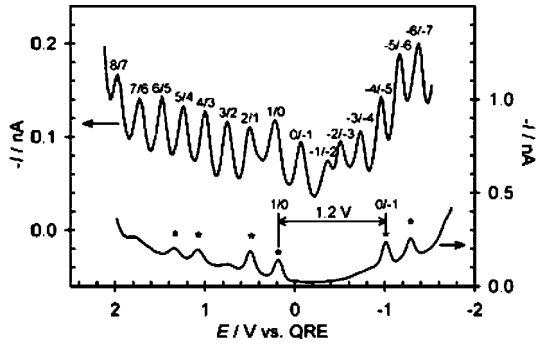

Figure 40. DPV scans of NP solutions measured using a Pt microelectrode. The upper curve, obtained using hexanethiolate-capped 1.6 nm Au NPs, exhibits 15 QDL peaks; and the lower, obtained using hexanethiolate-capped 1.1 nm Au NPs, exhibits a HOMO−LUMO gap. Reprinted with permission from ref 324 (Quinn's group). Copyright 2003 American Chemical Society (http://dx.doi.org/10.1021/ja0349305).

possess a capacitance, C, NP charging occurs at potential intervals, $\Delta V = e/C$. If C is sufficiently small, then the charging energy exceeds k_BT, and single electron charging can be observed. Observation of QDL charging also requires that the NPs be fairly monodisperse in terms of both size and composition since polydispersity gives rise to a range of NP capacitances that smears out QDL charging peaks.[328]

Chen et al.[329] have developed a theoretical model to explain QDL charging. In their model, the potential of an NP with charge state z in solution is expressed by

$$E_{NP^z} = E_{PZC} + \frac{ze}{C} \tag{80}$$

where E_{PZC} is the potential of zero charge of the NP (i.e., $z = 0$). They argued that a mixture of NPs with charges z and $z - 1$ can be regarded as a "redox couple" with a formal potential:

$$E^\circ_{z,z-1} = E_{PZC} + \frac{(z - 1/2)e}{C} \tag{81}$$

The basis of this analogy is that NPs can be viewed as multivalent redox species that exhibit equally spaced formal potentials,

$$\Delta E^\circ = \frac{e}{C} \tag{82}$$

assuming that C is independent of the NP charge state, z.[70] Continuing the analogy with redox molecular species, the potential of an NP redox couple follows the Nernst equation,

$$E = E^\circ_{z,z-1} + \frac{RT}{F} \ln \frac{[NP^z]}{[NP^{z-1}]} \tag{83}$$

where $[NP^z]$ and $[NP^{z-1}]$, respectively, represent concentrations of reduced and oxidized states of the NP charge state couple, and R and F are the gas constant and Faraday constant, respectively.

Murray and co-workers[123,330] have exploited the Nernstian behavior of the NPs to control the charge states of NPs in a solution by applying an electrochemical potential to the solution or by employing chemical redox reactions. Pietron et al.[330] have shown that solutions of hexanethiolate-capped 1.6 nm Au NPs in a toluene/acetonitrile solvent containing a supporting electrolyte can be electrochemically charged to controllable potentials. For example, using a Pt mesh electrode and an Ag/AgCl reference electrode, they applied a potential of 0.91 V to a stirred solution of NPs for a few hours. Then, after transferring the solution to a separate cell, they measured the potential of the solution and observed a potential of 0.69 V corresponding to a charge state of $z = +3.6$ e/NP. The NP charge state was tunable by controlling the applied potential. Resulting charged NPs were stable in solution for hours, could be isolated in dried form, and retained most of their charge upon redissolution. In another study, Wuelfing et al.[123] prepared solutions of charged NPs using a chemical redox reaction. They used CH_2Cl_2 solutions of hexanethiolate-capped 1.6 nm Au NPs, mixed them with an aqueous solution containing an oxidant $Ce(SO_4)_2$ for various periods of times, and then separated the reaction phases. The reaction time determined the potential of the resulting NP solutions. Again, the charged NPs retained most of their charge upon isolation and redissolution.

Although most studies of electrochemically charged NPs have involved the use of Au NPs, QDL charging has also been observed using NPs made of other metals such as Ag,[331] Pd,[332,333] Cu,[334] and Rh.[335] Reports of QDL using semiconducting NPs (i.e., QDs) remain scarce. Ding et al.[336] have observed QDL charging using ~1.74, ~2.77, and ~2.96 nm Si QDs in N,N'-dimethylformamide and acetonitrile. Observation of QDL charging in solutions of QDs is challenging since they are typically chemically unstable upon electron transfer. For example, charge transfer in PbS[337] or CdS[338] QDs leads to multiple electron-transfer reactions and chemical decomposition.[339]

A number of studies have investigated influences of capping ligands (e.g., ligand thickness[340] or chemical structure[341]), solvent/electrolyte,[342] and temperature[343] on QDL charging of NPs. Hicks et al.[340] have used $CH_3(CH_2)_{n-1}S$-capped Au NPs to study the dependence of capacitance on monolayer thickness ($n = 4-16$). Their results (see Table 3) show that the NP capacitance can be modeled as the capacitance of two concentric conducting spheres separated by a dielectric (alkanethiolate monolayer) of thickness s and dielectric constant ε_r (see Figure 20b):

$$C = 4\pi\varepsilon_0\varepsilon_r \frac{R(R+s)}{s} \tag{84}$$

There are a number of approximations in this simple model,[344] including that the length of fully extended ligand

Table 3. NP Capacitance, *C*, As a Function of Monolayer Chain Length (Reprinted with Permission from Ref 340 (Murray's Group); Copyright 1999 American Chemical Society (http://dx.doi.org/10.1021/ac990432w))

chain length (R, s, nm)[a]	C^{calc}, aF[b]	C^{expt}, aF[a]	ratio (C^{expt}/C^{calc})
In 2:1 Toluene/CH_3CN			
C_4S (0.8, 0.52)	0.69	0.59	0.9
C_6S (0.8, 0.77)	0.53	0.57	1.1
C_6S (1.0, 0.77)	0.77	0.72	1.1
C_8S (0.7, 1.02)	0.40	0.52	1.3
$C_{10}S$ (0.8, 1.27)	0.44	0.47	1.1
$C_{12}S$ (0.8, 1.52)	0.39	0.40	1.0
$C_{16}S$ (0.8, 2.52)	0.36	0.39	1.1
	In CH_2Cl_2		
C_6S (0.8, 0.77)	0.53	0.57	1.1
C_6S (1.0, 0.77)	0.77	0.70	1.1
C_8S (0.7, 1.02)	0.40	0.55	1.4
$C_{10}S$ (0.8, 1.27)	0.44	0.53	1.2

[a] For details, see ref 340. [b] Calculated from eq 84.

chains determines the thickness, s, and that the electrolyte solution is a good conductor. Guo et al.[341] have studied effects of substituents, "X", on capping ligands. They measured formal potentials of 1.1 nm Au NPs capped with arylthiolates (p-$HSCH_2CH_2C_6H_4X$) and found that, as the electron affinity of X was changed from electron-donating (OCH_3) to electron-withdrawing (NO_2), the formal potentials of NPs shifted to more positive values by as much as 450 mV. The substituents have a similar effect on redox potentials of molecular species.

5.1.2. Molecule-Like Charging

In addition to QDL charging that arises from the small capacitances of NPs, sufficiently small NPs can also exhibit molecule-like charging due to discrete electronic energy levels. Figure 40 (lower curve) shows DPV scan of 1.1 nm Au NPs[324,345,346] exhibiting a large gap between the first oxidation and reduction peaks around E_{ZPC}. The size of the gap, as shown by Chen et al.,[262] increases as NP size decreases and is detectable for NPs smaller than ~1.5 nm. This central gap is, therefore, attributed to an energy difference between the highest occupied (HOMOs) and lowest unoccupied (LUMOs) molecular orbitals of small NPs and highlights their large energy level spacings.

To investigate the origin of the gap, Murray and co-workers[345] studied electrochemical and optical properties of phenylethylthiolate-capped 1.1 nm Au NPs in CH_2Cl_2 (initially the authors assigned the NPs as $Au_{38}(S(CH_2)_2Ph)_{24}$, later revised to $Au_{25}(S(CH_2)_2Ph)_{18}$).[347] Figure 41a shows a DPV scan of the NPs obtained at room temperature. The scan exhibits a central gap of $\Delta E^{o}_{ox1-red1} \approx 1.62$ V and a spacing between the first and second oxidation peaks of $\Delta E^{o}_{ox2-ox1} \approx 0.29$ V. The central energy gap is given by the HOMO−LUMO energy gap plus the energy required to charge the NP. Estimating the NP charging energy using $\Delta E^{o}_{ox2-ox1}$, one obtains a HOMO−LUMO energy gap of $e\Delta E^{o}_{ox1-red1} - e\Delta E^{o}_{ox2-ox1} \approx 1.33$ eV. The HOMO−LUMO gap can be independently determined by optical absorbance spectroscopy. UV/vis spectra of the NPs (see Figure 41b) exhibit an absorbance edge corresponding to a HOMO−LUMO gap of 1.33 eV, in excellent agreement with the preceding estimate. On the basis of their observations, they proposed an energy level structure for the phenylethylthiolate-capped 1.1 nm Au NPs.[345]

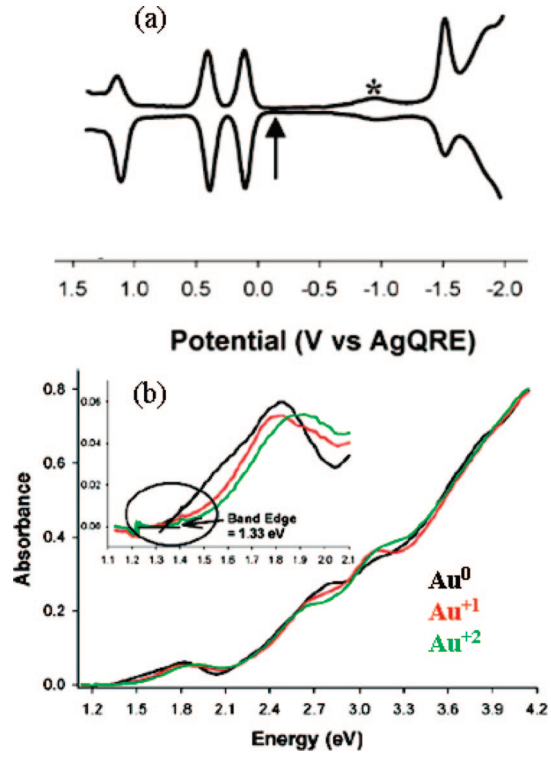

Figure 41. (a) DPV scan (at 0.02 V/s) of phenylethylthiolate-capped 1.1 nm Au NPs. Spectra were obtained using 0.1 M Bu_4NPF_6 and degassed CH_2Cl_2 at 25 °C. A 0.4-mm-diameter Pt working, Ag wire quasi-reference and Pt wire counterelectrode were used. An arrow indicates the solution rest potential, and * indicates a feature due to remnant O_2. (b) UV/vis spectra of Au^0 (black line), Au^{1+} (red line), and Au^{2+} (green line) NPs in degassed CH_2Cl_2 solution at 25 °C. The three spectra are of the same solution; the 1+ and 2+ charge states were generated by electrolysis in a spectroelectrochemical cell. Reprinted with permission from ref 345 (Murray's group). Copyright 2004 American Chemical Society (http://dx.doi.org/10.1021/ja049605b).

5.2. Quantized Charging in NP Assemblies on Solid Substrates

Quantized electrochemical charging can also be observed in immobilized mono-[348−355] or multilayer[168,170,356−359] assemblies of NPs on solid substrates. Chen[349] measured CV and DPV scans of a gold electrode modified with a self-assembled monolayer of 1.6 nm Au NPs (Figure 42). The author prepared films by exposing hexanethiolate-capped NPs to 1,6-hexanedithiol, partially displacing the original capping groups. The NPs were subsequently anchored to the electrode surface via the hexanedithiol linkers. CV and DPV curves (Figure 42 parts a and b) exhibited regularly spaced current peaks similar to those exhibited by NPs in solution. Figure 42c shows a plot of NP formal potentials, obtained from DPV data, versus NP charge states (z), confirming a linear dependence (see eq 81). From the slope and the intercept, one can estimate the NP capacitance ($C = 0.75$ aF) and the potential of zero charge ($E_{PZC} = -0.22$ V). These estimates are in good agreement with those for NPs in solution: $C = 0.59$ aF and $E_{PZC} = -0.2$ V.[348] NP monolayers usually exhibit smaller voltammogram peaks than NPs in solutions, because fewer NPs are electrochemically charged in a monolayer than than in solution.[348] Yang et al.[354] have prepared Langmuir monolayers of hexanethiolate-capped 2 nm Au NPs and studied their voltammetric responses at an air−water interface using butanethiolate-coated IDA electrodes. They observed current peaks with a spacing of ~150

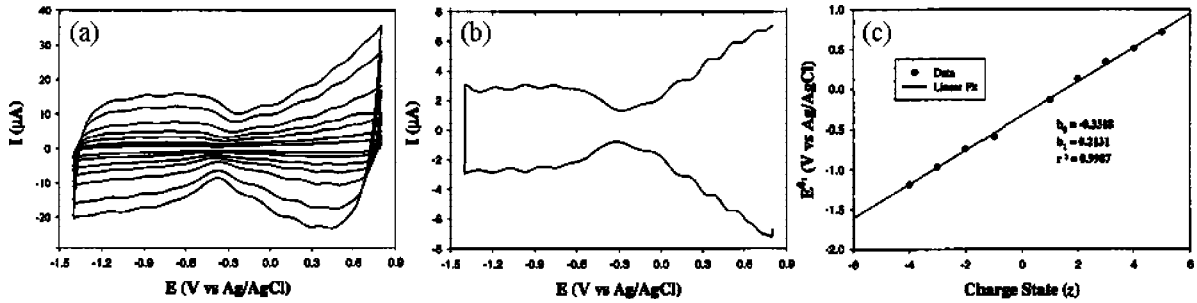

Figure 42. (a) CV and (b) DPV scans of a monolayer of hexanethiolate-capped Au NPs self-assembled on a Au electrode surface. The modified electrode was immersed in CH_2Cl_2 containing 0.1 M tetra-*n*-butylammonium perchlorate. CV scans were measured at sweep rates of 100, 200, 400, 600, 902, 1505, and 2000 mV/s. During DPV, the DC potential sweep rate was 10 mV/s and the pulse amplitude 50 mV. (c) Plot of formal potentials vs NP charge state. Data were obtained from DPV measurements. Reprinted with permission from ref 349 (Chen's group). Copyright 2000 American Chemical Society (http://dx.doi.org/10.1021/jp993524y).

mV in a potential range between −0.7 and +0.7 V. In solution, the NPs exhibited a peak spacing of ∼270 mV. Yang et al. attributed the smaller peak spacing exhibited by monolayers to an increase in NP capacitances generated by ligand intercalation and NP coupling.

Murray and co-workers[168,170,358] studied the QDL charging of multilayer NP films. The films comprised multilayers of 1.6 nm Au NPs self-assembled via carboxylate−ion−carboxylate linkages (see Figure 6) onto gold substrates. When used as electrodes in a CH_2Cl_2 solution containing a supporting electrolyte, the multilayers exhibited CV and DPV responses with QDL peaks. Figure 43 shows cyclic voltammograms of multilayer films with varying thicknesses.[170] The peak currents increase with the number of the NPs that can be electrochemically charged on the surface. QDL charging requires that electrolyte ions move toward or away from the NPs to balance the charge on the NP and maintain local electroneutrality within the film. Observation of QDL events thus implies that charge and ion-transfer processes are feasible through these films.[357] Chen and co-workers[350,351,353,356,359] have studied the influence of electrolyte ions on QDL charging of immobilized NPs on electrode surfaces in aqueous media. They have found that the QDL charging could be rectified by certain hydrophobic ions (e.g., PF_6^-, ClO_4^-, BF_4^-). That is, when $E > E_{PZC}$, currents exhibited a series of voltammetric peaks, but when $E < E_{PZC}$, the currents were suppressed (Figure 44). They attributed this rectificating behavior to binding of hydrophobic anions to positively charged NPs at $E > E_{PZC}$. For $E < E_{PZC}$, such ion binding is not favored, and only featureless charging of the electrode double layer is observed.

QDL charging offers a means to obtain electron transfer (ET) rates in NP assemblies using common electrochemical methods. ET-limited currents in such measurements are proportional to electron diffusion coefficients, D_E, in the NP assemblies, which in turn are related to electron hopping rates between NPs, k_{HOP}. Using a cubic lattice model and assuming only nearest-neighbor hopping (NNH), $D_E = k_{HOP}\delta^2/6$ where δ is the NP center−center core separation and represents an effective electron hopping length.[170] Using films of 1.6 nm Au NPs tethered via carboxylate−Zn^{2+}−carboxylate linkage and potential step chronoamperometry, Hicks et al.[170] found $k_{HOP} \approx 10^6\ s^{-1}$. They also found no significant variation of k_{HOP} with NP charge state or film coverage. This k_{HOP} is comparable with ET rates between Au electrodes and ferrocene units with intervening alkane chains; for example, the rate constant is $\sim 10^6\ s^{-1}$ using a five-methylene chain.[239] Kim and Lee[355] have studied ET rates through Langmuir monolayers of 1.1 nm Au NPs linked with $HS(CH_2)_nSH$ (n = 5, 6, 8, 9). They observed that k_{HOP} decreased exponentially (from 5.0×10^5 to $2.2 \times 10^4\ s^{-1}$) with increasing inter-NP distance (from 9.5 to 13.3 Å) with a decay constant of 0.82 $Å^{-1}$. The value of the decay constant is consistent with an underlying tunneling mechanism for electron transport through NP films.

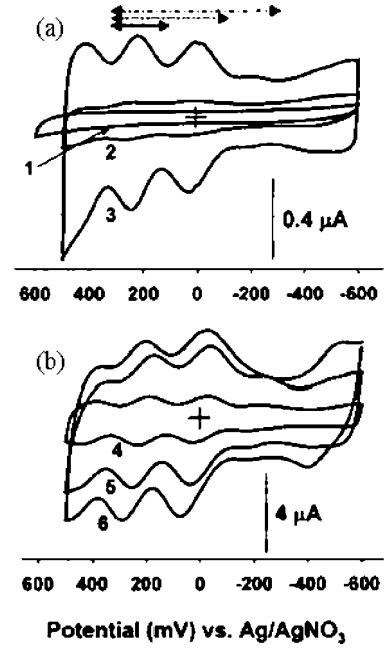

Figure 43. CV scans obtained using electrodes modified with (a) a mercaptoundecanoic acid monolayer (1) and subsequently exposed to an NP solution once yielding a ∼single monolayer film with a coverage of 3×10^{-11} mol/cm^2 (2), twice yielding an ∼8-monolayer-thick film with a coverage of 1.6×10^{-10} mol/cm^2 (3), (b) three times yielding an ∼16-monolayer-thick film with a coverage of 3.1×10^{-10} mol/cm^2 (4), four times yielding an ∼31-monolayer-thick film with a coverage of 6.2×10^{-10} mol/cm^2 (5), and five times yielding an ∼55-monolayer-thick film with a coverage of 1.1×10^{-9} mol/cm^2 (6). Carboxylate−ion−carboxylate linkages facilitated NP self-assembly onto the surfaces. Coverage was estimated using the charge under the 2+/1+ peak, above the continuum background. Arrows indicate one, two, and three electron charging events with respect to the NP^{2+} charge state. Scans were obtained using 50 mV/s scan rate, 0.1 M Bu_4NPF_6 electrolyte in CH_2Cl_2, $Ag/AgNO_3$ reference, 0.02 cm^2 working electrode, and a Pt counter electrode. Reprinted with permission from ref 170 (Murray's group). Copyright 2001 American Chemical Society (http://dx.doi.org/10.1021/ja0106826).

QDL charging has enabled studies of the role of NP charge state on electron transport through NP assemblies. Films of NPs with mixed charge states (or *mixed-valent* NPs) can be

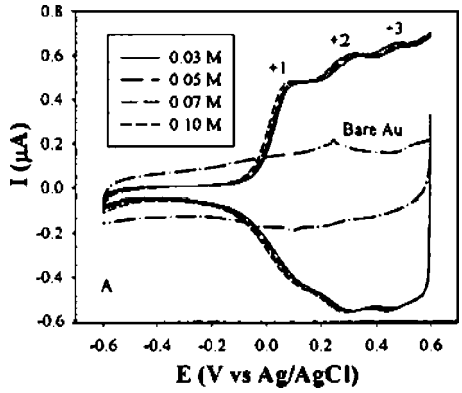

Figure 44. CV scans obtained using a Au electrode modified with a monolayer of hexanethiolate-capped 2 nm Au NPs. The electrode was immersed in aqueous NH_4PF_6 solutions of various concentrations. Also shown is a CV of the same bare electrode in 0.1 M NH_4PF_6. Electrode area is 1.1 mm^2. Sweep rate is 100 mV/s. Reprinted with permission from ref 350 (Chen's group). Copyright 2000 American Chemical Society (http://dx.doi.org/10.1021/ja0016093).

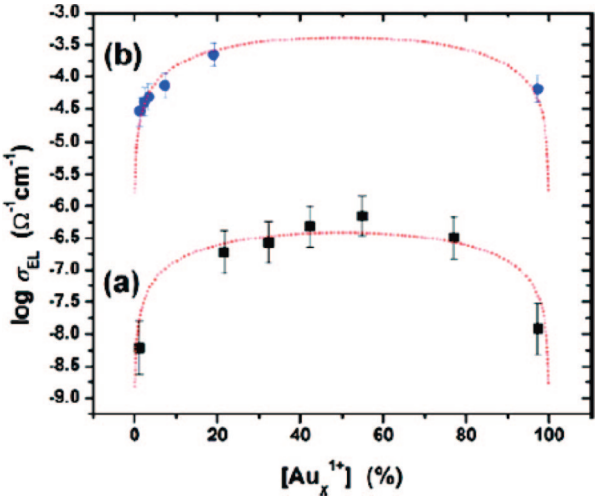

Figure 45. Effect of the NP charge state composition on film conductivities: (a) mixed-valent hexanethiolate-capped 1.1 nm Au NPs; (b) mixed-valent phenylethylthiolate-capped 1.6 nm Au NPs. Estimated error bars are ±10%. Red dotted curves are conductivity values simulated using a bimolecular reaction with rate constants 1.5×10^6 M^{-1} s^{-1} for 1.1 nm and 4.3×10^9 M^{-1} s^{-1} for 1.6 nm NPs. Reprinted with permission from ref 360 (Murray's group). Copyright 2006 American Chemical Society (http://dx.doi.org/10.1021/ja062736n).

regarded as electron- or hole-doped NP assemblies and can be prepared as described in section 5.1.1. Studies of mixed-valent NP films[123,360,361] have shown that film conductivities depend on the NP charge state composition. Figure 45 displays conductivities of monolayer-capped Au NP films with various fractions of NP^0 and NP^{1+}. Films were prepared using either phenylethylthiolate-capped 1.1 nm NPs or hexanethiolate-capped 1.6 nm NPs. Film conductivities exhibit minima when they were composed of mostly NP^0 or NP^{1+}, and maxima at 1:1 composition of NP^0/NP^{1+}. Murray and co-workers[123,360] have proposed a bimolecular rate law to describe the conductivities of such mixed-valent NP films,

$$NP^0 + NP^{1+} \xrightarrow{k_{EX}} NP^{1+} + NP^0 \qquad (85)$$

where k_{EX} is the rate constant for the bimolecular exchange reaction ($M^{-1}s^{-1}$). The rate of the exchange reaction is proportional to $[NP^0][NP^{1+}]$ and is the largest when the concentrations are equal (i.e., 1:1 mixed-valency). They have calculated k_{EX} from film conductivities, σ, assuming a cubic lattice model of film structure:

$$k_{EX} = \frac{6RT\sigma}{10^{-3}F^2\delta^2[NP^0][NP^{1+}]} \qquad (86)$$

k_{EX} for films of mixed-valent hexanethiolate-capped 1.6 nm and phenylethylthiolate-capped 1.1 nm Au NPs were, respectively, $\sim 3 \times 10^9$ and $\sim 2 \times 10^6$ $M^{-1}s^{-1}$, and corresponding activation energies were ~70 and ~210 meV, respectively. The ET rate between hexanethiolate-capped 1.6 nm $Au^{1+/0}$ NPs was ~3 orders of magnitude larger than that between phenylethylthiolate-capped 1.1 nm $Au^{1+/0}$ NPs. The difference could be attributed to differences in activation energies, NP ligand shell (thickness, molecular structure), and NP density of states.

5.3. NP-Modified Electrodes for Probing Redox Activity

Understanding structure−properties relationships of NP-modified electrodes is a key step in their effective application in electrochemistry. Electrochemical processes at the electrode/solution interface involve movement of ions from the solution to the interface and transfer of electrons from redox-active centers to the electrode. Important considerations are how kinetics of these processes, electrochemical activity, and sensitivity vary with assembly components and architecture. Studies using microarray electrodes[362] have shown that electrochemical properties of electrodes depend on the fraction of active electrode area. Therefore, NP-modified electrodes are expected to exhibit electrochemical responses (e.g., peak height, width, or separation in cyclic voltammograms) that depend on NP size, interparticle spacing, and packing density.[363] Molecular components of NP assemblies can introduce barriers for electron tunneling through NP−NP or NP−electrode junctions and influence the rate of ET. Assembly architecture is also critical: a degree of randomness inherent in assembly process leads to defects, disorder, and percolation effects that can strongly influence electrochemical activity.

Studies exploring electrochemical characteristics of NP-modified electrodes have typically adopted two approaches to prepare the electrodes: (i) constructing NP assemblies comprising electro-*inactive* monolayers on the electrode to probe redox-active species in solution phase and (ii) incorporating the redox-active units in the molecular components of the NP assemblies. Next, we review the results achieved using these approaches.

5.3.1. Electrodes Modified with Redox-Inactive NP Assemblies

Figure 46, reported by Zhong et al.,[364] shows CV curves obtained using a bare Au electrode (curve a), a 1,9-nonanedithiol SAM-coated Au electrode (curve b), and a 1,9-nonanedithiol/NP modified Au electrode (curves c and d). All measurements were performed with the electrodes immersed in a 1 mM $Fe(CN)_6^{4-}$/1 M KCl electrolyte. The CV curve of the bare gold electrode exhibits reversible peaks corresponding to oxidation and reduction of the $Fe(CN)_6^{4-/3-}$ redox couple. The CV response of the SAM-coated electrode is significantly suppressed. CV scans of a 1,9-nonanedithiol-coated Au electrode immersed in a solution

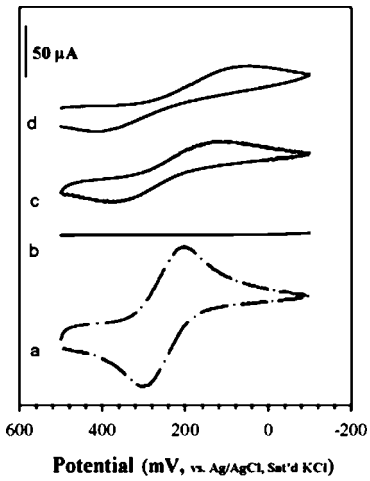

Figure 46. CV scans of $Fe(CN)_6^{4-/3-}$ redox probe at (a) a bare gold electrode, (b) a 1,9-nonanedithiol SAM-coated electrode, and a 1,9-nonanedithiol SAM-coated electrode immersed in a solution of decanethiolate-capped 5 nm Au NP for (c) 10 and (d) 24 h. Electrode substrate = Au/glass; geometric area = 0.34 cm^2; electrolyte = 1 mM $Fe(CN)_6^{4-/3-}$/1 M KCl; and scan rate = 50 mV/s. Reprinted with permission from ref 364 (Zhong's group). Copyright 1999 Elsevier (http://dx.doi.org/10.1016/S1388-2481(99)00008-9).

of decanethiolate-capped 5 nm Au NPs for 10 (curve c) and 20 h (curve d) exhibit partially restored electrochemical activity.

A SAM-coated electrode can mediate redox reactions in two ways:[365] (i) redox can occur at the SAM/solution interface with electron transfer through the SAM and (ii) the electroactive species can penetrate through defects or pinholes in the SAM and redox can occur at the electrode surface. Studies of alkanethiolate SAMs on gold electrodes have shown that long carbon chain alkanethiols ($n \geq 6$) produce excellent SAMs with effective barriers for ET and ion penetration. On the other hand, electrodes coated with shorter-chain alkanethiolates exhibit partially blocked responses that can be attributed to a combination of defects and small ET barriers.[365] Several studies have observed restorated electrode activity after depositing NPs on alkanedithiols.[22,94,152,155,363,364,366−374] This indicates that redox can occur at NP surfaces and that NPs can act as "electron relays" between the electrolyte solution and the underlying electrode.[366] The NP-modified electrodes (Figure 46, curves c and d) exhibit a larger separation of oxidation and reduction waves, ΔE_p, than bare electrodes. ΔE_p provides a measure of reversibility of the redox reaction at the electrode/solution interface. Reversibility requires that heterogeneous ET between redox species and the electrode be sufficiently fast to allow the redox species to equilibrate during the scan time. Hence, reversibility depends on the relative values of the heterogeneous ET rate and the scan rate, v.[375,376] For a reversible redox reaction, $\Delta E_p = 59/n$ mV, where n is the number of electrons involved in the reaction.[375] If kinetics of heterogeneous ET is slow, then the process is said to be *quasi-reversible*. In this case, $\Delta E_p > 59/n$ mV and increases with v.[375] The large ΔE_p observed in Figure 46 indicates quasi-reversible ET.

Addition of more NPs to the NP-modified electrode leads to additional improvement in electrochemical response of the electrode and increased reversibility.[155,363,368−370] Lu et al.[370] have studied CV responses of Au electrodes modified with multilayer films of 12 nm Au NP linked by 1,6-hexanedithiolate. Figure 47 shows CV scans of the NP-modified electrodes with various numbers of NP layers (1, 3, 5, and 7) in 5 mM $Fe(CN)_6^{3-}$/0.1 M Na_2SO_4 at $v = 50$ mV/s. As the number of layers increases, redox peak currents increase and ΔE_p decreases from 250 mV to 75 mV. These results can be explained by viewing the NP film as an array of "nanoelectrodes". The active area of the nanoelectrode array is determined by the number (or loading density) of the NPs due to the porous nature of such films. Increasing nanoelectrode loading gives rise to a larger electrode area and results in higher redox peak currents.[92,94,363,369,370,377]

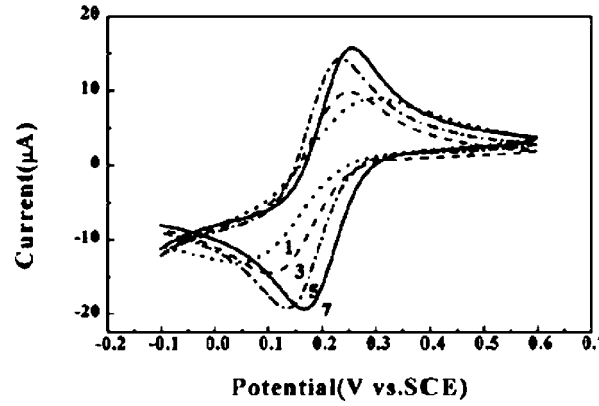

Figure 47. CV scans of 12 nm Au NP modified electrodes in 5 mM $Fe(CN)_6^{3-}$/0.1 M Na_2SO_4 obtained at a scan rate of 50 mV/s. Numbers of Au NP layers are indicated on graph. Reprinted with permission from ref 370 (Li's group). Copyright 2002 Elsevier (http://dx.doi.org/10.1006/jcis.2002.8238).

The ability of NPs to modify an electrode's redox activity through surface area has been corroborated by a number of studies that have investigated the influence of NP size on electrochemical response.[363,368,378−380] These studies involve enlarging NPs already bound to a substrate. For example, Musick et al.[368] have prepared an Au NP film by immersing an aminosilane-funtionalized glass substrate into an aqueous solution of 12 nm Au NPs. To increase the size of the surface-bound NPs, they immersed the film into an aqueous solution of 0.4 mM NH_2OH and added a 1% solution of $HAuCl_4$. AFM images of the resulting film showed an increase in NP size and a decrease in inter-NP separation as a function of immersion time. Figure 48 shows CV using $Ru(NH_3)_6^{3+}$ and the NP-modified electrode after immersion in the Au^{3+}/NH_2OH solution for various times (7.5−20 min). As the immersion time increased, peak currents increased 5-fold, and ΔE_p decreased from 150 to <90 mV. An inset in Figure 48 shows that current peaks are proportional to $v^{1/2}$, which is expected for a planar electrode and linear ion diffusion characteristics.[375] These results demonstrate an ability of NPs to fine-tune electrochemical properties of nanoelectrode arrays.

To gain further insight into kinetics of ET and ion diffusion at the interface of NP-modified electrodes, several groups have exploited electrochemical impedance spectroscopy (EIS).[92−94,363,370,377,380] In EIS, a small AC potential is applied to an electrochemical cell: $V = V_0\, e^{i\omega t}$, where V_0 is the modulation amplitude, $i = \sqrt{-1}$, ω is the modulation frequency, and t is time. The resulting modulated current through the cell, $I = I_0\, e^{i(\omega t+\phi)}$, and its phase angle, ϕ, are measured as a function of ω. The ratio V/I is the complex impedance $Z = |Z|\, e^{i\phi}$, where $|Z| = V_0/I_0$. For example, for a circuit composed of a resistance (R) and a capacitance (C) in series, one can show that $Z = R - i/\omega C$, $\tan(\phi) = -1/$

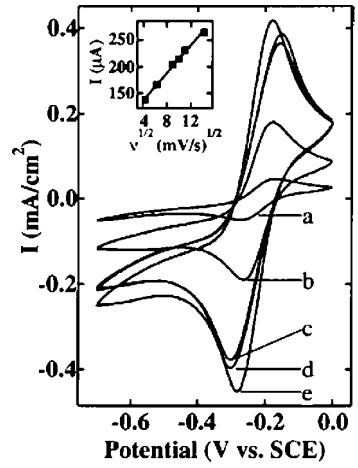

Figure 48. CV scans of a Au NP-modified electrode prepared by immersing the electrode into a 0.4 mM NH_2OH/0.01% Au^{3+} mixture for (a) 7.5, (b) 10, (c) 12.5, (d) 17.5, and (e) 20 min. Scans were obtained with electrodes immersed in 5 mM $Ru(NH_3)_6^{3+}$ in 0.1 M Na_2SO_4 at $\upsilon = 50$ mV/s. Inset shows the peak current vs $\upsilon^{1/2}$ for the electrode immersed in the NH_2OH/Au^{3+} mixture for 7.5 min. Reprinted with permission from ref 368 (Natan's group). Copyright 1999 American Chemical Society (http://dx.doi.org/10.1021/la980911a).

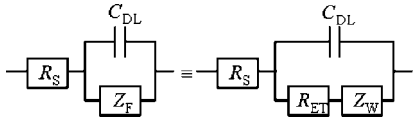

Figure 49. Equivalent circuit for an electrochemical cell: R_S, solution resistance; C_{DL}, double-layer capacitance; Z_F, Faradaic impedance; R_{ET}, ET resistance; and Z_W, Warburg impedance. Reprinted with permission from ref 375. Copyright 1980 John Wiley & Sons, Inc.

ωRC, and $|Z| = [R^2 + 1/(\omega C)^2]^{1/2}$. Figure 49 shows a simple circuit that can be used to model an electrochemical cell. The circuit consists of an electrolyte solution resistance, R_S, in series with a parallel combination of a double-layer capacitor, C_{DL}, and a Faradaic impedance, Z_F. Z_F in turn consists of two components: an ET resistance, R_{ET}, and a mass-transfer impedance (known as Warburg impedance, Z_W) resulting from the diffusion of ions from the bulk electrolyte to the electrode interface. Z_W varies with frequency as $\omega^{-1/2}$,

$$Z_W = \sigma_W \omega^{-1/2} - i\sigma_W \omega^{-1/2} \tag{87}$$

where σ_W is Warburg's coefficient and depends on diffusion coefficients of redox species in the electrolye.[375] R_S and Z_W represent properties of the bulk electrolyte solution and are not significantly affected by chemical modifications of the electrode. C_{DL} and R_{ET}, on the other hand, depend on the dielectric and kinetics characteristics at the electrode/electrolyte interface and are influenced by such modifications.

Figure 50 shows an EIS curve of the circuit in Figure 49, presented as a Nyquist plot showing real, Z_{Re}, versus imaginary, Z_{Im}, components of Z. The plot exhibits a semicircle at high ω and a straight line at low ω. The semicircle reflects an ET-controlled process, shown as follows. At very high frequencies ($\omega \rightarrow \infty$), Z_W becomes negligible compared with R_{ET}, and the impedance of the circuit is given by

$$Z = R_S + \frac{1}{(R_{ET})^{-1} + i\omega C_{DL}} \tag{88}$$

The real and imaginary components of Z are then

$$Z_{Re} = R_S + \frac{R_{ET}}{1 + (\omega C_{DL} R_{ET})^2} \tag{89}$$

$$Z_{Im} = -\frac{\omega C_{DL} R_{ET}^2}{1 + (\omega C_{DL} R_{ET})^2} \tag{90}$$

Elimination of ω from eqs 89 and 90 yields

$$\left(Z_{Re} - R_S - \frac{R_{ET}}{2}\right)^2 + Z_{Im}^2 = \left(\frac{R_{ET}}{2}\right)^2 \tag{91}$$

A plot of Z_{Re} vs Z_{Im} is a circle centered at $Z_{Re} = R_S + R_{ET}/2$ and $Z_{Im} = 0$. At very low frequencies ($\omega \rightarrow 0$), the Warburg impedance dominates and one can show that (see ref 375)

$$Z_{Im} = Z_{Re} - R_S - R_{ET} + 2\sigma_W^2 C_{DL} \tag{92}$$

Thus, the linear region in the Nyquist plot corresponds to an ion-diffusion-controlled process. Parameters such as R_{ET}, C_{DL}, and R_S relating to ET and ion-diffusion characteristics at the electrode/solution interfaces can be extracted from the Nyquist plot as shown in Figure 50.

Cheng et al.[363] studied effects of NP size and loading density on EIS responses of Au NP-modified electrodes. Figure 51a shows Nyquist plots of a mercaptosilane-functionalized ITO electrode after immersion in a 12 nm Au NP solution for various times. As immersion time and, therefore, NP loading density increase, the radii of the semicircle regions decrease. Corresponding R_{ET} values decrease from 1362.7 to 149.7 Ω cm^2; that is, ET rates increase. They also showed that R_{ET} can be further reduced to ~10 Ω cm^2 by increasing sizes of surface-bound NPs via treatment with an Au^{3+}/NH_2OH solution (Figure 51b). After immersion in the Au salt solution for 25 min (Figure 51b, solid triangles), the EIS response of the electrode resembles that of a gold macroelectrode and is limited by ion diffusion. These results are in agreement with the CV studies reported by Musick et al.[368] (see Figure 48).

5.3.2. Electrodes Modified with Redox-Active NP Assemblies

Surfaces modified with mono- or multilayers of redox-active molecules have been studied extensively because of their potential applications in chemical and biochemical sensors (for reviews, see refs 381 and 382). In many sensor applications, it is necessary to increase the number of redox-active molecular layers to enhance sensitivity. However, increasing the number of electroactive layers also requires increasing the amount of intervening material between outer electroactive layers and the electrode. Since molecular layers

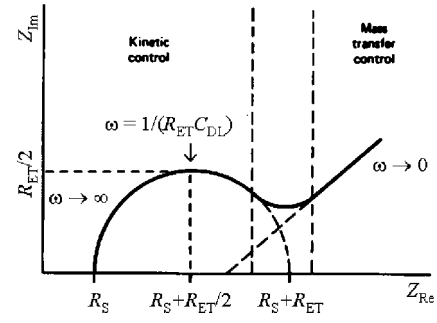

Figure 50. Impedance plot (Nyquist plot) for an electrochemical cell. Reprinted with permission from ref 375. Copyright 1980 John Wiley & Sons, Inc.

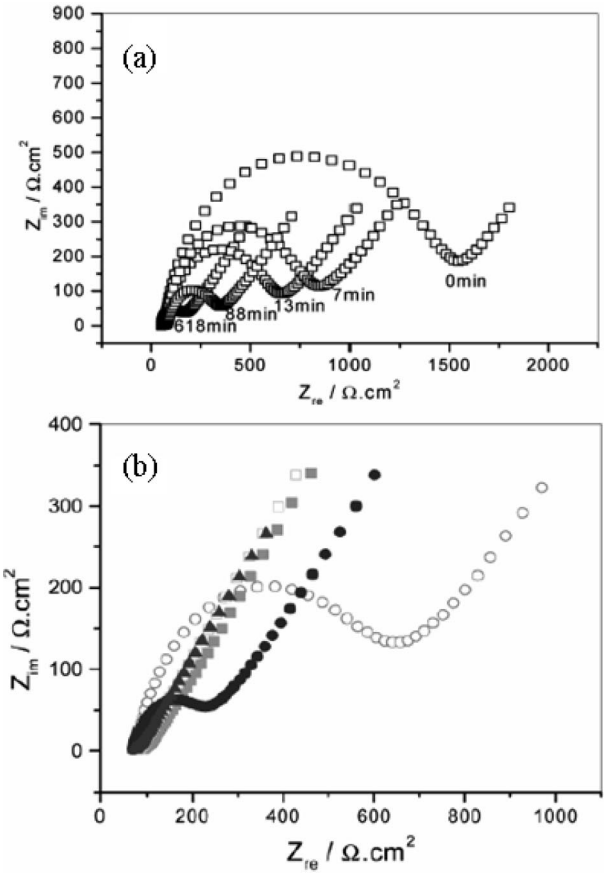

Figure 51. Nyquist plots obtained using Au NP-modified electrodes in 1 mM $Fe(CN)_6^{3-/4-}$/0.1 M KCl. The electrode potential was 0.22 V vs Ag/AgCl, the voltage amplitude was 5 mV, and the frequency ranged 100 kHz−0.1 Hz. (a) Plots for mercaptosilane-functionalized ITO substrates after immersion in a 12 nm Au NP solution for various times as labeled in the graph. (b) Plots obtained using an NP-modified electrode showing the effects of immersion in a 0.3 mM Au^{3+}/NH_2OH aqueous solution. The electrode was initially immersed in an NP solution for 12 min. Open circles, solid circles, solid squares, open squares, and solid triangles correspond to 0, 3, 10, 15, and 25 min immersion in Au^{3+}/NH_2OH solution, respectively. Reprinted with permission from ref 363 (Wang's group). Copyright 2002 American Chemical Society (http://dx-.doi.org/10.1021/la026022b).

often behave as ET barriers, this in turn reduces the ET rate through multilayers and makes the electrochemical response less reversible. This competition between increased electroactivity due to electroactive moieties and reduced ET rates due to intervening material was confirmed, for example, by Zhang et al.[383] using multilayers of glucose oxidase and poly(allylamine)ferrocene (see Figure 52).

Conducting NPs can function as "charge relays", facilitating ET between the redox centers and the electrode surface in multilayer redox-active assemblies. Such hybrid assemblies of metal NPs and redox-active molecules are expected to be both conducting and redox-active. Several novel combinations of NPs and molecules have been studied in this regard, including Au or Ag NPs and derivatives of viologen,[91,95−98] ferrocene,[99−103] bipyridinium cyclophane,[112−115] tetrathiafulvane,[384] thionine,[385] or polyaniline.[84] Assemblies were constructed using stepwise self-assembly driven by covalent or electrostatic interactions.

Escorcia and Dhirani[103] have studied CV responses of multilayers comprising Au NPs and ferrocenylalkanedithiolate (FDT) linkers. They used films with various numbers of layers and with FDT terminal layers (see Figure 53). The

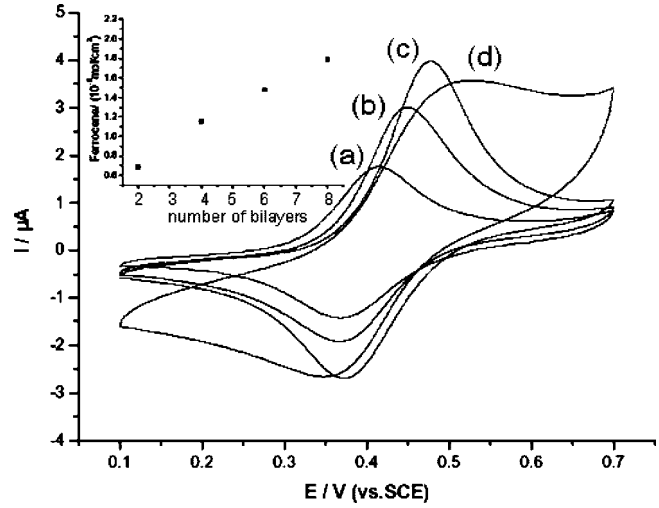

Figure 52. CV scans of a cystamine functionalized Au electrode modified with (a) 2, (b) 4, (c) 6, and (d) 8 bilayers of glucose oxidase/poly(allylamine)ferrocene. The scans were obtained using 0.1 M acetate buffer solution (pH = 5.18). Inset plots ferrocene surface coverage (10^{-9} mol/cm^2) vs the number of bilayers. Surface coverages were determined by integrating anodic scans. Reprinted with permission from ref 383 (Sun's group). Copyright 2004 Elsevier (http://dx.doi.org/10.1016/j.snb.2004.04.012).

CV responses exhibited peaks due to redox of ferrocene within the immobilized cross-linkers. Anodic peak currents increased with the number of layers, indicating that the amount of the electroactive ferrocene moieties increased accordingly. The increase was correlated with film growth as confirmed by UV/vis spectroscopy. As the number of layers increased, full-width at half-maxima (ΔE_{fwhm}) of the peaks tended to increase from 80 to 150 mV initially and then plateaued around 120−150 mV after about five layers. For an ideal monolayer, in which all the redox centers have equivalent environments and interactions between the centers are minimal, theory predicts $\Delta E_{fwhm} = 90.6/n$ mV, where n is the number of electrons involved in the redox reaction.[375] Values exceeding $90.6/n$ mV have been attributed to inhomogeneities in the environment of redox centers arising from disordered structure, for example.[386] Observed values of peak separation (ΔE_p) were found to be remarkably small (~50−58 mV). ΔE_p for immobilized redox species is expected to be 0 V in a reversible ET process,[386] and $\Delta E_p > 0$ in a quasi-reversible or an irreversible process.[387] Similar trends have been commonly observed in multilayer films of NPs and redox-active linkers.[84,91,96,97,100−102,112−114,385]

The overall redox reaction of an electroactive moiety immobilized on an electrode can be expressed as[100]

$$-\mathrm{Red} + \mathrm{A}^-(\mathrm{solv}) \rightarrow -\mathrm{Ox}^+\mathrm{A}^- + \mathrm{e}^-(\mathrm{electrode}) + \mathrm{solv} \quad (93)$$

where −Red and $-Ox^+$, respectively, represent reduced and oxidized states of the immobilized redox species, A^-(solv) is a solvated ion in the solution, $-Ox^+A^-$ is an ion pair, and solv is a solvent molecule. This reaction is composed of two steps: (i) ET from redox centers to the electrode,

$$-\mathrm{Red} \rightarrow -\mathrm{Ox}^+ + \mathrm{e}^-(\mathrm{electrode}) \quad (94)$$

and (ii) ion transport from the electrolyte solution to the redox centers to form ion pairs and maintain charge-neutrality:

$$-\mathrm{Ox}^+ + \mathrm{A}^-(\mathrm{solv}) \rightarrow -\mathrm{Ox}^+\mathrm{A}^- + \mathrm{solv} \quad (95)$$

ET between immobilized redox species and electrodes has been studied extensively.[57] A prototype system is a mono-

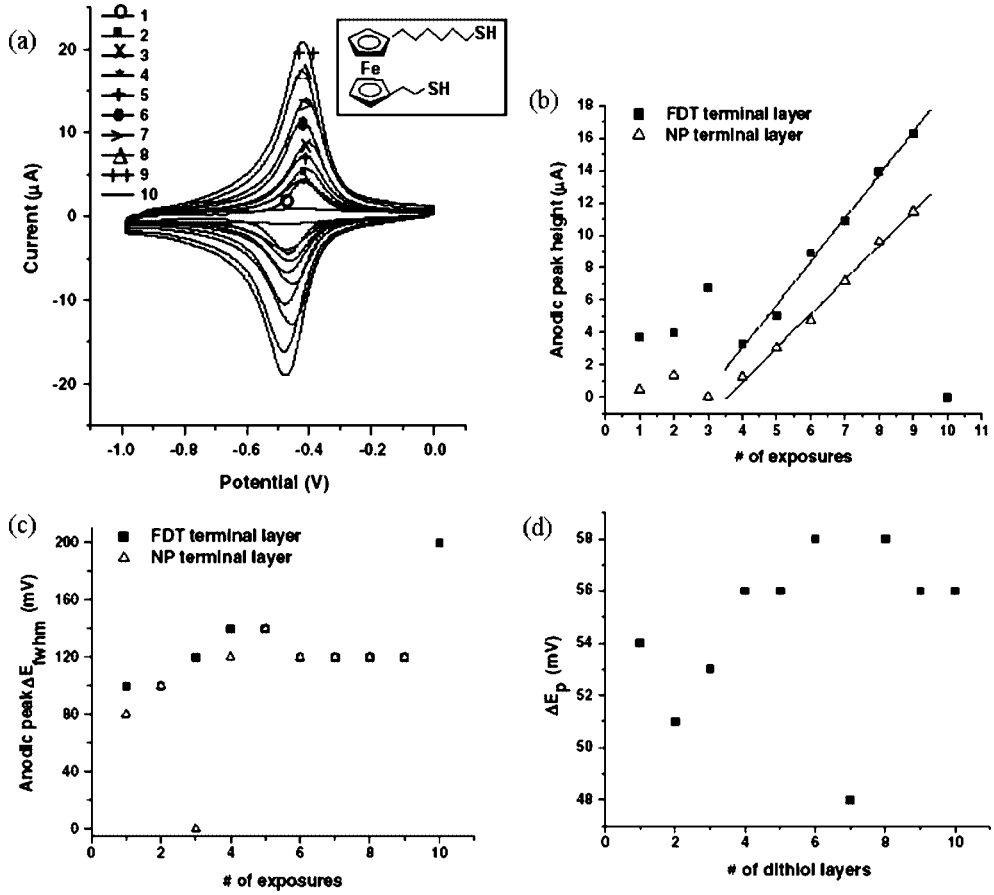

Figure 53. (a) Typical CV scans obtained using FDT/Au NP films with various numbers of layers and with FDT as terminal layers. Films were immersed in a solution of 0.1 M Bu_4NPF_6/CH_3CN, and the scan rate was 480 mV/s. Inset: Chemical structure of ferrocenylalkanedithiol (FDT). Parameters extracted from CV scans: (b) anodic peak height, (c) full width at half-maximum, ΔE_{fwhm}, and (d) redox peak separation, ΔE_p, versus number of layers. Reprinted with permission from ref 103 (Dhirani's group). Copyright 2007 Elsevier (http://dx.doi.org/10.1016/j.jelechem.2006.11.009).

layer of ferrocene-terminated alkanethiolate, $Fc(CH_2)_nSH$, self-assembled on Au electrodes. For example, Smalley et al.[239] have shown that ET between the ferrocene moieties and the electrode is based on tunneling, and the ET rate constant can be expressed as $k_{ET} \propto \exp(-\beta_n n)$ with $\beta_n = 1.2$. Ion transport during the redox reaction can be monitored using an electrochemical quartz crystal microbalance (EQCM). In EQCM, the working electrode of an electrochemical cell is attached to a quartz crystal, and changes in the vibration frequency of the crystal due to changes in the crystal mass are measured. Uosaki and co-workers[100−102] have used EQCM to study ion transport through multilayer films of poly(allyamine hydrochloride)/Au NPs. The NPs were capped with a mixture of mercaptoundecanoic acid, hexanethiol, and ferrocenylhexanethiol and self-assembled on an Au electrode. Figure 54a shows current density and frequency shifts during a CV scan using a five-layer film in 0.1 M $HClO_4$. As the potential was scanned positively from −100 mV, the vibration frequency started to decrease, i.e., the mass increased, due to double-layer charging of the electrode. The frequency decrease (mass increase) became more significant at a potential range of 270−440 mV, i.e., when the ferrocene moiety oxidizes. At more positive potentials, where the oxidation of the ferrocene moiety was complete, a relatively small frequency change was observed. As the potential was decreased, the change in frequency reversed. Figure 54b shows mass change, calculated from frequency change, as a function of the redox charge determined from the oxidation region of the CV scan. A nearly linear relationship was observed with a slope of 245 g mol^{-1} $electon^{-1}$. The data suggest perchlorate ions solvated with ~8 water molecules transfer into (out of) the film during the oxidation (reduction) of the ferrocene moiety.

NPs can, in principle, influence both steps involved in the redox reaction (eqs 94 and 95). With respect to the ET, the distance between the electrode surface and the redox centers located at an outermost layer in multilayer films is usually too long to allow efficient direct electron tunneling. For example, CV responses of multilayer glucose sensors discussed earlier exhibit significantly slower ET rates due to incorporated insulating protein layers (note the decreasing reversibility with increasing number of layers in Figure 52). On the other hand, studies have reported that films with up to 15 layers of NPs and redox-active SAMs exhibit reversible voltammograms.[100] ET through such multilayer films is facilitated by NPs that serve as charge relays. With respect to ion transport, studies have reported that peak currents in CV responses of electrodes modified with viologen[91,97] or ferrocene[103] SAMs reduce upon addition of an NP layer (Figure 55). The loss in electroactivity can be attributed to an inability of electrolyte ions to access some redox moieties located underneath the NPs, rendering these "shadowed" moieties electrochemically inactive.[91,97,103] However, subsequent deposition of a redox-active SAM generally results in an overall net increase in the electroactivity of the assembly (see Figure 53b). This suggests that more redox-active molecules are added on top of the NPs than are

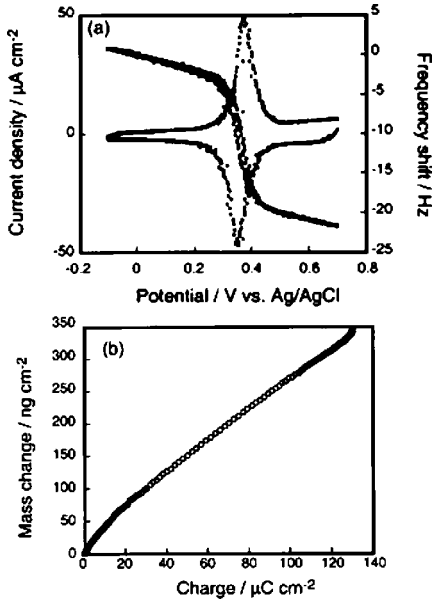

Figure 54. (a) CV and associated frequency changes obtained using an Au electrode with 5 alternating layers of poly(allylamine hydrochloride)/ferrocenylhexanethiolate-capped Au NPs. Data were obtained using 0.1 M $HClO_4$ at $\upsilon = 10$ mV/s. (b) Mass change, calculated from frequency change, as a function of the charge determined from the ferrocene oxidation region (270−440 mV). Reprinted with permission from ref 100 (Uosaki's group). Copyright 2002 Royal Society of Chemistry (http://dx.doi.org/10.1039/b200397j).

rendered inactive below the NPs. This can be attributed to a porous film structure and increasing surface area with film growth.

6. Applications

6.1. Sensors

Among different potential applications of NP assemblies, the most extensively studied are their applications to chemical and biochemical sensing. NP-based sensors can be classified according to their transducing mechanism: electrical, electrochemical, optical, etc. In this review, we focus on electrical and electrochemical-based sensors. For reviews of optical-, photochemical-, or magnetic-based sensors, see refs 16, 17, 49, and 388.

6.1.1. Electrical Sensors

The most widely studied electrical-based transduction mechanism of NP sensors is chemiresistance.[16,21,49,389] Wohltjen and Snow[390] have demonstrated this capability of NP assemblies. They prepared a film of octanethiolate-capped 2 nm Au NPs by spraying a chloroform NP solution onto IDA electrodes at 120 °C. They observed that film conductance changed in the presence of various analyte vapors, including toluene, tetrachloroethylene, 1-propanol, and water. This set of solvents was chosen because they represent analytes with a variety of chemical structures (hydrocarbon, chlorocarbon, hydrogen-bonding polar organic, and very polar inorganic) but similar vapor pressures, allowing direct comparison of chemical selectivity afforded by the NPs. Figure 56 shows responses of the NP film to various vapors at different pressures. Toluene and tetrachloroethylene vapors caused decreases in the film conductance that were large (up

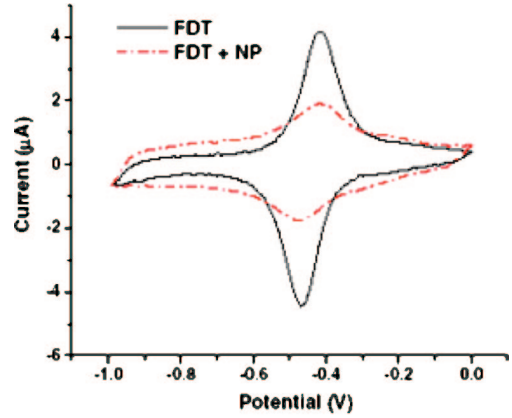

Figure 55. CV scans of a Au wire modified with a self-assembled ferrocenylalkanedithiol (FDT) monolayer (black solid curve) and an FDT/NP bilayer (red dash−dotted curve). In the latter case, NPs were self-assembled on top of the FDT monolayer. Scans were obtained in a solution of 0.1 M Bu_4NPF_6/CH_3CN at $\upsilon = 480$ mV/s. Reprinted with permission from ref 103 (Dhirani's group). Copyright 2007 Elsevier (http://dx.doi.org/10.1016/j.jelechem.2006.11.009).

to 2-fold or more), rapid (90% response in <1 s), and reversible. The drops in conductance were proportional to the vapor pressure and permitted detection limits significantly below 1 ppm. The NP film exhibited negligible response to water and a weak response to 1-propanol.

Several groups have studied NP vapor sensors using a variety of molecular components, including alkanethiol derivatives,[391−398] benzenethiol derivatives,[392,398−401] alkaneamines,[402] alkanedithiols,[403−409] mercaptocarboxylic acids,[172,403,406,410,411] dendrimers,[108−111] and biological molecules such as an extract of lemongrass plant.[412] NP films have been prepared via drop-casting or spray-/spin-coating,[390,392−395,397,399−402,412] stepwise self-assembly,[108−111,172,404,405,410,411,413] cross-linking precipitation,[403,406−408] or Langmuir−Schaefer deposition.[398] A majority of these studies involve Au NPs. A few studies have also reported chemiresistors based on Pt[405] and Pd[397] NPs.

Chemiresistivity of NP-based films is correlated with sorption of analyte molecules into the films as has been demonstrated by quartz crystal microbalance (QCM) measurements.[111,172,392,401,403,410] Figure 57, reported by Han et al.,[403] shows typical conductivity and QCM responses of a film of 5 nm Au NPs cross-linked with 11-mercaptoundecanoic acid (MUA). Film resistance, R, and QCM frequency change, Δf, were measured simultaneously as the film was exposed to flowing nitrogen gas containing analyte vapors. Both R and Δf changed upon introduction of analyte vapor ("on") and returned to their initial values when exposed to pure nitrogen ("off"). The decrease (increase) in Δf corresponds to an increase (decrease) in the film mass proportional to vapor concentration. By calculating the mass of sorbed analyte molecules (e.g., hexane) and taking into consideration their sizes, they estimated that up to ∼20 equivalent layers of analyte molecules could be taken up by the NP film. Vossmeyer and co-workers[111,414] have studied the distribution of absorbed d_4-methanol (CD_3OD) in a multilayer film of Au NP linked with poly(propyleneimine) dendrimers using neutron reflectometry. They found that a significant amount of methanol diffused into and distributed uniformly across the bulk of the film. The ability to uptake large amounts of analyte molecules due to high porosity is an attractive feature of NP film chemiresistors.

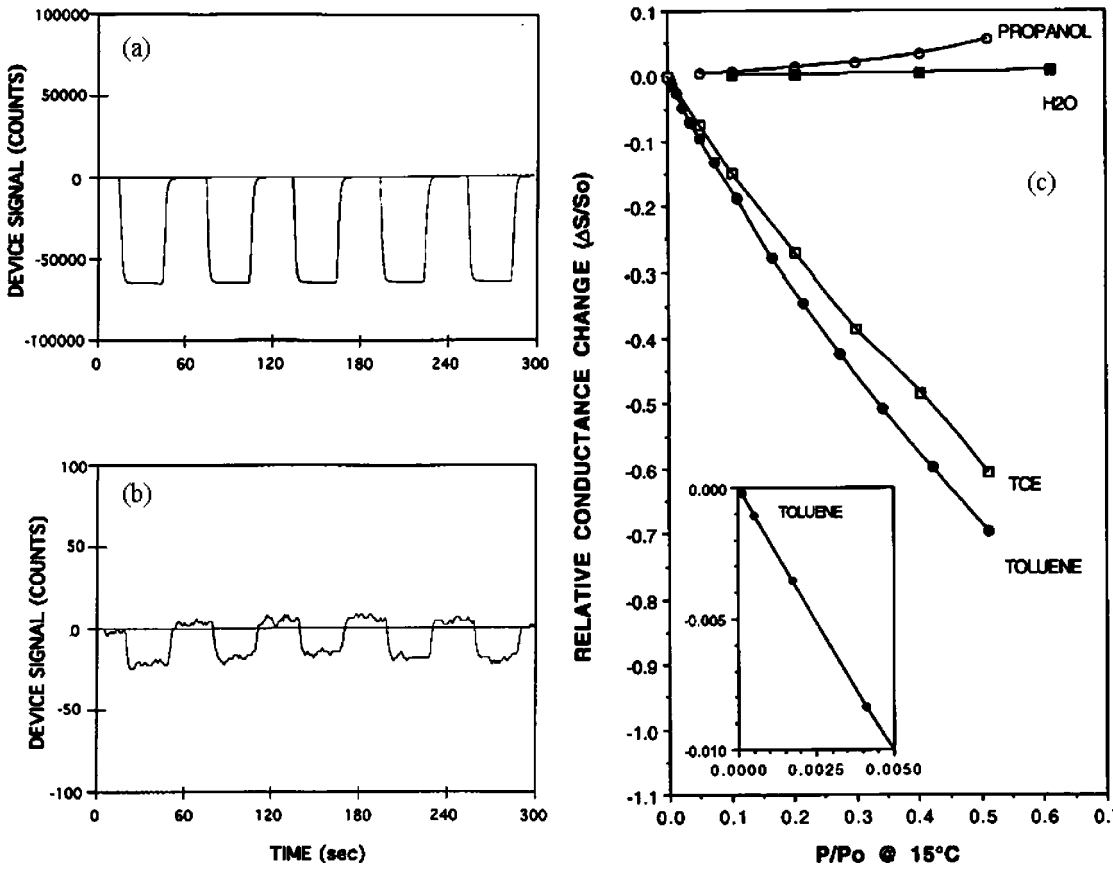

Figure 56. Responses of an NP sensor to five 60 s toluene vapor exposure/purge cycles at concentrations of (a) 11000 and (b) 2.7 ppmv in dry air. The device signal is proportional to the sensor resistance. Baseline signal (0 device signal counts) corresponds to 1.5 MΩ, and those at 11000 and 2.7 ppmv of vapor correspond to 3.4 MΩ and 420 Ω, respectively. (c) Response of the NP sensor to various vapor pressures of toluene, tetrachloroethylene (TCE), 1-propanol, and water at 15 °C. Inset displays the reponse to toluene down to 2.7 ppmv. Reprinted with permission from ref 390 (Snow's group). Copyright 1998 American Chemical Society (http://dx.doi.org/10.1021/ac9713464).

Evans and co-workers[399,400] have correlated ellipsometric and conductance measurements to rationalize NP film response to various solvent vapors. They prepared films of Au NPs by spin-coating NP solutions onto a silicon wafer. Au NPs were capped with benzenethiols (p-HSC_6H_4X, where X = OH, CH_3, NH_2, COOH). Ellipsometric response of the NP films indicated that both thickness and permittivity of the films changed upon exposure to solvent vapor (Figure 58). Both factors can, in principle, affect the film conductivity. Conductivity of an NP film (in a weak coupling regime) can be expressed as

$$\sigma \propto e^{-\beta s}\, e^{-E_C/k_B T} \tag{96}$$

Variations in the inter-NP separation, s, and relative permittivity, ε_r, modify tunneling probability and activation energies ($E_C \approx e^2/4\pi\varepsilon_r\varepsilon_0 r$), respectively, significantly affecting σ. However, s and ε_r can yield counterbalancing effects on σ. Increases in film thickness observed in ellipsometric measurements upon exposure to analyte vapor are associated with film swelling. This increases inter-NP separation and lowers σ. On the other hand, since permittivities of organic solvents are larger than that of air (or vacuum), diffusion of solvent molecules into pores of the film lowers E_C and increases σ. Evans and co-workers[400] observed that σ of films of NPs capped with 4-mercaptophenol (p-HSC_6H_4OH) and exposed to ethanol vapor increased at <90 ppt ethanol but decreased at higher partial pressures. They concluded that the influences of ε_r and s dominated in these two regimes, respectively.

By measuring capacitance, Pang et al.[407] confirmed that analytes can induce changes in permittivity of NP films. They simultaneously measured resistance and capacitance of a film of octanethiolate-capped Au NPs cross-linked with hexanedithiol as a function of relative humidity (RH) (see Figure 59). They found that, at low humidity (RH ≤ 40%), the film exhibited increased resistance and negligible capacitance changes. However, above RH ≈ 43%, the resistance began to decrease and capacitance began to increase, suggesting a significant change in the permittivity of the film. Again, the interplay between film swelling and permittivity can explain film responses. Joseph et al.[413] have investigated the importance of film swelling versus changes in permittivity using multilayer films of Au NPs cross-linked by flexible or rigid molecules. They chose dodecanedithiol and [4]-staffane-3,3‴-dithiol linkers as flexible and rigid linkers, respectively. Both are saturated hydrocarbons with similar lengths and hydrophobicity. They observed that the resistance of the NP film containing the rigid linker decreased when the film was exposed to vapors of tolyene, 4-methyl-2-pentanone, 1-propanol, or water. The NP film containing the flexible linker, on the other hand, exhibited an increase in resistance to all analytes. These observations suggest that, in the case of the rigid linker, the ability of the NP film to swell upon vapor sorption should be significantly reduced, and film response could be due to change in permittivity.

Chemical selectivity and sensitivity of NP-based chemiresistors are generally controlled by solubility properties of molecules incorporated into the chemiresistors. For example,

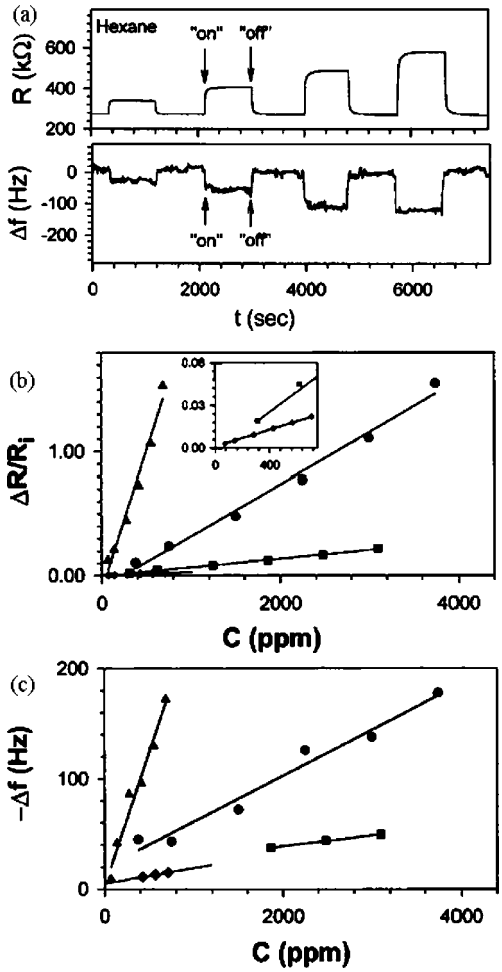

Figure 57. (a) Resistance, R, and QCM frequency change, Δf, for an MUA-capped 5 nm Au NP film due to hexane sorption/desorption. Peak heights correspond to (from left to right) 749, 1499, 2248, and 2998 ppm. (b) Relative resistance change, $\Delta R/R$, and (c) frequency change, Δf, vs vapor concentration, C, of toluene (▲), hexane (●), methanol (■), and water (♦). Inset in (b) shows an enlarged view of the methanol and water data in the low-concentration region. Reprinted with permission from ref 403 (Zhong's group). Copyright 2001 American Chemical Society (http://dx.doi.org/10.1021/ac0104025).

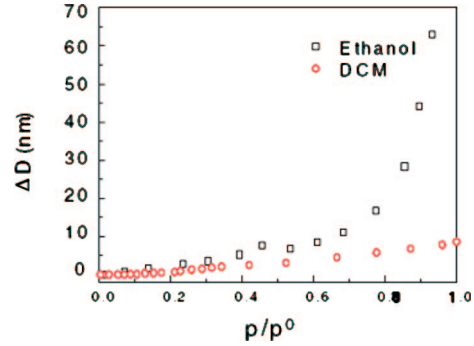

Figure 58. Thickness changes of OH-functionalized NP films induced by exposure to dichloromethane and ethanol, as a function of partial pressure of analyte. Reprinted with permission from ref 400 (Evans's group). Copyright 2002 Institute of Physics Publishing Ltd. (http://dx.doi.org/10.1088/0957−4484/13/3/339).

Zhang et al.[400] have observed that 4-methylbenzenethiolate-capped Au NPs are more sensitive to vapors of nonpolar solvents (e.g., dichloromethane) while 4-mercaptophenol-capped NPs are more sensitive to vapors of polar solvents

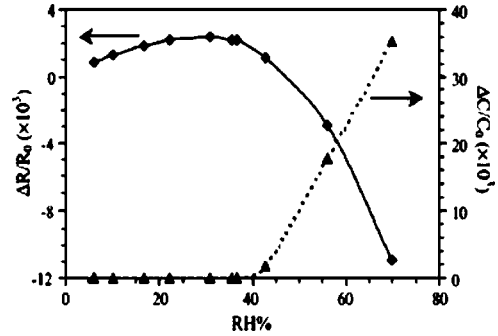

Figure 59. Relative resistance, $\Delta R/R$, and capacitance, $\Delta C/C$, changes of a Au NP film vs relative humidity (RH%). The film was prepared by cross-linking octanethiolate-capped Au NPs with 1,6-hexanedithiol. Reprinted with permission from ref 407 (Cai's group). Copyright 2006 Elsevier (http://dx.doi.org/10.1016/j.snb.2005.07.036).

(e.g., methanol). Kim et al.[394] have reported that films of Au NPs capped with a mixture of chlorobenzenemethanethiol and octanethiol ligands displayed different responses to 1-propanol, acetone, and cyclohexane as the ratio between the capping ligands was varied. Joseph et al.[404] observed that responses of $HS(CH_2)_nSH$-linked Au NP films to vapors of toluene and tetrachloroethylene increased (exponentially) with n. They proposed that the number of sorption sites for these vapor molecules is determined by the amount of organic material in the films. Krasteva et al.[109,110] observed that multilayer films of Au NPs linked with various types of organic dendrimers (e.g., polyphenylene, polyamidoamine, and polypropyleneimine) exhibited both tunable sensitivity and selectively to vapors of toluene, 1-propanol, and water. Vapor selectivities of the Au/dendrimer films corresponded well with the solubility properties of the dendrimers. In addition, they observed that Au NP/poly(propyleneimine) films, comprising dendrimers of generation 1−5, exhibited increased sensitivities to toluene and 1-propanol with increasing size of dendrimers. The sensitivity to water was rather unaffected. They proposed that the dendrimers provide selective interaction sites for sorption of solvent molecules. That is, toluene and 1-propanol molecules are preferentially "solvated" within the dendrimers and, in this sense, the dendrimer macromolecules can be viewed as nanocontainers for the analyte molecules. Interaction sites for water sorption are likely the primary amino groups at the surface of the dendrimers; their number is independent of dendrimer size.

Zellers and co-workers[415] have proposed an analytical model to parametrize response of NP-based chemiresistors as a function of variables associated with analyte vapors, NP films, and the vapor−NP interactions. Their model allows predictions of chemiresistors responses to within 24% accuracy. In addition, they[416] have exploited the fast, reversible, and selective responses of NP-based chemiresistors to develop gas-chromatography detectors for vapor recognition and quantification. The sensitivities and detection limits of the chemiresistors were comparable to those of commonly used flame-ionization detectors and polymer-coated surface acoustic wave sensors.

NP-based chemiresistors can also be used for gas detection. Briglin et al.[402] prepared films of dodecylamine-capped Au NPs by drop-casting the NPs on IDA electrodes. Upon exposure to thiol-containing gases (such as H_2S, CH_3SH, C_3H_7SH), the films exhibited irreversible decrease in resistance. Optical spectroscopic and TEM data indicated that

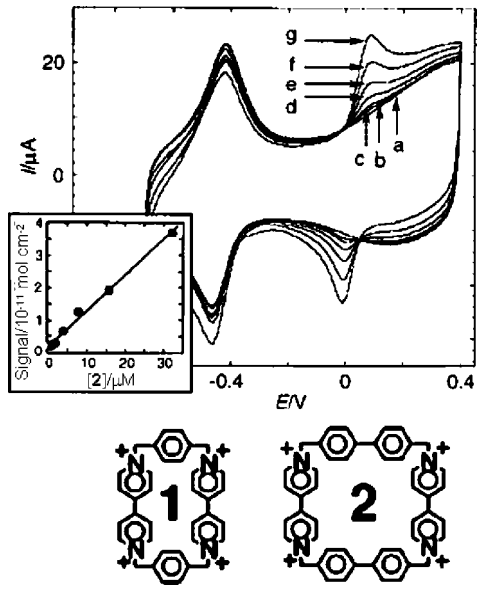

Figure 60. Chemical structures of cyclobis(paraquat-*p*-phenylene), **1**, and cyclobis(paraquat-*p*-biphenylene), **2**. CV scans obtained using a five-layer film of Au NPs linked with **1** and immersed in solutions with various concentrations of *p*-hydroquinone: (a) 0, (b) 1, (c) 2, (d) 4, (e) 8, (f) 16, and (g) 32 μM. Inset: Calibration curve for electrochemical sensing of *p*-hydroquinone. Data were calculated by coulometric assay of the reduction peak of *p*-hydroquinone. All data were recorded under argon in 0.1 M phosphate buffer, pH = 7.2, υ = 100 mV/s. Reprinted with permission from ref 112 (Willner's group). Copyright 1999 the Royal Society of Chemistry (http://dx.doi.org/10.1039/a902763g).

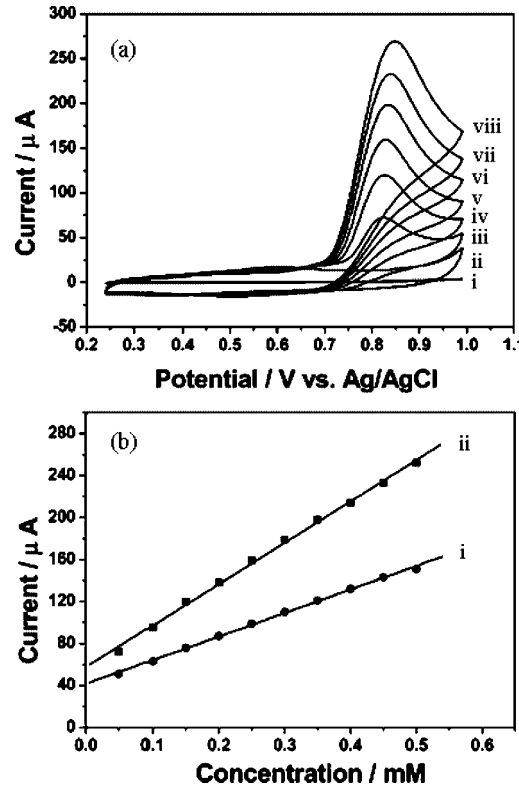

Figure 61. (a) CV scans of (i) a bare ITO electrode and (ii−viii) a poly(ethylenimine)/$[(PSS/PAH)_2/PSS/Au\ NP]_3$-modified electrode. The electrodes were immersed in phosphate buffer solution (pH = 2.0) containing various concentrations of $NaNO_2$: (i) 0.5, (ii) 0, (iii) 0.05, (iv) 0.15, (v) 0.25, (vi) 0.35, (vii) 0.45, and (viii) 0.55 mM. υ = 50 mV/s. (b) Amperometric responses vs concentration of $NaNO_2$ obtained using ITO electrodes modified with (i) poly(ethylenimine)/$(PSS/PAH)_2/PSS/Au\ NP$ and (ii) poly(ethylenimine)/$[(PSS/PAH)_2/PSS/Au\ NP]_3$. Reprinted with permission from ref 420 (Caruso's group). Copyright 2003 American Chemical Society (http://dx.doi.org/10.1021/nl034363j).

the thiols displaced the amine caps, allowing the Au NP cores to approach and, in some cases, contact each other, lowering the film resistance.

6.1.2. Electrochemical Sensors

6.1.2.1. Chemical Sensors. Electrodes modified with NP assemblies have been used in many demonstrations of electrochemical sensing.[14−17] Willner and co-workers[112−115] used assemblies of Au NPs cross-linked with macromolecules such as bipyridinium cyclophanes, **1** or **2** (see Figure 60). These macromolecules can act as receptors for π-donor analytes and, thus, enable concentration of guest analytes at the electrode surface. Figure 60 shows CV scans of an ITO electrode modified with a five-layer film using **1**. The scans were obtained in the presence of *p*-hydroquinone (HOC_6H_4OH). The linear response of the electrode as indicated by the calibration plot (Figure 60 inset) implies detection of *p*-hydroquinone at bulk concentrations as low as 1 μM. Using the same macromolecule−NP system, they were also able to sense other π-donor guests such as dihydroxyphenyl acetic acid as well as the neurotransmitters adrenaline and dopamine. Selectivity of these electrodes was controllable by the structure and size of the macromolecule receptors. For example, dihydroxymethyl ferrocene was detecable using the larger receptor **2** but not the smaller receptor **1**. An NP film consisting of three layers of **1**-cross-linked NPs and three layers of **2**-cross-linked NPs, however, enabled sensing of both *p*-hydroxyquinone and bihydroxymethyl ferrocene.[115]

Incorporating NPs with electrocatalytic properties into electrochemical sensors offers several benefits, namely, decreased overpotentials, increased reversibility, and enhanced sensitivity. The latter can be controlled through the amount of NPs incorporated into the sensors.[417] NPs, because of their small sizes, can exhibit enhanced catalytic activity relative to bulk materials (for a review on catalytic activities of NPs, see refs 5 and 418). Gold, for example, is a poor catalyst in bulk form, but Au NPs are excellent catalysts for oxidation of CO, H_2, and CH_3OH and reduction of O_2 and NO.[44] Abdelrahman et al.[419] used CV to study electrocatalytic reduction of O_2 by 1,4-benzenedimethanedithiol (BDMT)/Au NP multilayers on Au electrodes. They observed that addition of an Au NP layer not only restored the O_2 reduction peak that was entirely inhibited by the preceding BDMT but also decreased the reduction peak potential and increased the peak current compared with that obtained using a bare Au electrode. Yu et al.[420] utilized ITO electrodes modified with polyelectrolyte/Au NP multilayer films to detect nitric oxide (NO) electrochemically. They prepared the films by incorporating 4-(dimethylamino)pyridine-stabilized Au NPs into multilayers of poly(sodium 4-stryrenesulfonate), PSS, and poly(allylamine hydrochloride), PAH. They investigated electrocatalytic activity of the Au NPs in the films using sodium nitrite ($NaNO_2$) as a precursor of NO. Figure 61a shows CV scans of an ITO electrode modified with three layers of polyelectrolyte/NP. Using a bare ITO electrode, they observed almost no response arising from NO oxidation. In contrast, using the polyelectrolyte/NP-modified electrode,

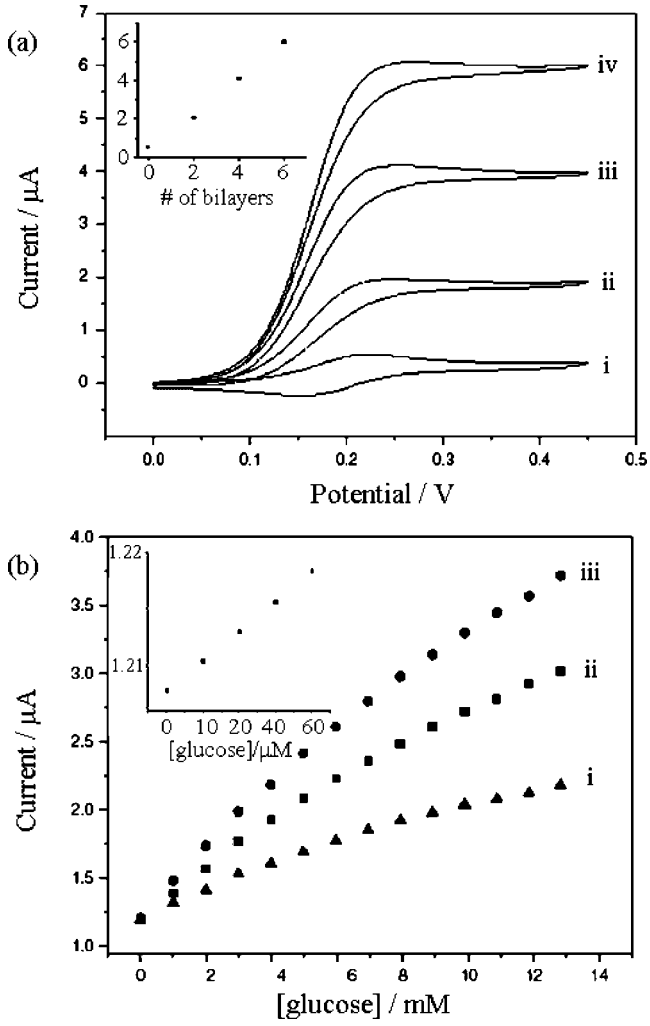

Figure 62. (a) CV scans obtained using electrodes functionalized with (i) 0, (ii) 2, (iii) 4, and (iv) 6 bilayers of GOx/Au NPs. Electrodes were immersed in a solution containing 20 mM glucose, 0.1 M phosphate buffer (pH = 6.8), and 0.25 mM ferrocenemethanol as a diffusional ET mediator. Inset: Plot of anodic plateau currents vs numbers of bilayers. Scan rate = 5 mV/s. (b) Plots of peak current vs glucose concentration for (i) 2, (ii) 4, and (iii) 6 bilayers of GOx/NP. Inset: A similar plot for 6-bilayers using low glucose concentrations. Reprinted with permission from ref 461 (Sun's group). Copyright 2006 Elsevier (http://dx.doi.org/10.1016/j.elecom.2005.11.014).

they observed an oxidation peak with a peak current that increased with increasing concentration of $NaNO_2$ in solution. The sensitivity of the modified electrode depended on the number of layers or the Au NP content of the film (Figure 61b).

Other examples of electrocatalytic NP sensors include Au electrodes functionalized with Au NP/cystamine assemblies for sensing dopamine in the presence of ascorbic acid,[421] ITO electrodes functionalized with Cu NP/(3-mercaptopropyl)trimethoxysilane thin films for detecting sodium nitrite,[422] ITO electrodes coated with Au NPs prepared by a seed-mediated growth method for sensing paracetamol,[423] and ITO electrodes functionalized with multilayer films composed of Prussian blue (a typical hexacyanoferrate) NPs and poly(allylamine hydrochloride) for detecting H_2O_2.[424]

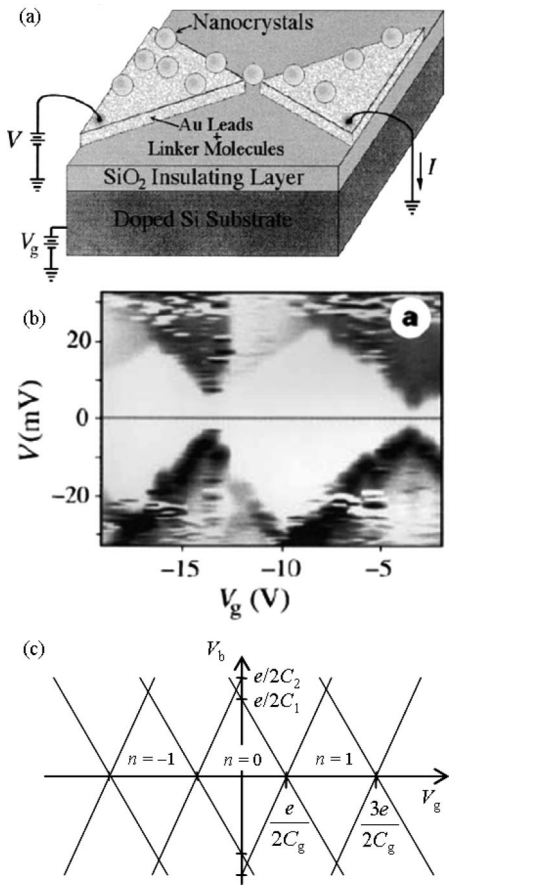

Figure 63. (a) Schematic of a CdSe NP SET device. (b) Grey-scale plot of the differential conductance of the device as a function of both bias and gate voltage at 4.2 K. The white diamond-shaped regions correspond to Coulomb blockade. Reprinted with permission from ref 178 (McEuen's group). Copyright 1997 Nature Publishing Group (http://dx.doi.org/10.1038/39535). (c) Diamond plots produced by eqs 98 and 99, assuming $C_1 > C_2$.

6.1.2.2. Biosensors. Biocompatibility of NPs made of several types of materials, notably Au, Ag, Pt, CdS, CdSe, SiO_2, and TiO_2, have allowed fabrication of NP−biomolecule hybrid assemblies in which the biomolecules retain their bioactivities. Synthesis, properties, and applications of NP−biomolecule hybrid materials have already been reviewed[17,18,20,417,425−431] and are not discussed here in detail. NPs provide a general route for the development of biosensors as they enable immobilization of a variety of biomolecules. These include DNA[430−433] as well as proteins such as enzymes,[434] antigens,[435] and antibodies.[436−439] In addition, NPs can function as electron relays facilitating electron transfer between electrode surfaces and redox-active biomolecules. Bioelectroactivity facilitated by NPs has been demonstrated using a wide range of biomolecules, including horseradish peroxide,[440−451] glucose oxidase,[440,452−463] cytochrome *c*,[366,464,465] xanthine oxidase,[440,466] hemoglobin,[444,467−471] myoglobin,[444,472−474] microperoxidase-11,[475] and fructose dehydrogenase.[476] These studies have used NPs made of various materials including Au, SiO_2,[435,444] Ag,[437,448,464,467] TiO_2,[446] Pt,[455] ZrO_2,[470] and CdS.[471] As an example, Sun and co-workers[458−463] have reported that gold or silica NPs can greatly enhance bioelectrocatalytic activity of glucose oxidase (GOx) and can be used to construct glucose biosensors with high stability and sensitivity. Figure

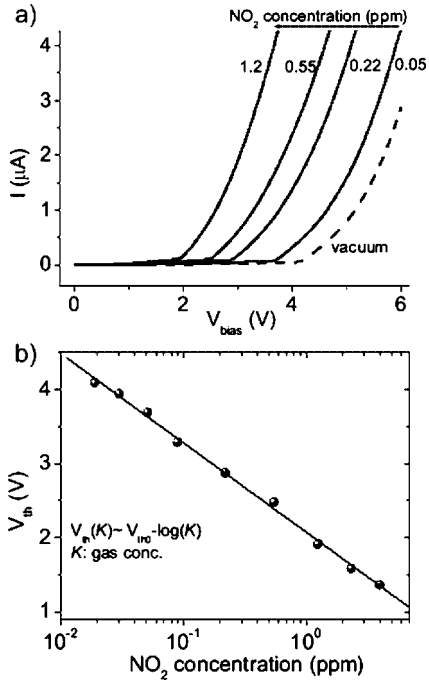

Figure 64. (a) $I-V$ curves of a Si NP array exposed to various NO_2 concentrations. NO_2 molecules narrow the CB gap. (b) Dependence of the CB threshold on NO_2 concentration. Reprinted with permission from ref 483 (Borini's group). Copyright 2006 Wiley-VCH Verlag GmbH & Co. KGaA (http://dx.doi.org/10.1002/adma.200600198).

62 shows some of their CV scans obtained using electrodes modified with different numbers of GOx/Au NP bilayers and immersed in glucose solutions with various concentraions. Anodic peak currents increased linearly with both the number of bilayers and the concentration of glucose in solution.

6.2. Electronics

6.2.1. Transistors

Control over the number of excess charges on NPs has enabled their application in single-electron transistors (SETs). Klein et al.[178] have demonstrated an SET made from chemically synthesized NPs. They fashioned the device by fabricating two nanometer-separated Au electrodes (source/drain electrodes) on a silicon/silicon−oxide substrate (gate/gate oxide) using lithography. They then assembled a 1,6-hexanedithiol monolayer on the electrodes and deposited 5.5 nm CdSe NPs to bridge the gap between the electrodes (Figure 63a). Plots of source−drain conductance measured at 4.2 K as a function of both bias and gate voltages exhibited diamond-shaped regions (Figure 63b). These so-called "Coulomb diamonds" correspond to Coulomb blockade (CB) thresholds varying with gate voltage.

The operation of the SET can be understood as follows. The gate voltage, V_g, induces a charge $Q_0 = C_gV_g$ on the NP, where C_g is the capacitance between the NP and the gate. The total charge on the NP then will be $Q = Q_0 + ne$, where n is an integer. We only consider $-e/2 \le Q_0 \le e/2$ since an integer number of e can always be absorbed in n. The energy, $\Delta U^{\pm}$, required to add (+) or remove (−) an electron to/from the NP now becomes (eq 38)

$$\Delta U^{\pm} = \frac{(Q \pm e)^2}{2C_\Sigma} - \frac{Q^2}{2C_\Sigma} = \frac{\pm 2e(Q_0 + ne) + e^2}{2C_\Sigma} = \pm\frac{eC_gV_g}{C_\Sigma} + (\pm 2n + 1)\frac{e^2}{2C_\Sigma} \quad (97)$$

where $C_\Sigma = C_1 + C_2 + C_g$ is the total capacitance of the SET and C_1 and C_2 are the capacitances between the NP and the source and drain electrodes. Equation 97 indicates that $\Delta U^{\pm}$ varies linearly with V_g. The CB voltage threshold can be obtained using eqs 35, 37, and 40. At absolute zero, the tunneling rates are suppressed under the following conditions:

$$\Delta E_1^{\pm} \le 0 \Rightarrow -\Delta U^- \le \frac{eC_2V_b}{C_\Sigma} \le \Delta U^+ \Rightarrow C_gV_g + \left(n - \frac{1}{2}\right)e \le C_2V_b \le C_gV_g + \left(n + \frac{1}{2}\right)e \quad (98)$$

$$\Delta E_2^{\pm} \le 0 \Rightarrow -\Delta U^+ \le \frac{eC_1V_b}{C_\Sigma} \le \Delta U^- \Rightarrow -C_gV_g - \left(n + \frac{1}{2}\right)e \le C_1V_b \le -C_gV_g - \left(n - \frac{1}{2}\right)e \quad (99)$$

Inequalities 98 and 99 result in diamond-shaped regions (Figure 63c) inside which conductance is zero and the number of electrons on the NP is constant.

CB based transistors have also been fabricated using NP arrays. Sato et al.[180] and Weiss et al.[187] have reported fabrication of such devices using chains of 1,6-hexanedithiolate-linked 10 nm Au NPs and octanethiolate-capped 50 nm Au NPs, respectively. Suganuma and Dhirani[12] have shown that films of 1,4-butanedithiolate-linked Au NPs self-assembled in a stepwise fashion on a Si/SiO_2 substrate exhibit CB that can be gated. Talapin and Murray[477] have reported that drop-cast thin films of semiconducting NPs (such as PbSe, PbS, PbTe, CdSe, and InP QDs), when chemically activated by hydrazine, exhibit room-temperature transistor behavior and allow reversible switching between electron- and hole-dominated transport.

Potential applications of single-electron devices have been the subject of a number of reviews.[478−481] Such applications may be analog or digital in nature and include electrometry, current metrology, thermometry, and data storage. Self-assembly of solution-based NPs can provide a route to rapid and cost-effective fabrication of these devices.[482] However, because of practical challenges, large-scale and reproducible fabrication of commercial single-electron devices based on NP assemblies has not been realized.

6.2.2. Transistor-Based Sensors

Borini et al.[483] have shown that CB thresholds of silicon NP arrays are very sensitive to the presence of molecules, such as NO_2, that have high electron-affinities. They fabricated 3D arrays of Si NPs by electrochemically etching doped silicon. The NP arrays exhibited room-temperature CB thresholds that decreased in the presence of increasing concentration of NO_2 due to gating by the molecules (Figure 64). Their observation suggests that the arrays can function as CB gas sensors operable at room-temperature.

NP arrays also enable ion-sensitive field-effect transistors (ISFETs) capable of detecting charged species near the gate surface. Figure 65a shows a schematic of an ISFET described by Kharitonov et al.[484] The ISFET was fabricated by

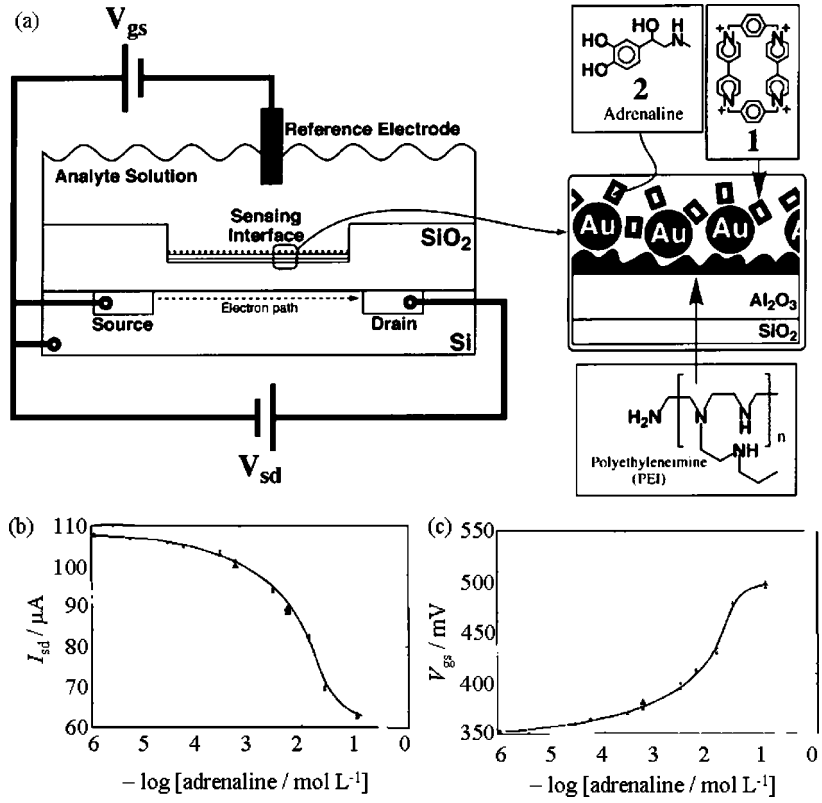

Figure 65. (a) Schematic illustrations of an ISFET. The sensor's interface consists of polyethyleneimine/Au NP/cyclobis(paraquat-*p*-phenylene) **1**. (b) Source−drain current at different concentrations of adrenaline. $V_{gs} = 1.5$ V and $V_{sd} = 0.5$ V. (c) V_{gs} at different concentrations of adrenaline. $I_{sd} = 100$ mA and $V_{sd} = 0.5$ V. All experiments were performed using a 0.1 M phosphate buffer solution (pH = 7.6) and Ag/AgCl as the reference electrode. Reprinted with permission from ref 484 (Willner's group). Copyright 1999 American Chemical Society (http://dx.doi.org/10.1021/ac990997s).

sequentially depositing polyethyleneimine, citrate-stabilized Au NPs, and cyclobis(paraquat-*p*-phenylene) macromolecules on an Al_2O_3 substrate. The macromolecules act as hosts for π-donor guest analytes. The ISFET was then used to sense adrenaline by either (i) monitoring the source−drain current (I_{sd}) at fixed gate-source potential (V_{gs}) or (ii) measuring V_{gs} required to maintain fixed I_{sd}. Figure 65 (parts b and c) displays the ISFET's responses to different concentrations of adrenaline. Xu et al.[485] have reported fabrication of an ISFET biosensor using stepwise self-assembly of MnO_2 NPs and lactate oxidase. The biosensor was able to detect low concentrations of lactate with a detection limit of 8.0 μM.

6.2.3. Data Storage

Suganuma et al.[13] have recently shown that self-assembled NP films can be used to store analog data. Using stepwise self-assembly, they prepared multilayer films of 1,4-butanedithiolate-linked Au NPs on a Si/SiO_2 substrate. The device had a field-effect transistor configuration with electrodes deposited on the film serving as source and drain electrodes and the underlying silicon as a gate electrode. The authors observed that an applied gate voltage caused a CB gap to shift away from zero source−drain voltage. In addition, if a gate voltage was applied as the device was slowly cooled below a threshold temperature (~175 K), the CB gap remained shifted even after the gate voltage was turned off. That is, the value of the applied gate voltage was effectively *recorded*. Figure 66 (parts a−c) shows maps of differential conductance vs source−drain bias and gate voltage obtained at 77 K, demonstrating stored gate voltages of −5, 0, or +5 V applied during cooling. The authors argued that, above a threshold temperature, background charges redistribute in order to cancel gate-induced electric fields. As the temperature is lowered, eventually these charges can become trapped or "frozen", creating a charge glass that generates gating fields even after the gate voltage is removed. The recorded value of gate voltage is *read* through the shift in CB gap. Since the gate voltage can be varied continuously, these films can be used as analog memory storage devices. As the devices were warmed, the CB gap became weaker and eventually vanished at ~175 K, *erasing* stored information. The authors were also able to store multivalued information by applying multivalued time-dependent gate voltages during cooling. Figure 66d shows two examples. The authors applied cyclic time-dependent gate voltages, generating 77 K conductance maps that resemble "••−" and "−" corresponding to "U" and "T" in Morse code, respectively.

7. Summary

NP assemblies exhibit bulk properties that are controllable from the bottom up. NPs with a variety of optical, chemical, and electronic functionalities can be prepared by chemical synthetic methods. Molecules—either as capping ligands or cross-linkers—can confer additional functionalities (such as chemical or biorecognition), control inter-NP separations, and influence the rate of charge transfer between NPs. Properties of assemblies can be further controlled via assembly procedure. Assemblies can be organized into 1D, 2D, and 3D arrays of various length scales with controllable degrees of order/disorder. They can exhibit unusual architectural

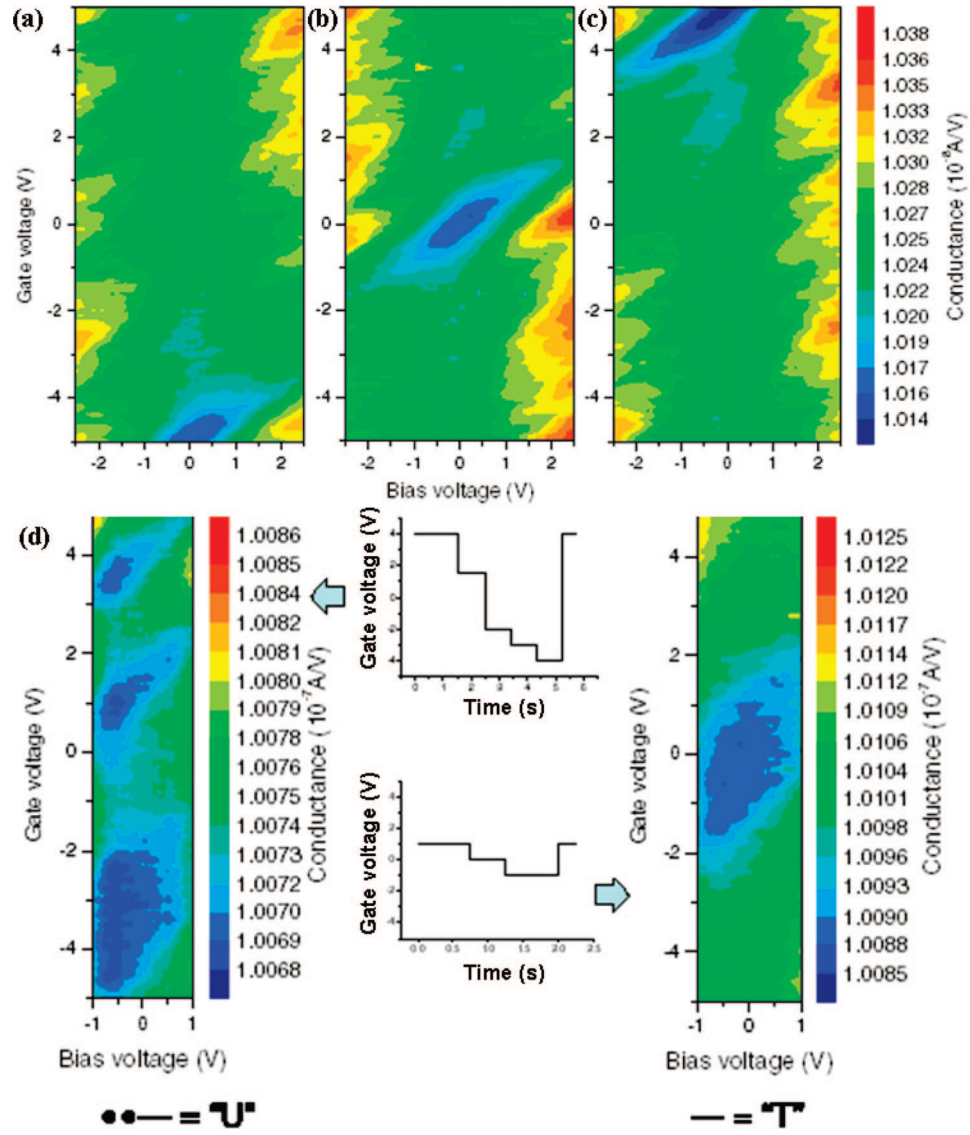

Figure 66. Differential conductance maps showing stored applied gate voltages. The maps were obtained at 77 K. As the device was cooled to 77 K, values of the gate voltage was kept constant at (a) −5 V, (b) 0, or (c) +5 V. (d) Differential conductance maps (left and right) measured at 77 K after cyclic gate voltages (center) were applied during cooling. The stored information in the conductance maps reading from $V_g = 5$ V toward −5 V resembles "••−" and "−", which correspond to "U" and "T", respectively, in Morse code. Reprinted with permission from ref 13 (Dhirani's group). Copyright 2005 Institute of Physics Publishing Ltd. (http://dx.doi.org/10.1088/0957−4484/16/8/037).

features such as large porosity and surface area that can be desirable depending on application.

The controlled functionality afforded by NP assemblies combined with the ability of NPs to serve as charge relays has enabled a host of new opportunities, both fundamental and applied. Assemblies have enabled systematic studies of phenomena ranging from single-electron charging to metal−insulator transitions. In terms of applications, there has been particular interest in exploiting functionality of NP assemblies for electronic chemical and biological sensing. A number of proof-of-principle devices, such as vapor-, electrochemical-, chemical-, and biosensors, have already been demonstrated. Further studies are required to explore more fully the large range of material properties and applications enabled by the large choice of assembly components (including mixtures of NPs) and architectures. In view of the desirable features of electronics (such as low cost, scalability, integrability, etc.), this area will likely continue to represent a significant target of opportunity for future studies.

8. Abbreviations

1D	one-dimensional
2D	two-dimensional
3D	three-dimensional
ac	alternating current
AFM	atomic force microscope/microscopy
BDMT	1,4-benzenedimethylthiol
cHDMT	1,4-cyclohexanedimethylthiol
CB	Coulomb blockade
CP-AFM	conductive-probe atomic force microscope
CV	cyclic voltammetry
D−B−A	donor−bridge−acceptor
dc	direct current
DNA	deoxyribonucleic acid
DOS	density of states
DPV	differential pulsed voltammetry
EA	electron affinity
EIS	electrochemical impedance spectroscopy
EQCM	electrochemical quartz crystal microbalance
ES	Efros and Shklovskii

ET	electron transfer
FDT	ferrocenylalkanedithiol
GOx	glucose oxidase
hcp	hexagonal close-packed
HOMO	highest occupied molecular orbital
IE	ionization energy
IDA	interdigitated array
IR	infrared
ISFET	ion-sensitive field-effect transistor
ITO	indium tin oxide
LDOS	local density of states
LIA	lock-in amplifier
LUMO	lowest unoccupied molecular orbital
MIT	metal−insulator transition
MPTMS	3-(mercaptopropyl)trimethoxysilane
MUA	11-mercaptoundecanoic acid
MW	Middleton and Wingreen
NMR	nuclear magnetic resonance
NNH	nearest-neighbor hopping
NP	nanoparticle
PAH	poly(allylamine hydrochloride)
PDMA	polydimethylsiloxane
PSS	poly(sodium 4-styrenesulfonate)
PTFE	polytetrafluoroethylene
QCM	quartz crystal microbalance
QD	quantum dot
QDL	quantized double-layer
QLH	quasi-localized hopping
RH	relative humidity
RT	room temperature
SAM	self-assembled monolayer
SAXS	small-angle X-ray scattering
SECM	scanning electrochemical microscope/microscopy
SEM	scanning electron microscope/microscopy
SET	single-electron transistor
STM	scanning tunneling microscope/microscopy
TCR	temperature coefficient of resistance
TEM	transmission electron microscope/microscopy
TOP	trioctylphosphine
TOPO	trioctylphosphine oxide
UME	ultramicroelectrode
UV/vis	ultraviolet/visible
VRH	variable-range hopping
WKB	Wentzel−Kramers−Brillouin
a_0	Bohr radius of hydrogen atom
α	numerical coefficient
A	cross-sectional area
β	decay constant
β_n	decay constant per carbon atom
C	capacitance
C_g	gate capacitance
C_{DL}	double-layer capacitance
C_Σ	total capacitance
δ	Dirac's delta function, energy level spacing, and nanoparticle center-to-center core separation
D	dimensionality
D_E	electron diffusion coefficient
Δ	widths of energy bands
ΔE_{fwhm}	full-width at half-maximum of cyclic voltammograms' peaks
ΔE_p	peak separation of oxidation and reduction waves
ΔG^o	standard free energy of reaction
ΔG_a	free energy of activation
ΔN	number of states per unit volume
ΔU	charging energy
ΔW	energy bandwidth
e	electron charge
ε	permittivity
ε_0	permittivity of vacuum
ε_{op}	optical dielectric constant
ε_r	dielectric constant
ε_s	static dielectric constant
E	energy, electrochemical potential
E_a	activation energy
E_g	energy gap
E_C	charging energy
$\bar{E}_C$	average charging energy
E_F	Fermi energy
E_{PZC}	potential of zero charge
f	distribution function, Fermi−Dirac distribution, and frequency
ϕ	barrier height, phase angle, and work function
F	Faraday constant, force
g	conductance
g_0	tunneling conductance at zero bias
g_{eff}	effective conductance
g_i	insulating conductance
g_m	metallic conductance
g_t	thermally activated conductance
g_Q	quantum of conductance
Γ	electron tunneling rate, energy level broadening
h	film thickness
$\hbar$	Planck's constant
i	imaginary unit
I	current
I_{sd}	source−drain current
k	spring constant
k_B	Boltzmann's constant
k_{CT}	charge transfer rate
k_{ET}	electron transfer rate
k_{EX}	rate constant of bimolecular exchange reaction
k_{HOP}	hopping rate
κ	decay constant
l	mean free path
$\mathbf{l}$	overlapping length of electrodes
λ	outer-sphere reorganization energy
L	distance between electrodes, grain size
m	mass of electron
m^*	effective mass of electron
μ	chemical potential
n	density of conducting electrons, number of electrons involved in a reaction, and number of methylene groups
n_{sat}	number of saturated carbon−carbon bonds
υ	temperature exponent
N	number of atoms, number of finger pairs
p	filling fraction
p_c	percolation threshold
P	probability
Q	nanoparticle charge
r	distance
ρ	density of states
R	gas constant, nanoparticle radius, resistance
R_c	critical resistance
R_{ET}	electron transfer resistance
R_G	gain resistance
R_S	resistance of electrolyte solution
s	inter-NP surface-to-surface separation
σ	conductivity
σ_W	Warburg's coefficient
t	time
τ	mean free time
T	temperature
$\lvert T\rvert^2$	tunneling transmission probability
T_C	critical temperature
U	barrier height, Hubbard energy
$\bar{U}$	average barrier height
υ	scan rate
υ_F	Fermi velocity
V	voltage

$\tilde{V}$	modulation voltage
V_o	modulation amplitude
V_b	bias voltage
V_g	gate voltage
V_{gs}	gate-source potential
V_{sd}	source−drain potential
V_{CB}	Coulomb blockade threshold voltage
V_T	voltage threshold
V_{out}	output voltage
ω	modulation angular frequency
ξ	localization length
ψ	wavefunction
$\psi_H(r)$	hydrogen atom wavefunction
z	cantilever deflection, charge state, and coordination number
ζ	scaling exponent
Z	impedance
Z_{Im}	imaginary component of impedance
Z_F	Faradaic impedance
Z_{Re}	real component of impedance
Z_W	Warburg impedance

9. Acknowledgments

The authors acknowledge the Natural Science and Engineering Research Council of Canada for support. A.Z. acknowledges support through an Ontario Graduate Scholarship and a Lachlan Gilchrist Fellowship.

10. Appendix A: Tunneling through a 1D Potential Barrier

According to quantum mechanics, an electron can tunnel through a potential energy barrier whose height (V_0) is greater than the electron's energy (E). Consider, for example, the energy diagram for a 1D potential barrier shown in Figure A1, where the potential energy is equal to V_0 between $x = 0$ and $x = L$ and zero everywhere else.

Schrödinger's equation for such a system is

$$\begin{cases} -\frac{\hbar^2}{2m}\frac{d^2\psi(x)}{dx^2} + V_0\psi(x) = E\psi(x) & 0 \le x \le L, \\ -\frac{\hbar^2}{2m}\frac{d^2\psi(x)}{dx^2} = E\psi(x) & \text{otherwise} \end{cases} \tag{A1}$$

where m is the mass of electron and $\hbar$ is Planck's constant. By solving eq A1, we find electronic wave functions (ψ) in regions I, II, and III:

$$\psi_I(x) = A\,e^{i\alpha x} + B\,e^{-i\alpha x} \tag{A2}$$

$$\psi_{II}(x) = C\,e^{\kappa x} + D\,e^{-\kappa x} \tag{A3}$$

$$\psi_{III}(x) = F\,e^{i\alpha x} \tag{A4}$$

where

$$\alpha = \sqrt{2mE}/\hbar \tag{A5}$$

$$\kappa = \sqrt{2m(V_0 - E)}/\hbar \tag{A6}$$

and A, B, C, D, and F are constants. In the above equations, the terms $A\,e^{i\alpha x}$, $B\,e^{-i\alpha x}$, and $F\,e^{i\alpha x}$ represent incident, reflected, and transmitted parts of the wave function, and note that $C\,e^{\kappa x}$ and $D\,e^{-\kappa x}$ correspond to growing and decaying exponential components of the wave function inside the barrier, respectively.

To find the constants A, B, C, and D relative to A_0, we apply the following boundary conditions:

$$\psi_I(0) = \psi_{II}(0), \quad \psi_{II}(L) = \psi_{III}(L), \quad \left.\frac{d\psi_I}{dx}\right|_{x=0} = \left.\frac{d\psi_{II}}{dx}\right|_{x=0}, \quad \left.\frac{d\psi_{II}}{dx}\right|_{x=L} = \left.\frac{d\psi_{III}}{dx}\right|_{x=L} \tag{A7}$$

Resulting equations are as follows:

$$A + B = C + D \tag{A8}$$

$$i\alpha A - i\alpha B = \kappa C - \kappa D \tag{A9}$$

$$C\,e^{\kappa L} + D\,e^{-\kappa L} = F\,e^{i\alpha L} \tag{A10}$$

$$\kappa C\,e^{\kappa L} - \kappa D\,e^{-\kappa L} = i\alpha F\,e^{i\alpha L} \tag{A11}$$

The transmission probability through the barrier, $|T|^2$, is then calculated by

$$|T|^2 = \left|\frac{F}{A}\right|^2 = \left|\frac{4i\alpha\kappa\,e^{-i\alpha L}}{(i\alpha+\kappa)^2 e^{-\kappa L} - (i\alpha-\kappa)^2 e^{\kappa L}}\right|^2 \tag{A12}$$

The expression for $|T|^2$ can be simplified using a thick-barrier approximation, in which $\kappa L \gg 1$. The result is

$$|T|^2 \approx \left|\frac{4i\alpha\kappa\,e^{-i\alpha L}}{(i\alpha-\kappa)^2\,e^{\kappa L}}\right|^2 = \frac{16\alpha^2\kappa^2}{(\alpha^2+\kappa^2)^2}\,e^{-2\kappa L} = 16\left(\frac{E}{V_0}\right)\left(1-\frac{E}{V_0}\right)e^{-2\kappa L} \tag{A13}$$

The pre-exponential factor is typically in the order of ~1, and therefore, the exponential factor is the most significant:

$$|T|^2 \approx e^{-2\kappa L} \tag{A14}$$

The transmission probability decays exponentially with the barrier width, and the decay constant, κ, depends on the barrier height as described by eq A6.

In the thick-barrier approximation, the growing exponential term in the expression of Ψ_{II} (eq A3) can be neglected since, from the boundary conditions (eqs A10 and A11), one can obtain

$$\left|\frac{C}{D}\right|^2 = e^{-4\kappa L} \tag{A15}$$

In the limit of $\kappa L \gg 1$, the probability of the growing exponential term, $|C|^2$, becomes much smaller than that of

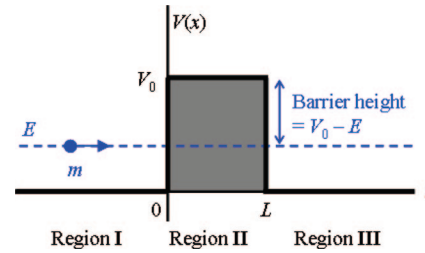

Figure A1. Energy diagram of a 1D square potential barrier.

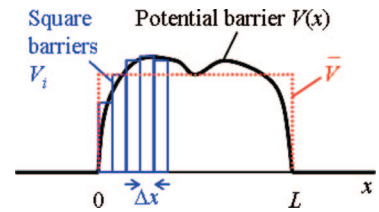

Figure A2. Arbitrary potential barrier approximated by a series of square barriers with widths of Δx.

the decaying exponential term, $|D|^2$. Therefore, the wave function in the barrier region decays exponentially with distance:

$$\psi_{II}(x) \approx e^{-\kappa x} \tag{A16}$$

with a decay constant equal to κ.

The above equations can be extended to describe a barrier potential with a slowly varying arbitrary shape using the WKB approximation. For a barrier with the potential profile of $V(x)$, the tunneling transmission can be approximated by

$$|T|^2 \approx \exp\left(-\frac{2}{\hbar}\int_0^L \sqrt{2m(V(x)-E)}\,dx\right) \tag{A17}$$

Equation A17 can be rationalized as follows. The potential barrier can be considered as a series of square barriers with widths of Δx where the ith square barrier has a height of V_i (Figure A2). The probability of transmission trough the barrier $V(x)$ then can be written as a product of the probabilities of tunneling through the square barriers:

$$|T|^2 \approx \prod_i \exp\left(-\frac{2\sqrt{2m(V_i-E)}\Delta x}{\hbar}\right) = \exp\left(-\sum_i \frac{2\sqrt{2m(V_i-E)}\Delta x}{\hbar}\right) \tag{A18}$$

Substituting the sum in the above equation by an integral in the limit of $\Delta x \to 0$, we get the WKB approximation. In tha average barrier height approximation, eq A17 is simplified by replacing the potential barrier $V(x)$ with a constant average potential $\bar{V}$:

$$|T|^2 \approx \exp\left(-\frac{2\sqrt{2m(\bar{V}-E)}L}{\hbar}\right) = e^{-2\bar{\kappa}L} \tag{A19}$$

where

$$\bar{\kappa} = \sqrt{2m(\bar{V}-E)}/\hbar \tag{A20}$$

11. Appendix B: Tunneling Current at Intermediate Bias

Here, we derive an expression for tunneling current taking into account the voltage dependence of the barrier height. We assume that $eV_b \ll \phi$, so that electron transport is dominated by tunneling. The tunneling transmission according to the WKB approximation (eq A17) is then given by

$$\begin{aligned}\ln|T|^2 &\approx -\frac{2}{\hbar}\int_0^L \sqrt{2m(\phi + E_F - E - eV_b x/L)}\,dx \\ &= -\frac{2\sqrt{2m\phi}}{\hbar}\int_0^L \left(1 + \frac{E_F - E}{\phi} - \frac{eV_b x}{\phi L}\right)^{1/2} dx \\ &\approx -\frac{2\sqrt{2m\phi}}{\hbar}\int_0^L \left(1 + \frac{E_F - E}{2\phi} - \frac{eV_b x}{2\phi L}\right) dx \\ &= -\frac{2\sqrt{2m\phi}}{\hbar}\left(1 + \frac{E_F - E}{2\phi} - \frac{eV_b}{4\phi}\right)L \\ &= -2\kappa_0 L + (E - E_F)/\xi + eV_b/2\xi \end{aligned} \tag{B1}$$

where

$$\kappa_0 = \sqrt{2m\varphi}/\hbar \tag{B2}$$

$$\xi = \varphi/\kappa_0 L \tag{B3}$$

Substituting eq B1 into the expression for tunneling current (eq 21), we find

$$I \approx \frac{4\pi e}{\hbar}\rho(E_F)^2\, e^{-2\kappa_0 L}\, e^{eV_b/2\xi}\int_0^{+\infty} e^{(E-E_F)/\xi}\left[\frac{1}{1+e^{(E-E_F)/kT}} - \frac{1}{1+e^{(E-E_F+eV_b)/kT}}\right] dE \tag{B4}$$

By introducing an integration variable $y = \exp[(E - E_F)/kT]$ and taking $\exp(-E_F/kT) \approx 0$ in the lower limit of the integral after exchanging variables, we get

$$I \approx \frac{4\pi e}{\hbar}\rho(E_F)^2\, e^{-2\kappa_0 L}\, e^{eV_b/2\xi}\int_0^{+\infty} y^{kT/\xi}\left[\frac{1}{1+y} - \frac{1}{1+ye^{eV_b/kT}}\right]\frac{kT}{y}\,dy \tag{B5}$$

The above integral can be solved analytically using the following relationship:

$$\int_0^{+\infty} \frac{y^{a-1}}{1+by}\,dy = \frac{\pi b^{-a}}{\sin(\pi a)} \quad (a<1) \tag{B6}$$

Thus, we obtain

$$\begin{aligned} I &\approx \frac{4\pi e}{\hbar}\rho(E_F)^2\, e^{-2\kappa_0 L}\, e^{eV_b/2\xi}\frac{\pi kT}{\sin(\pi kT/\xi)}[1 - e^{-eV_b/\xi}] \\ &= \frac{8\pi e\xi}{\hbar}\rho(E_F)^2\, e^{-2\kappa_0 L}\frac{\pi kT/\xi}{\sin(\pi kT/\xi)}\sinh(eV_b/2\xi) \end{aligned} \tag{B7}$$

$\pi kT/\xi$ is typically a small quantity. Its value for Au ($\phi \approx$ 5.1 eV) at room temperature is ~0.18. Therefore, $(\pi kT/\xi)/\sin(\pi kT/\xi)$ is approximately a constant equal to ~1. The tunneling current then can be written as

$$I \approx \frac{8\pi e\xi}{\hbar}\rho(E_F)^2\, e^{-2\kappa_0 L}\sinh\frac{eV_b}{2\xi} \tag{B8}$$

12. Appendix C: Some Useful Integrations

The integral in eq 22 can be solved analytically. By introducing an integration variable, $y = \exp[(E - E_F)/k_BT]$, and taking $\exp(-E_F/k_BT) \approx 0$ in the lower limit of the integral after exchanging variables, we get

$$\begin{aligned}\int_0^{+\infty}[f(E) - f(E+eV_b)]\,dE &= \int_0^{+\infty}\left[\frac{1}{1+e^{(E-E_F)/k_BT}} - \frac{1}{1+e^{(E+eV_b-E_F)/k_BT}}\right]dE \\ &\approx k_BT\int_0^{+\infty}\left[\frac{1}{1+y} - \frac{1}{1+e^{eV_b/k_BT}y}\right]\frac{dy}{y} \\ &= k_BT(e^{eV_b/k_BT} - 1)\int_0^{+\infty}\frac{dy}{(1+y)(1+e^{eV_b/k_BT}y)} \\ &= k_BT(e^{eV_b/k_BT} - 1)\frac{eV_b/k_BT}{e^{eV_b/k_BT} - 1} \\ &= eV_b \end{aligned} \tag{C1}$$

The integral in eq 36 can be solved similarly:

$$\int_0^{+\infty} f(E)[1-f(E-\Delta E_j^{\pm})]\,\mathrm{d}E = \int_0^{+\infty} \frac{1}{1+\mathrm{e}^{(E-E_\mathrm{F})/k_\mathrm{B}T}}\left[1-\frac{1}{1+\exp[(E-\Delta E_j^{\pm}-E_\mathrm{F})/k_\mathrm{B}T]}\right]\mathrm{d}E$$
$$\approx k_\mathrm{B}T\int_0^{+\infty}\frac{1}{1+y}\left[1-\frac{1}{1+y\exp(-\Delta E_j^{\pm}/k_\mathrm{B}T)}\right]\frac{\mathrm{d}y}{y}$$
$$= k_\mathrm{B}T\,\mathrm{e}^{-\Delta E_j^{\pm}/k_\mathrm{B}T}\int_0^{+\infty}\frac{\mathrm{d}y}{(1+y)[1+y\exp(-\Delta E_j^{\pm}/k_\mathrm{B}T)]}$$
$$= k_\mathrm{B}T\,\mathrm{e}^{-\Delta E_j^{\pm}/k_\mathrm{B}T}\frac{-\Delta E_j^{\pm}/k_\mathrm{B}T}{\exp(-\Delta E_j^{\pm}/k_\mathrm{B}T)-1} = \frac{-\Delta E_j^{\pm}}{1-\exp(\Delta E_j^{\pm}/k_\mathrm{B}T)} \quad \text{(C2)}$$

13. Appendix D: Zero-Bias Conductance of a Symmetric Double-Junction System

Zero-bias conductance of a symmetric double-junction system can be obtained by

$$g(0\,\mathrm{V}) = e\left(\frac{\partial\Gamma_1^{+}}{\partial V_\mathrm{b}}(0\,\mathrm{V})-\frac{\partial\Gamma_1^{-}}{\partial V_\mathrm{b}}(0\,\mathrm{V})\right) \quad \text{(D1)}$$

The tunneling rate $\Gamma_1^{\pm}$ (eq 39) at $0 < k_\mathrm{B}T \ll \Delta E_1^{\pm}$ can be written as follows:

$$\Gamma_1^{\pm} \approx \frac{\Delta E_1^{\pm}}{e^2R}\,\mathrm{e}^{-\Delta E_1^{\pm}/k_\mathrm{B}T} = -\frac{k_\mathrm{B}T(-u\pm v)}{e^2R}\,\mathrm{e}^{-u\pm v} \quad \text{(D2)}$$

where $u \equiv E_\mathrm{C}/k_\mathrm{B}T$ and $v \equiv eV_\mathrm{b}/2k_\mathrm{B}T$. The derivative of $\Gamma_1^{\pm}$ with respect to V_b then is given by

$$\frac{\partial\Gamma_1^{\pm}}{\partial V_\mathrm{b}} = \frac{\partial\Gamma_1^{\pm}}{\partial v}\frac{\partial v}{\partial V_\mathrm{b}} \approx -\frac{1}{2eR}[\pm\mathrm{e}^{-u\pm v}\pm(-u\pm v)\mathrm{e}^{-u\pm v}] \quad \text{(D3)}$$

The zero-bias conductance then becomes

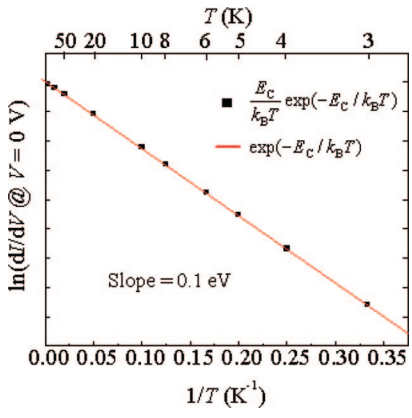

Figure D1. ln[g(0 V)] vs $1/T$ for $E_\mathrm{C} = 0.1$ eV. The black dots and the red solid line are produced using eqs D4 and D5, respectively.

$$g(0\,\mathrm{V}) \approx -\frac{1}{2R}[(\mathrm{e}^{-u}-u\mathrm{e}^{-u})-(-\mathrm{e}^{-u}+u\mathrm{e}^{-u})] = -\frac{1}{R}(1-u)\mathrm{e}^{-u} = -\frac{1}{R}\left(1-\frac{E_\mathrm{C}}{k_\mathrm{B}T}\right)\mathrm{e}^{-\frac{E_\mathrm{C}}{k_\mathrm{B}T}} \approx \frac{1}{R}\frac{E_\mathrm{C}}{k_\mathrm{B}T}\mathrm{e}^{-\frac{E_\mathrm{C}}{k_\mathrm{B}T}} \quad \text{(D4)}$$

The pre-exponential factor $E_\mathrm{C}/k_\mathrm{B}T$ varies more slowly with T than the exponential term. Therefore, we get

$$g(0\,\mathrm{V}) \approx \exp\left(-\frac{E_\mathrm{C}}{k_\mathrm{B}T}\right) \quad \text{(D5)}$$

Figure D1 shows plots of ln[g(0 V)] vs $1/T$ according to eqs D4 and D5.

14. References

(1) Kastner, M. A. *Phys. Today* **1993**, *46*, 24.
(2) Halperin, W. P. *Rev. Mod. Phys.* **1986**, *58*, 533.
(3) Ralph, D. C.; Black, C. T.; Tinkham, M. *Phys. Rev. Lett.* **1995**, *74*, 3241.
(4) Alivisatos, A. P. *Science* **1996**, *271*, 933.
(5) Burda, C.; Chen, X.; Narayanan, R.; El-Sayed, M. A. *Chem. Rev.* **2005**, *105*, 1025.
(6) van Staveren, M. P. J.; Brom, H. B.; de Jongh, L. J. *Phys. Rep.* **1991**, *208*, 1.
(7) Ralph, D. C.; Black, C. T.; Tinkham, M. *Phys. Rev. Lett.* **1997**, *78*, 4087.
(8) Ralph, D. C.; Guéron, S.; Black, C. T.; Tinkham, M. *Physica B* **2000**, *280*, 420.
(9) Dunford, J. L. M.Sc. Thesis, Department of Chemistry, University of Toronto, Toronto, Canada, 2003.
(10) Bose, S.; Raychaudhuri, P.; Banerjee, R.; Vasa, P.; Ayyub, P. *Phys. Rev. Lett.* **2005**, *95*, 147003.
(11) Weitz, I. S.; Sample, J. L.; Ries, R.; Spain, E. M.; Heath, J. R. *J. Phys. Chem. B* **2000**, *104*, 4288.
(12) Suganuma, Y.; Dhirani, A.-A. *J. Phys. Chem. B* **2005**, *109*, 15391.
(13) Suganuma, Y.; Trudeau, P.-E.; Dhirani, A.-A. *Nanotechnology* **2005**, *16*, 1196.
(14) Shipway, A. N.; Willner, I. *Chem. Commun.* **2001**, 2305.
(15) Hernández-Santos, D.; González-García, M. B.; García, A. C. *Electroanalysis* **2002**, *14*, 1225.
(16) Katz, E.; Willner, I.; Wang, J. *Electroanalysis* **2004**, *16*, 19.
(17) Katz, E.; Willner, I. *Angew. Chem., Int. Ed.* **2004**, *43*, 6042.
(18) Parak, W. J.; Gerion, D.; Pellegrino, T.; Zanchet, D.; Micheel, C.; Williams, S. C.; Boudreau, R.; Le Gros, M. A.; Larabell, C. A.; Alivisatos, A. P. *Nanotechnology* **2003**, *14*, R15.
(19) Alivisatos, P. *Nat. Biotechnol.* **2004**, *22*, 47.
(20) Rosi, N. L.; Mirkin, C. A. *Chem. Rev.* **2005**, *105*, 1547.
(21) Haick, H. *J. Phys. D: Appl. Phys.* **2007**, *40*, 7173.
(22) Freeman, R. G.; Grabar, K. C.; Allison, K. J.; Bright, R. M.; Davis, J. A.; Guthrie, A. P.; Hommer, M. B.; Jackson, M. A.; Smith, P. C.; Walter, D. G.; Natan, M. J. *Science* **1995**, *267*, 1629.
(23) Goebbert, C.; Nonninger, R.; Aegerter, M. A.; Schmidt, H. *Thin Solid Films* **1999**, *351*, 79.
(24) Schmid, G.; Corain, B. *Eur. J. Inorg. Chem.* **2003**, 3081.
(25) Steigerwald, M. L.; Brus, L. E. *Annu. Rev. Mater. Sci.* **1989**, *19*, 471.
(26) Schmid, G. *Chem. Rev.* **1992**, *92*, 1709.
(27) Whetten, R. L.; Shafigullin, M. N.; Khoury, J. T.; Schaaff, T. G.; Vezmar, I.; Alvarez, M. M.; Wilkinson, A. *Acc. Chem. Res.* **1999**, *32*, 397.
(28) Murray, C. B.; Kagan, C. R.; Bawendi, M. G. *Annu. Rev. Mater. Sci.* **2000**, *30*, 545.
(29) Trindade, T.; O'Brien, P.; Pickett, N. L. *Chem. Mater.* **2001**, *13*, 3843.
(30) Moriarty, P. *Rep. Prog. Phys.* **2001**, *64*, 297.
(31) Crooks, R. M.; Zhao, M.; Sun, L.; Chechik, V.; Yeung, L. K. *Acc. Chem. Res.* **2001**, *34*, 181.
(32) Zhong, Z.; Male, K. B.; Luong, J. H. T. *Anal. Lett.* **2003**, *36*, 3097.
(33) Masala, O.; Seshadri, R. *Annu. Rev. Mater. Res.* **2004**, *34*, 41.
(34) Bawendi, M. G.; Stiegerwald, M. L.; Brus, L. E. *Annu. Rev. Phys. Chem.* **1998**, *49*, 371.
(35) Link, S.; El-Sayed, M. A. *Int. Rev. Phys. Chem.* **2000**, *19*, 409.
(36) Hodak, J. K.; Henglein, A.; Hartland, G. V. *J. Chem. Phys. B* **2000**, *104*, 9954.
(37) Efros, A. L.; Rosen, M. *Annu. Rev. Mater. Sci.* **2000**, *30*, 475.
(38) Yoffe, A. D. *Adv. Phys.* **2001**, *50*, 1.
(39) Kamat, P. V. *J. Phys. Chem. B* **2002**, *106*, 7729.

(40) Link, S.; El-Sayed, M. A. *Annu. Rev. Phys. Chem.* **2003**, *54*, 331.
(41) Thomas, K. G.; Kamat, P. V. *Acc. Chem. Res.* **2003**, *36*, 888.
(42) Ghosh, S. K.; Tarasankar, P. *Chem. Rev.* **2007**, *107*, 4797.
(43) Tolbert, S. H.; Alivisatos, A. P. *Annu. Rev. Phys. Chem.* **1995**, *46*, 595.
(44) Daniel, M.-C.; Astruc, D. *Chem. Rev.* **2004**, *104*, 293.
(45) Fendler, J. H.; Meldrum, F. C. *Adv. Mater.* **1995**, *7*, 607.
(46) Fendler, J. H. *Chem. Mater.* **1996**, *8*, 1616.
(47) Collier, C. P.; Vossmeyer, T.; Heath, J. R. *Annu. Rev. Phys. Chem.* **1998**, *49*, 371.
(48) Wang, Z. L. *Adv. Mater.* **1998**, *10*, 13.
(49) Shipway, A. N.; Katz, E.; Willner, I. *Chem. Phys. Chem.* **2000**, *1*, 18.
(50) Rao, C. N. R.; Kulkarni, G. U.; Thomas, P. J.; Edwards, P. P. *Chem. Soc. Rev.* **2000**, *29*, 27.
(51) Chakraborty, A. K.; Golumbfskie, A. J. *Annu. Rev. Phys. Chem.* **2001**, *52*, 537.
(52) Pileni, M. P. *J. Phys. Chem. B* **2001**, *105*, 3358.
(53) Brust, M.; Kiely, C. J. *Colloids Surf., A* **2002**, *202*, 175.
(54) Liz-Marzan, L. M.; Mulvaney, P. *J. Phys. Chem. B* **2003**, *107*, 7312.
(55) Schmid, G.; Simon, U. *Chem. Commun.* **2005**, 697.
(56) Crespo-Biel, O.; Ravoo, B. J.; Reinhoudt, D. N.; Huskens, J. *J. Mater. Chem.* **2006**, *16*, 3997.
(57) Adams, D. M.; Brus, L.; Chidsey, C. E. D.; Creager, S.; Creutz, C.; Kagan, C. R.; Kamat, P. V.; Lieberman, M.; Lindsay, S.; Marcus, R. A.; Metzger, R. M.; Michel-Beyerle, M. E.; Miller, J. R.; Newton, M. D.; Rolison, D. R.; Sankey, O.; Schanze, K. S.; Yardley, J.; Zhu, X. *J. Phys. Chem. B* **2003**, *107*, 6668.
(58) Turkevich, J.; Stevenson, P. C.; Hillier, J. *Discuss. Faraday Soc.* **1951**, *11*, 55.
(59) Slot, J. W.; Geuze, H. J. *Eur. J. Cell Bio.* **1985**, *38*, 87.
(60) Brust, M.; Walker, M.; Bethell, D.; Schiffrin, D. J.; Whyman, R. *J. Chem. Soc., Chem. Commun.* **1994**, *7*, 801.
(61) Brust, M.; Schiffrin, D. J.; Bethell, D.; Kiely, C. J. *Adv. Mater.* **1995**, *7*, 795.
(62) Murray, C. B.; Sun, S.; Doyle, H.; Betley, T. *MRS Bull.* **2001**, *26*, 985.
(63) Murray, C. B.; Norris, D. J.; Bawendi, M. G. *J. Am. Chem. Soc.* **1993**, *115*, 8706.
(64) Whetten, R. L.; Khoury, J. T.; Alvarez, M. M.; Murthy, S.; Vezmar, I.; Wang, Z. L.; Stephens, P. W.; Cleveland, C. L.; Luedtke, W. D.; Landman, U. *Adv. Mater.* **1996**, *8*, 428.
(65) Devenish, R. W.; Goulding, T.; Heaton, B. T.; Whyman, R. *J. Chem. Soc., Dalton Trans.* **1996**, 673.
(66) Zhong, C. J.; Zhang, W. X.; Leibowitz, F. L.; Eichelberger, H. H. *Chem. Commun.* **1999**, 1211.
(67) Maye, M. M.; Zheng, W.; Leibowitz, F. L.; Ly, N. K.; Zhong, C. J. *Langmuir* **2000**, *16*, 490.
(68) Schaaff, T. G.; Whetten, R. L. *J. Phys. Chem. B* **1999**, *103*, 9394.
(69) Wilcoxon, J. P.; Martin, J. E.; Parsapour, F.; Wiedenman, B.; Kelley, D. F. *J. Chem. Phys.* **1998**, *108*, 9137.
(70) Hicks, J. F.; Miles, D. T.; Murray, R. W. *J. Am. Chem. Soc.* **2002**, *124*, 13322.
(71) Wei, G.; Liu, F.; Wang, C. R. C. *Anal. Chem.* **1999**, *71*, 2085.
(72) Wilcoxon, J. P.; Martin, J. E.; Provencio, P. *Langmuir* **2000**, *16*, 9912.
(73) Schnabel, U.; Fischer, C.; Kenndler, E. *J. Microcolumn Sep.* **1997**, *9*, 529.
(74) Templeton, A. C.; Cliffel, D. E.; Murray, R. W. *J. Am. Chem. Soc.* **1999**, *121*, 7081.
(75) Bos, W.; Steggerda, J. J.; Yan, S.; Casalnuovo, J. A.; Mueting, A. M.; Pignolet, L. H. *Inorg. Chem.* **1988**, *27*, 948.
(76) Jimenez, V. L.; Leopold, M. C.; Mazzitelli, C.; Jorgenson, J. W.; Murray, R. W. *Anal. Chem.* **2003**, *75*, 199.
(77) Hostetler, M. J.; Green, S. J.; Stokes, J. J.; Murray, R. W. *J. Am. Chem. Soc.* **1996**, *118*, 4212.
(78) Hostetler, M. J.; Templeton, A. C.; Murray, R. W. *Langmuir* **1999**, *15*, 3782.
(79) Kuno, M.; Lee, J. K.; Dabbousi, B. O.; Mikulec, F. V.; Bawendi, M. G. *J. Chem. Phys.* **1997**, *106*, 9869.
(80) Shenhar, R.; Rotello, V. M. *Acc. Chem. Res.* **2003**, *36*, 549.
(81) Hostetler, M. J.; Wingate, J. E.; Zhong, C. J.; Harris, J. E.; Vachet, R. W.; Clark, M. R.; Londono, J. D.; Green, S. J.; Stokes, J. J.; Wignall, G. D.; Glish, G. L.; Porter, M. D.; Evans, N. D.; Murray, R. W. *Langmuir* **1998**, *14*, 17.
(82) Templeton, A. C.; Wuelfing, M. P.; Murray, R. W. *Acc. Chem. Res.* **2000**, *33*, 27.
(83) Love, J. C.; Estroff, L. A.; Kriebel, J. K.; Nuzzo, R. G.; Whitesides, G. M. *Chem. Rev.* **2005**, *105*, 1103.
(84) Tian, S.; Liu, J.; Zhu, T.; Knoll, W. *Chem. Mater.* **2004**, *16*, 4103.
(85) Sih, B. C.; Wolf, M. O. *Chem. Commun.* **2005**, 3375.
(86) Taniguchi, S.; Minamoto, M.; Matsushita, M. M.; Sugawara, T.; Kawada, Y.; Bethel, D. *J. Mater. Chem.* **2006**, *16*, 3459.
(87) Mirkin, C. A.; Letsinger, R. L.; Mucic, R. C.; Storhoff, J. J. *Nature* **1996**, *382*, 607.
(88) Park, S.-J.; Lazarides, A. A.; Mirkin, C. A.; Brazis, P. W.; Kannewurf, C. R.; Letsinger, R. L. *Angew. Chem., Int. Ed.* **2000**, *39*, 3845.
(89) Koplin, E.; Niemeyer, C. M.; Simon, U. *J. Mater. Chem.* **2006**, *16*, 1338.
(90) Liu, Y.; Wang, Y.; Claus, R. O. *Chem. Phys. Lett.* **1998**, *298*, 315.
(91) Ferreyra, N.; Coche-Guérente, L.; Fatisson, J.; Teijelo, M. L.; Labbé, P. *Chem. Commun.* **2003**, 2056.
(92) Kakkassery, J. J.; Abid, J.-P.; Carrara, M.; Fermín, D. J. *Faraday Discuss.* **2004**, *125*, 157.
(93) Chirea, M.; Garcia-Morales, V.; Manzanares, J. A.; Pereira, C.; Gulaboski, R.; Silva, F. *J. Phys. Chem. B* **2005**, *109*, 21808.
(94) Zhao, J.; Bradbury, C. R.; Huclova, S.; Potapova, I.; Carrara, M.; Fermín, D. J. *J. Phys. Chem. B* **2005**, *109*, 22985.
(95) Doron, A.; Katz, E.; Willner, I. *Langmuir* **1995**, *11*, 1313.
(96) Blonder, R.; Sheeney, L.; Willner, I. *Chem. Commun.* **1998**, 1393.
(97) Gittins, D. I.; Bethell, D.; Nichols, R. J.; Schiffrin, D. J. *Adv. Mater.* **1999**, *11*, 737.
(98) Gittins, D. I.; Bethell, D.; Nichols, R. J.; Schiffrin, D. J. *J. Mater. Chem.* **2000**, *10*, 79.
(99) Chen, S. *Langmuir* **2001**, *17*, 6664.
(100) Uosaki, K.; Kondo, T.; Okamura, M.; Song, W. *Faraday Discuss.* **2002**, *121*, 373.
(101) Song, W.; Okamura, M.; Kondo, T.; Uosaki, K. *J. Electroanal. Chem.* **2003**, *554*, 385.
(102) Song, W.; Okamura, M.; Kondo, T.; Uosaki, K. *Phys. Chem. Chem. Phys.* **2003**, *5*, 5279.
(103) Escorcia, A.; Dhirani, A.-A. *J. Electroanal. Chem.* **2007**, *601*, 260.
(104) Labande, A.; Astruc, D. *Chem. Commun.* **2000**, 1007.
(105) Daniel, M.-C.; Ruiz, J.; Nlate, S.; Palumbo, J.; Blais, J.-C.; Astruc, D. *Chem. Commun.* **2001**, 2000.
(106) Labande, A.; Ruiz, J.; Astruc, D. *J. Am. Chem. Soc.* **2002**, *124*, 1782.
(107) Daniel, M.-C.; Ruiz, J.; Nlate, S.; Blais, J.-C.; Astruc, D. *J. Am. Chem. Soc.* **2003**, *125*, 2617.
(108) Vossmeyer, T.; Guse, B.; Besnard, I.; Bauer, R. E.; Müllen, K.; Yasuda, A. *Adv. Mater.* **2002**, *14*, 238.
(109) Krasteva, N.; Besnard, I.; Guse, B.; Bauer, R. E.; Müllen, K.; Yasuda, A.; Vossmeyer, T. *Nano Lett.* **2002**, *2*, 551.
(110) Krasteva, N.; Guse, B.; Besnard, I.; Yasuda, A.; Vossmeyer, T. *Sens. Actuators, B* **2003**, *92*, 137.
(111) Joseph, Y.; Krasteva, N.; Besnard, I.; Guse, B.; Rosenberger, M.; Wild, U.; Knop-Gericke, A.; Schlögl, R.; Krustev, R.; Yasuda, A.; Vossmeyer, T. *Faraday Discuss.* **2004**, *125*, 77.
(112) Lahav, M.; Shipway, A. N.; Willner, I. *J. Chem. Soc., Perkin Trans.* **1999**, *2*, 1925.
(113) Lahav, M.; Gabai, R.; Shipway, A. N.; Willner, I. *Chem. Commun.* **1999**, 1937.
(114) Lahav, M.; Shipway, A. N.; Willner, I.; Nielsen, M. B.; Stoddart, J. F. *J. Electroanal. Chem.* **2000**, *482*, 217.
(115) Shipway, A. N.; Lahav, M.; Willner, I. *Adv. Mater.* **2000**, *12*, 993.
(116) Andres, R. P.; Bielefeld, J. D.; Henderson, J. I.; Janes, D. B.; Kolagunta, V. R.; Kubiak, C. P.; Mahoney, W. J.; Osifchin, R. G. *Science* **1996**, *273*, 1690.
(117) Korgel, B. A.; Fullam, S.; Connolly, S.; Fitzmaurice, D. *J. Phys. Chem. B* **1998**, *102*, 8379.
(118) Korgel, B. A.; Fitzmaurice, D. *Phys. Rev. B* **1999**, *59*, 14191.
(119) Lin, X. M.; Jaeger, H. M.; Sorensen, C. M.; Klabunde, K. J. *J. Phys. Chem. B* **2001**, *105*, 3353.
(120) Narayanan, S.; Wang, J.; Lin, X.-M. *Phys. Rev. Lett.* **2004**, *93*, 135503.
(121) Bigioni, T. P.; Lin, X.-M.; Nguyen, T. T.; Corwin, E. I.; Witten, T. A.; Jaeger, H. M. *Nat. Mater.* **2006**, *5*, 265.
(122) Terrill, R. H.; Postlethwaite, T. A.; Chen, C.; Poon, C.; Terzis, A.; Chen, A.; Hutchison, J. E.; Clark, M. R.; Wignall, G.; Londono, J. D.; Superfine, R.; Falvo, M., Jr.; Samulski, E. T.; Murray, R. W. *J. Am. Chem. Soc.* **1995**, *117*, 12537.
(123) Wuelfing, W. P.; Green, S. J.; Pietron, J. J.; Cliffel, D. E.; Murray, R. W. *J. Am. Chem. Soc.* **2000**, *122*, 11465.
(124) Beecher, P.; Quinn, A. J.; Shevchenko, E. V.; Weller, H.; Redmond, G. *J. Phys. Chem. B* **2004**, *108*, 9564.
(125) Beecher, P.; Quinn, A. J.; Shevchenko, E. V.; Weller, H.; Redmond, G. *Nano Lett.* **2004**, *4*, 1289.
(126) Quinn, A. J.; Beecher, P.; Iacopino, D.; Floyd, L.; De Marzi, G.; Shevchenko, E. V.; Weller, H.; Redmond, G. *Small* **2005**, *1*, 613.
(127) Quinn, A. J.; Redmond, G. *Prog. Solid State Chem.* **2005**, *33*, 263.
(128) Shevchenko, E. V.; Talapin, D. V.; Rogach, A. L.; Kornowski, A.; Haase, M.; Weller, H. *J. Am. Chem. Soc.* **2002**, *124*, 11480.
(129) Black, C. T.; Murray, C. B.; Sandstorm, R. L.; Sun, S. *Science* **2000**, *290*, 1131.
(130) Drndiæ, M.; Jarosz, M. V.; Morgan, M. Y.; Kastner, M. A.; Bawendi, M. G. *J. Appl. Phys.* **2002**, *92*, 7498.

(131) Yu, D.; Wang, C.; Wehrenberg, B. L.; Guyot-Sionnest, P. *Phys. Rev. Lett.* **2004**, *92*, 216802.
(132) Wehrenberg, B. L.; Yu, D.; Ma, J.; Guyot-Sionnest, P. *J. Phys. Chem. B* **2005**, *109*, 20192.
(133) Romero, H. E.; Drndic, M. *Phys. Rev. Lett.* **2005**, *95*, 156801.
(134) Heath, J. R.; Knobler, C. M.; Leff, D. V. *J. Phys. Chem. B* **1997**, *101*, 189.
(135) Chen, S. *Anal. Chim. Acta* **2003**, *496*, 29.
(136) Bourgoin, J.-P.; Kergueris, C.; Lefèver, E.; Palacin, S. *Thin Solid Films* **1998**, *327*, 515.
(137) Markovich, G.; Collier, C. P.; Heath, J. R. *Phys. Rev. Lett.* **1998**, *80*, 3807.
(138) Medeiros-Ribeiro, G.; Ohlberg, D. A. A.; Williams, R. S.; Heath, J. R. *Phys. Rev. B* **1999**, *59*, 1633.
(139) Kim, S.-H.; Medeiros-Ribeiro, G.; Ohlberg, D.; Stanley Williams, R.; Heath, J. R. *J. Phys. Chem. B* **1999**, *103*, 10341.
(140) Sampaio, J. F.; Beverly, K. C.; Heath, J. R. *J. Phys. Chem. B* **2001**, *105*, 8797.
(141) Beverly, K. C.; Sampaio, J. F.; Heath, J. R. *J. Phys. Chem. B* **2002**, *106*, 2131.
(142) Liljeroth, P.; Vanmaekelbergh, D.; Ruiz, V.; Kontturi, K.; Jiang, H.; Kauppinen, E.; Quinn, B. M. *J. Am. Chem. Soc.* **2004**, *126*, 7126.
(143) Xia, Y.; Rogers, J. A.; Paul, K. E.; Whitesides, G. M. *Chem. Rev.* **1999**, *99*, 1823.
(144) Gates, B. D.; Xu, Q. B.; Stewart, M.; Ryan, D.; Willson, C. G.; Whitesides, G. M. *Chem. Rev.* **2005**, *105*, 1171.
(145) Santhanam, V.; Liu, J.; Agarwal, R.; Andres, R. P. *Langmuir* **2003**, *19*, 7881.
(146) Santhanam, V.; Andres, R. P. *Nano Lett.* **2004**, *4*, 41.
(147) Liao, J.; Bernard, L.; Langer, M.; Schönenberger, C.; Calame, M. *Adv. Mater.* **2006**, *18*, 2444.
(148) Guo, Q.; Teng, X.; Rahman, S.; Yang, H. *J. Am. Chem. Soc.* **2003**, *125*, 630.
(149) Park, J.-I.; Lee, W.-R.; Bae, S.-S.; Kim, Y. J.; Yoo, K.-H.; Cheon, J.; Kim, S. *J. Chem. Phys. B* **2005**, *109*, 13119.
(150) Müller, K.-H.; Herrmann, J.; Raguse, B.; Baxter, G.; Reda, T. *Phys. Rev. B* **2002**, *66*, 075417.
(151) Müller, K.-H.; Wei, G.; Raguse, B.; Myers, J. *Phys. Rev. B* **2003**, *68*, 155407.
(152) Leibowitz, F. L.; Zheng, W.; Maye, M. M.; Zhong, C.-J. *Anal. Chem.* **1999**, *71*, 5076.
(153) Decher, G. *Science* **1997**, *277*, 1232.
(154) Ariga, K.; Hill, J. P.; Ji, Q. *Phys. Chem. Chem. Phys.* **2007**, *9*, 2319.
(155) Bethell, D.; Brust, M.; Schiffrin, D. J.; Kiely, C. *J. Electroanal. Chem.* **1996**, *409*, 137.
(156) Brust, M.; Bethell, D.; Kiely, C. J.; Schiffrin, D. J. *Langmuir* **1998**, *14*, 5425.
(157) Hu, K.; Brust, M.; Bard, A. J. *Chem. Mater.* **1998**, *10*, 1160.
(158) Musick, M. D.; Keating, C. D.; Lyon, L. A.; Botsko, S. L.; Peña, D. J.; Holliway, W. D.; McEvoy, T. M.; Richardson, J. N.; Natan, M. J. *Chem. Mater.* **2000**, *12*, 2869.
(159) Fishelson, N.; Shkrob, I.; Lev, O.; Gun, J.; Modestov, A. D. *Langmuir* **2001**, *17*, 403.
(160) Snow, A. W.; Ancona, M. G.; Kruppa, W.; Jernigan, G. G.; Foos, E. E.; Park, D. *J. Mater. Chem.* **2002**, *12*, 1222.
(161) Trudeau, P.-E.; Orozco, A.; Kwan, E.; Dhirani, A.-A. *J. Chem. Phys.* **2002**, *117*, 3978.
(162) Trudeau, P.-E.; Escorcia, A.; Dhirani, A.-A. *J. Chem. Phys.* **2003**, *119*, 5267.
(163) Wessels, J. M.; Nothofer, H.-G.; Ford, W. E.; von Wrochem, F.; Scholz, F.; Vossmeyer, T.; Schroedter, A.; Weller, H.; Yasuda, A. *J. Am. Chem. Soc.* **2004**, *126*, 3349.
(164) Dunford, J. L.; Suganuma, Y.; Dhirani, A.-A.; Statt, B. *Phys. Rev. B* **2005**, *72*, 075441.
(165) Dunford, J. L.; Dhirani, A.-A.; Statt, B. *Phys. Rev. B* **2006**, *74*, 115417.
(166) Zabet-Khosousi, A.; Trudeau, P.-E.; Suganuma, Y.; Dhirani, A.-A.; Statt, B. *Phys. Rev. Lett.* **2006**, *96*, 156403.
(167) Pełka, J. B.; Brust, M.; Gierłowski, P.; Paszkowicz, W.; Schell, N. *Appl. Phys. Lett.* **2006**, *89*, 063110.
(168) Zamborini, F. P.; Hicks, J. F.; Murray, R. W. *J. Am. Chem. Soc.* **2000**, *122*, 4514.
(169) Templeton, A. C.; Zamborini, F. C.; Wuelfing, W. P.; Murray, R. W. *Langmuir* **2000**, *16*, 6682.
(170) Hicks, J. F.; Zamborini, F. P.; Osisek, A. J.; Murray, R. W. *J. Am. Chem. Soc.* **2001**, *123*, 7048.
(171) Wuelfing, W. P.; Zamborini, F. C.; Templeton, A. C.; Wen, X.; Yoon, H.; Murray, R. W. *Chem. Mater.* **2001**, *13*, 87.
(172) Zamborini, F. P.; Leopold, M. C.; Hicks, J. C.; Kulesza, P. J.; Malik, M. A.; Murray, R. W. *J. Am. Chem. Soc.* **2002**, *124*, 8958.
(173) Zamborini, F. P.; Smart, L. E.; Leopold, M. C.; Murray, R. W. *Anal. Chim. Acta* **2003**, *496*, 3.
(174) Chen, S. *Langmuir* **2001**, *17*, 2878.
(175) Doty, R. C.; Yu, H.; Shih, C. K.; Korgel, B. A. *J. Phys. Chem. B* **2001**, *105*, 8291.
(176) Snow, A. W.; Wohltjen, H. *Chem. Mater.* **1998**, *10*, 947.
(177) Klein, D. L.; McEuen, P. L.; Katari, J. E. B.; Roth, R.; Alivisatos, A. P. *Appl. Phys. Lett.* **1996**, *68*, 2574.
(178) Klein, D. L.; Roth, R.; Lim, A. K. L.; Alivisatos, A. P.; McEuen, P. L. *Nature* **1997**, *389*, 699.
(179) Sato, T.; Ahmed, H. *Appl. Phys. Lett.* **1997**, *70*, 2759.
(180) Sato, T.; Ahmed, H.; Brown, D.; Johnson, B. F. G. *J. Appl. Phys.* **1997**, *82*, 696.
(181) Bezryadin, A.; Dekker, C.; Schmid, G. *Appl. Phys. Lett.* **1997**, *71*, 1273.
(182) Persson, S. H. M.; Olofsson, L.; Gunnarsson, L. *Appl. Phys. Lett.* **1999**, *74*, 2546.
(183) Amlani, I.; Rawlett, A. M.; Nagahara, L. A.; Tsui, R. K. *Appl. Phys. Lett.* **2002**, *80*, 2761.
(184) Beecher, P.; Quinn, A. J.; Shevchenko, E. V.; Weller, H.; Redmond, G. *J. Phys. Chem. B* **2004**, *108*, 9564.
(185) Dadosh, T.; Gordin, Y.; Krahne, R.; Khivrich, I.; Mahalu, D.; Frydman, V.; Sperling, J.; Yacoby, A.; Bar-Joseph, I. *Nature* **2005**, *17*, 3333.
(186) Xu, C.; van Zalinge, H.; Pearson, J. L.; Glidle, A.; Cooper, J. M.; Cumming, D. R. S.; Haiss, W.; Schiffrin, D. J.; Proupín-Pérez, M.; Cosstick, R.; Nichols, R. J. *Nanotechnology* **2006**, *17*, 3333.
(187) Weiss, D. N.; Brokmann, X.; Calvet, L. E.; Kastner, M. A.; Bawendi, M. G. *Appl. Phys. Lett.* **2006**, *88*, 143507.
(188) Zhou, C.; Muller, C. J.; Deshpande, M. R.; Sleight, J. W.; Reed, M. A. *Appl. Phys. Lett.* **1995**, *67*, 1160.
(189) Reed, M. A.; Zhou, C.; Muller, C. J.; Burgin, T. P.; Tour, J. M. *Science* **1997**, *278*, 252.
(190) Smit, R. H. M.; Noat, Y.; Untiedt, C.; Lang, N. D.; van Hemert, M. C.; van Ruitenbeek, J. M. *Nature* **2002**, *419*, 906.
(191) Champagne, A. R.; Pasupathy, A. N.; Ralph, D. C. *Nano Lett.* **2005**, *5*, 305.
(192) Park, H.; Lim, A. K. L.; Alivisatos, A. P.; Park, J.; McEuen, P. L. *Appl. Phys. Lett.* **1999**, *75*, 301.
(193) Khondaker, S. I.; Yao, Z. *Appl. Phys. Lett.* **2002**, *81*, 4613.
(194) Lambert, M. F.; Goffman, M. F.; Bourgoin, J. P.; Hesto, P. *Nanotechnology* **2003**, *14*, 772.
(195) Bolotin, K. I.; Kuemmeth, F.; Pasupathy, A. N.; Ralph, D. C. *Appl. Phys. Lett.* **2004**, *84*, 3154.
(196) Strachan, D. R.; Smith, D. E.; Johnston, D. E.; Park, T.-H.; Therien, M. J.; Bonnell, D. A.; Johnson, A. T. *Appl. Phys. Lett.* **2005**, *86*, 043109.
(197) Zabet-Khosousi, A.; Suganuma, Y.; Lopata, K.; Trudeau, P.-E.; Dhirani, A.-A.; Statt, B. *Phys. Rev. Lett.* **2005**, *94*, 096801.
(198) Ghosh, S.; Halimun, H.; Mahapatro, A. K.; Choi, J.; Lodha, S.; Janes, D. *Appl. Phys. Lett.* **2005**, *87*, 233509.
(199) van der Zant, H. S. J.; Osorio, E. A.; Poot, M.; O'Neill, K. *Phys. Status Solidi B* **2006**, *243*, 3408.
(200) Strachan, D. R.; Smith, D. E.; Fischbein, M. D.; Johnston, D. E.; Guiton, B. S.; Drndiæ, M.; Bonnell, D. A.; Johnson, A. T. *Nano Lett.* **2006**, *6*, 441.
(201) Zabet-Khosousi, A.; Dhirani, A.-A. *Nanotechnology* **2007**, *18*, 455305.
(202) Heersche, H. B.; Lientschnig, G.; O'Neill, K.; van der Zant, H. S. J.; Zandbergen, H. W. *Appl. Phys. Lett.* **2007**, *91*, 072107.
(203) Hadeed, F. O.; Durkan, C. *Appl. Phys. Lett.* **2007**, *91*, 123120.
(204) Taychatanapat, T.; Bolotin, K. I.; Kuemmeth, F.; Ralph, D. C. *Nano Lett.* **2007**, *7*, 652.
(205) Chen, F.; Hihtath, J.; Huang, Z.; Li, X.; Tao, N. J. *Annu. Rev. Phys. Chem.* **2007**, *58*, 535.
(206) Musick, M. D.; Keating, C. D.; Keefe, M. H.; Natan, M. J. *Chem. Mater.* **1997**, *9*, 1499.
(207) Torma, V.; Vidoni, O.; Simon, U.; Schmid, G. *Eur. J. Inorg. Chem.* **2003**, 1121.
(208) Bonnell, D. A. Basic Principles of Scanning Probe Microscopy. In *Scanning Probe Microscopy and Spectroscopy: Theory, Techniques and Applications*; Bonnell, D. A., Ed.; Wiley: New York, 2001; p 7.
(209) Kelley, T. W.; Granstrom, E. L.; Frisbie, C. D. *Adv. Mater.* **1999**, *11*, 261.
(210) Wold, D. J.; Frisbie, C. D. *J. Am. Chem. Soc.* **2000**, *122*, 2970.
(211) Huang, S.; Tsutsui, G.; Sakaue, H.; Shingubara, S.; Takahagi, T. *J. Vac. Sci. Technol., B* **2000**, *18*, 2653.
(212) Alperson, B.; Cohen, S.; Rubinstein, I.; Hodes, G. *Phys. Rev. B* **1995**, *52*, R17017.
(213) Dai, H.; Wong, E. W.; Lieber, C. M. *Science* **1996**, *272*, 523.
(214) Cui, X. D.; Primak, A.; Zarate, X.; Tomfohr, J.; Sankey, O. F.; Moore, A. L.; Moore, T. A.; Gust, D.; Harris, G.; Lindsay, S. M. *Science* **2001**, *294*, 571.
(215) Cui, X. D.; Primak, A.; Zarate, X.; Tomfohr, J.; Sankey, O. F.; Moore, A. L.; Moore, T. A.; Gust, D.; Nagahara, L. A.; Lindsay, S. M. *J. Phys. Chem. B* **2002**, *106*, 8609.

(216) Kim, B.; Beebe, J. M.; Jun, Y.; Zhu, X.-Y.; Frisbie, C. D. *J. Am. Chem. Soc.* **2006**, *128*, 4970.
(217) Wold, D. J.; Frisbie, C. D. *J. Am. Chem. Soc.* **2001**, *123*, 5549.
(218) Wold, D. J.; Haag, R.; Rampi, M. A.; Frisbie, C. D. *J. Phys. Chem. B* **2002**, *106*, 2813.
(219) Engelkes, V. B.; Beebe, J. M.; Frisbie, C. D. *J. Am. Chem. Soc.* **2004**, *126*, 14287.
(220) Bard, A. J. In *Scanning Electrochemical Microscopy*; Bard, A. J., Mirkin, M. V., Eds.; Dekker: New York, 2001; p 1.
(221) Quinn, B. M.; Prieto, I.; Haram, S. K.; Bard, A. J. *J. Phys. Chem. B* **2001**, *105*, 7474.
(222) Bard, A. J.; Denuault, G.; Lee, C.; Mandler, D.; Wipf, D. O. *Acc. Chem. Res.* **1990**, *23*, 357.
(223) Abeles, B.; Sheng, P.; Coutts, M. D.; Arie, Y. *Adv. Phys.* **1975**, *24*, 407.
(224) Morris, J. E.; Coutts, T. J. *Thin Solid Films* **1977**, *47*, 3.
(225) Vanmaekelbergh, D.; Liljeroth, P. *Chem. Soc. Rev.* **2005**, *34*, 299.
(226) Simmons, J. G. *J. Appl. Phys.* **1963**, *34*, 1793.
(227) Duke, C. B. In *Tunneling Phenomena in Solids*; Burstein, E., Lundqvist, S., Eds.; Plenum: New York, 1969; p 31.
(228) Ingold, G.-L.; Nazarov, Y. V. Charge Tunneling Rates in Ultrasmall Junctions. In *Single Charge Tunneling*; Grabert, H., Devoret, M. H., Eds.; Plenum: New York, 1992; p 21.
(229) Simmons, J. G. *J. Appl. Phys.* **1964**, *35*, 2472.
(230) Salomon, A.; Cahen, D.; Lindsay, S.; Tomfohr, J.; Engelkes, V. B.; Frisbie, C. D. *Adv. Mater.* **2003**, *15*, 1881.
(231) Tao, N. J. *Nature Nano.* **2006**, *1*, 173.
(232) Nitzan, A. *Annu. Rev. Phys. Chem.* **2001**, *52*, 681.
(233) Datta, S. *Nanotechnology* **2004**, *15*, S433.
(234) Xue, Y.; Ranter, M. A. *Int. J. Quantum Chem.* **2005**, *102*, 911.
(235) Selzer, Y.; Allara, D. L. *Annu. Rev. Phys. Chem.* **2006**, *57*, 593.
(236) Newton, M. D. *Chem. Rev.* **1991**, *91*, 767.
(237) McConnell, H. M. *J. Chem. Phys.* **1961**, *35*, 508.
(238) Nitzan, A. *J. Phys. Chem. A* **2001**, *105*, 2677.
(239) Smalley, J. F.; Feldberg, S. W.; Chidsey, C. E. D.; Linford, M. R.; Newton, M. D.; Liu, Y.-P. *J. Phys. Chem.* **1995**, *99*, 13141.
(240) Wuelfing, W. P.; Murray, R. W. *J. Phys. Chem. B* **2002**, *106*, 3139.
(241) Nitzan, A.; Ranter, M. A. *Science* **2003**, *300*, 1384.
(242) Metzger, R. M. *Chem. Rev.* **2003**, *103*, 3803.
(243) McCreery, R. L. *Chem. Mater.* **2004**, *16*, 4477.
(244) Averin, D. V.; Likharev, K. K. In *Mesoscopic Phenomena in Solids*; Altshuler, B. L., Lee, P. A., Webb R. A., Eds.; Elsevier: Amsterdam, 1991; p 173.
(245) Amman, M.; Wilkins, R.; Ben-Jacob, E.; Maker, P. D.; Jaklevic, R. C. *Phys. Rev. B* **1991**, *43*, 1146.
(246) Hanna, A. E.; Tinkham, M. *Phys. Rev. B* **1991**, *44*, 5919.
(247) Wilkins, R.; Ben-Jacob, E.; Jaklevic, R. C. *Phys. Rev. Lett.* **1989**, *63*, 801.
(248) Black, C. T.; Tuominen, M. T.; Tinkham, M. *Phys. Rev. B* **1994**, *50*, 7888.
(249) Dorogi, M.; Gomez, J.; Osifchin, R.; Andres, P. R.; Reinfenberger, R. *Phys. Rev. B* **1995**, *52*, 9071.
(250) Andres, R. P.; Bein, T.; Dorogi, M.; Feng, S.; Henderson, J. I.; Kubiak, C. P.; Mahoney, W. J.; Osifchin, R. G.; Reifenberger, R. *Science* **1996**, *272*, 1323.
(251) Harrell, L. E.; Bigioni, T. P.; Cullen, W. G.; Whetten, R. L.; First, P. N. *J. Vac. Sci. Technol., B* **1999**, *17*, 2411.
(252) Jiang, P.; Liu, Z. F.; Cai, S. M. *Appl. Phys. Lett.* **1999**, *75*, 3023.
(253) Thomas, P. J.; Kulkarni, G. U.; Rao, C. N. R. *Chem. Phys. Lett.* **2000**, *321*, 163.
(254) Graf, H.; Vancea, J.; Hoffmann, H. *Appl. Phys. Lett.* **2002**, *80*, 1264.
(255) Suganuma, Y.; Trudeau, P.-E.; Dhirani, A.-A. *Phys. Rev. B* **2002**, *66*, 241405.
(256) Suganuma, Y.; Trudeau, P.-E.; Dhirani, A.-A.; Leathem, B.; Shieh, B. *J. Chem. Phys.* **2003**, *118*, 9769.
(257) Bigioni, T. P.; Schaaff, T. G.; Wyrwas, R. B.; Harrell, L. E.; Whetten, R. L.; First, P. N. *J. Phys. Chem. B* **2004**, *108*, 3772.
(258) Yang, G.; Tan, L.; Yang, Y.; Chen, S.; Liu, G.-Y. *Surf. Sci.* **2005**, *589*, 129.
(259) Jacobsen, V.; Zhu, T.; Knoll, W.; Kreiter, M. *Eur. J. Inorg. Chem.* **2005**, 3683.
(260) Fan, F.-R. F.; Bard, A. J. *Science* **1997**, *277*, 1791.
(261) Ingram, R. S.; Hostetler, M. J.; Murray, R. W.; Schaaff, T. G.; Khoury, J. T.; Whetten, R. L.; Bigioni, T. P.; Guthrie, D. K.; First, P. N. *J. Am. Chem. Soc.* **1997**, *119*, 9279.
(262) Chen, S.; Ingram, R. S.; Hostetler, M. J.; Pietron, J. J.; Murray, R. W.; Schaaff, T. G.; Khoury, J. T.; Alvarez, M. M.; Whetten, R. L. *Science* **1998**, *280*, 2098.
(263) Wang, G. R.; Wang, L.; Rendeng, Q.; Wang, J.; Luo, J.; Zhong, C.-J. *J. Mater. Chem.* **2007**, *17*, 457.
(264) Marcus, R. A.; Sutin, N. *Biochim. Biophys. Acta* **1985**, *811*, 265.
(265) Marcus, R. A. *Angew. Chem., Int. Ed. Engl.* **1993**, *32*, 1111.
(266) Middleton, A. A.; Wingreen, N. S. *Phys. Rev. Lett.* **1993**, *71*, 3198.
(267) Cordan, A. S.; Goltzené, A.; Hervé, Y.; Mejias, M.; Vieu, C.; Launois, H. *J. Appl. Phys.* **1998**, *84*, 3756.
(268) Müller, H.-O.; Katayama, K.; Mizuta, H. *J. Appl. Phys.* **1998**, *84*, 5603.
(269) Cordan, A. S.; Leroy, Y.; Goltzené, A.; Pépin, A.; Vieu, C.; Mejias, M.; Launois, H. *J. Appl. Phys.* **2000**, *87*, 345.
(270) Johansson, J.; Haviland, D. B. *Phys. Rev. B* **2001**, *63*, 014201.
(271) Parthasarathy, R.; Lin, X.-M.; Jaeger, H. M. *Phys. Rev. Lett.* **2001**, *87*, 186807.
(272) Parthasarathy, R.; Lin, X.-M.; Elteto, K.; Rosenbaum, T. F.; Jaeger, H. M. *Phys. Rev. Lett.* **2004**, *92*, 076801.
(273) Lebreton, C.; Vieu, C.; Pépin, A.; Mejias, M.; Carcenac, F.; Jin, Y.; Launois, H. *Microelectron. Eng.* **1998**, *41/42*, 507.
(274) Clarke, L.; Wybourne, M. N.; Brown, L. O.; Hutchison, J. E.; Yan, M.; Cai, S. X.; Keana, J. F. W. *Semicond. Sci. Technol.* **1998**, *13*, A111.
(275) Ancona, M. G.; Kruppa, W.; Rendell, R. W.; Snow, A. W.; Park, D.; Boos, J. B. *Phys. Rev. B* **2001**, *64*, 033408.
(276) Ancona, M. G.; Kooi, S. E.; Kruppa, W.; Snow, A. W.; Foos, E. E.; Whitman, L. J.; Park, D.; Shirley, L. *Nano Lett.* **2003**, *3*, 135.
(277) Devoret, M. H.; Grabert, H. Introduction to Single Charge Tunneling. In *Single Charge Tunneling*; Grabert, H., Devoret, M. H., Eds.; Plenum: New York, 1992; p 1.
(278) Orr, B. G.; Jaeger, H. M.; Kuper, C. G. *Phys. Rev. Lett.* **1986**, *56*, 378.
(279) Geerligs, L. J.; Mooij, J. E. *Physica B* **1988**, *152*, 212.
(280) Geerligs, L. J.; Anderegg, V. F.; van der Jeugd, C. A.; Romijn, J.; Mooij, J. E. *Europhys. Lett.* **1989**, *10*, 79.
(281) Liu, H.; Mun, B. S.; Thornton, G.; Isaacs, S. R.; Shon, Y.-S.; Ogletree, D. F.; Salmeron, M. *Phys. Rev. B* **2005**, *72*, 155430.
(282) Collier, C. P.; Saykally, R. J.; Shiang, J. J.; Henrichs, S. E.; Heath, J. R. *Science* **1997**, *277*, 1978.
(283) Shiang, J. J.; Heath, J. R.; Collier, C. P.; Saykally, R. J. *J. Phys. Chem. B* **1998**, *102*, 3425.
(284) Henrichs, S.; Collier, C. P.; Saykally, R. J.; Shen, Y. R.; Heath, J. R. *J. Am. Chem. Soc.* **2000**, *122*, 4077.
(285) Artemyev, M. V.; Bibik, A. I.; Gurinovich, L. I.; Gaponenko, S. V.; Woggon, U. *Phys. Rev. B* **1999**, *60*, 1504.
(286) Artemyev, M. V.; Woggon, U.; Jaschinski, H.; Gurinovich, L. I.; Gaponenko, S. V. *J. Phys. Chem. B* **2000**, *104*, 11619.
(287) Ashcroft, N. W.; Mermin, N. D. *Solid State Physics*; Saunders College: Philadelphia, PA, 1976.
(288) Mott, N. F. *Proc. R. Soc. London, Ser. A* **1982**, *382*, 1.
(289) Mott, N. F. *Adv. Phys.* **1972**, *21*, 785.
(290) Kittel, C. *Introduction to Solid State Physics*; Wiley: New York, 1996; p 284.
(291) Wang, W.; Lee, T.; Reed, M. A. *J. Phys. Chem. B* **2004**, *108*, 18398.
(292) Kirkpatrick, S. *Rev. Mod. Phys.* **1973**, *45*, 574.
(293) Pury, P. A.; Caceres, M. O. *Phys. Rev. B* **1997**, *55*, 3841.
(294) White, G. K.; Woods, S. B. *Philos. Trans. R. Soc. London, Ser. A* **1959**, *251*, 273.
(295) Crowell, C. R.; Sze, S. M. *Phys. Rev. Lett.* **1965**, *15*, 659.
(296) Tran, T. B.; Beloborodov, I. S.; Lin, X. M.; Bigioni, T. P.; Vinokur, V. M.; Jaeger, H. M. *Phys. Rev. Lett.* **2005**, *95*, 076806.
(297) Liao, Z.-M.; Xun, J.; Yu, D.-P. *Phys. Lett. A* **2005**, *345*, 386.
(298) Rafiq, M. A.; Tsuchiya, Y.; Mizuta, H.; Oda, S.; Uno, S.; Durrani, Z. A. K.; Milne, W. I. *J. Appl. Phys.* **2006**, *100*, 014303.
(299) Sheng, P.; Abeles, B.; Arie, Y. *Phys. Rev. Lett.* **1973**, *31*, 44.
(300) Chui, T.; Deutscher, G.; Lindenfeld, P.; McLean, W. L. *Phys. Rev. B* **1981**, *23*, 6172.
(301) Entin-Wohlman, O.; Gefen, Y.; Shapira, Y. *J. Phys. C* **1983**, *16*, 1161.
(302) Gerber, A.; Milner, A.; Deutscher, G.; Karpovsky, M.; Gladkikh, A. *Phys. Rev. Lett.* **1997**, *78*, 4277.
(303) Mandal, S. K.; Gangopadhyay, A.; Chaudhuri, S.; Pal, A. K. *Vacuum* **1999**, *52*, 485.
(304) Yakimov, A. I.; Dvurechenskii, A. V.; Kirienko, V. V.; Yakovlev, Y. I.; Nikiforov, A. I.; Adkins, C. J. *Phys. Rev. B* **2000**, *61*, 10868.
(305) Bera, S. K.; Chaudhuri, S.; Pal, A. K. *Thin Solid Films* **2002**, *415*, 68.
(306) Mott, N. F. *J. Non-Cryst. Solids* **1968**, *1*, 1.
(307) Ambegaokar, V.; Halperin, B. I.; Langer, J. S. *Phys. Rev. B* **1971**, *4*, 2612.
(308) Efros, A. L.; Shklovskii, B. I. *J. Phys. C* **1975**, *8*, L49.
(309) Massey, J. G.; Lee, M. *Phys. Rev. Lett.* **1995**, *75*, 4266.
(310) Shklovskii, B. I.; Efros, A. L. *Electronic Properties of Doped Semiconductors*; Springer-Verlag: Berlin, 1984.
(311) Adkins, C. J. *J. Phys. C* **1989**, *1*, 1253.
(312) Sheng, P. *Philos. Mag. B* **1992**, *65*, 357.
(313) Pollak, M.; Adkins, C. J. *Philos. Mag. B* **1992**, *65*, 855.
(314) Zhang, J.; Shklovskii, B. I. *Phys. Rev. B* **2004**, *70*, 115317.
(315) Beloborodov, I. S.; Lopatin, A. V.; Vinokur, V. M. *Phys. Rev. B* **2005**, *72*, 125121.

(316) Feigel'man, M. V.; Ioselevich, A. S. *Pis'ma Zh. Eksp. Teor. Fiz.* **2005**, *81*, 341. [*JETP Lett.* **2005**, *81*, 227]
(317) Beloborodov, I. S.; Glatz, A.; Vinokur, V. M. *Phys. Rev. B* **2007**, *75*, 052302.
(318) Beloborodov, I. S.; Lopatin, A. V.; Vinokur, V. M.; Efetov, K. B. *Rev. Mod. Phys.* **2007**, *79*, 469.
(319) Averin, D. V.; Nazarov, Y. V. *Phys. Rev. Lett.* **1990**, *65*, 2446.
(320) Pollak, M. *J. Non-Cryst. Solids* **1972**, *11*, 1.
(321) Šimánek, E. *Solid State Commun.* **1981**, *40*, 1021.
(322) Sheng, P.; Klafter, J. *Phys. Rev. B* **1983**, *27*, 2583.
(323) Lin, C.-H.; Wu, G. Y. *Physica B* **2000**, *279*, 341.
(324) Quinn, B. M.; Liljeroth, P.; Ruiz, V.; Laaksonen, T.; Kontturi, K. *J. Am. Chem. Soc.* **2003**, *125*, 6644.
(325) Green, S. J.; Stokes, J. J.; Hostetler, M. J.; Pietron, J.; Murray, R. W. *J. Phys. Chem. B* **1997**, *101*, 2663.
(326) Green, S. J.; Pietron, J. J.; Stokes, J. J.; Hostetler, M. J.; Vu, H.; Wuelfing, W. P.; Murray, R. W. *Langmuir* **1998**, *14*, 5612.
(327) Miles, D. T.; Murray, R. W. *Anal. Chem.* **2001**, *73*, 921.
(328) Miles, D. T.; Leopold, M. C.; Hicks, J. F.; Murray, R. W. *J. Electroanal. Chem.* **2003**, *554*, 87.
(329) Chen, S.; Murray, R. W.; Feldberg, S. W. *J. Phys. Chem. B* **1998**, *102*, 9898.
(330) Pietron, J. J.; Hicks, J. F.; Murray, R. W. *J. Am. Chem. Soc.* **1999**, *121*, 5565.
(331) Cheng, W.; Dong, S.; Wang, E. *Electrochem. Commun.* **2002**, *4*, 412.
(332) Chen, S.; Huang, K.; Stearns, J. A. *Chem. Mater.* **2000**, *12*, 540.
(333) Kim, Y.-G.; Garcia-Martinez, J. C.; Crooks, R. M. *Langmuir* **2005**, *21*, 5485.
(334) Chen, S.; Sommers, J. M. *J. Phys. Chem. B* **2001**, *105*, 8816.
(335) Kakade, B. A.; Shintri, S. S.; Sathe, B. R.; Halligudi, S. B.; Pillai, V. K. *Adv. Mater.* **2007**, *19*, 272.
(336) Ding, Z.; Quinn, B. M.; Haram, S. K.; Pell, L. E.; Korgel, B. A.; Bard, A. J. *Science* **2002**, *296*, 1293.
(337) Chen, S.; Truax, L. A.; Sommers, J. M. *Chem. Mater.* **2000**, *12*, 3864.
(338) Haram, S. K.; Quinn, B. M.; Bard, A. J. *J. Am. Chem. Soc.* **2001**, *123*, 8860.
(339) Bard, A. J.; Ding, Z.; Myung, N. *Struct. Bonding* **2005**, *118*, 1.
(340) Hicks, J. F.; Templeton, A. C.; Chen, S.; Sheran, K. M.; Jasti, R.; Murray, R. W.; Debord, J.; Schaaff, T. G.; Whetten, R. L. *Anal. Chem.* **1999**, *71*, 3703.
(341) Guo, R.; Murray, R. W. *J. Am. Chem. Soc.* **2005**, *127*, 12140.
(342) Guo, R.; Georganopoulou, D.; Feldberg, S. W.; Donkers, R.; Murray, R. W. *Anal. Chem.* **2005**, *77*, 2662.
(343) Miles, D. T.; Murray, R. W. *Anal. Chem.* **2003**, *75*, 1251.
(344) Garcia-Morales, V.; Mafé, S. *J. Phys. Chem. C* **2007**, *111*, 7242.
(345) Lee, D.; Donkers, R. L.; Wang, G.; Harper, A. S.; Murray, R. W. *J. Am. Chem. Soc.* **2004**, *126*, 6193.
(346) Jimenez, V. L.; Georganopoulou, D. G.; White, R. J.; Harper, A. S.; Mills, A. J.; Lee, D. I.; Murray, R. W. *Langmuir* **2004**, *20*, 6864.
(347) Tracy, J. B.; Kalyuzhny, G.; Crowe, M. C.; Balasubramanian, R.; Choi, J. P.; Murray, R. W. *J. Am. Chem. Soc.* **2007**, *129*, 6706.
(348) Chen, S.; Murray, R. W. *J. Phys. Chem. B* **1999**, *103*, 9996.
(349) Chen, S. *J. Phys. Chem. B* **2000**, *104*, 663.
(350) Chen, S. *J. Am. Chem. Soc.* **2000**, *122*, 7420.
(351) Chen, S.; Pei, R. *J. Am. Chem. Soc.* **2001**, *123*, 10607.
(352) Hicks, J. F.; Zamborini, F. P.; Murray, R. W. *J. Phys. Chem. B* **2002**, *106*, 7751.
(353) Chen, S.; Deng, F. *Langmuir* **2002**, *18*, 8942.
(354) Yang, Y.; Pradhan, S.; Chen, S. *J. Am. Chem. Soc.* **2004**, *126*, 76.
(355) Kim, J.; Lee, D. *J. Am. Chem. Soc.* **2006**, *128*, 4518.
(356) Chen, S.; Pei, R.; Zhao, T.; Dyer, D. J. *J. Phys. Chem. B* **2002**, *106*, 1903.
(357) Hicks, J. F.; Seok-Shon, Y.; Murray, R. W. *Langmuir* **2002**, *18*, 2288.
(358) Brennan, J. L.; Branham, M. R.; Hicks, J. F.; Osisek, A. J.; Donkers, R. L.; Georganopoulou, D. G.; Murray, R. W. *Anal. Chem.* **2004**, *76*, 5611.
(359) Deng, F.; Chen, S. *Phys. Chem. Chem. Phys.* **2005**, *7*, 3375.
(360) Choi, J.-P.; Murray, R. W. *J. Am. Chem. Soc.* **2006**, *128*, 10496.
(361) Boettchier, S. W.; Strandwitz, N. C.; Schierhorn, M.; Lock, N.; Lonergan, M. C.; Stucky, G. D. *Nat. Mater.* **2007**, *6*, 592.
(362) Finklea, H. O.; Snider, D. A.; Fedyk, J.; Sabatani, E.; Gafni, Y.; Rubinstein, I. *Langmuir* **1993**, *9*, 3660.
(363) Cheng, W.; Dong, S.; Wang, E. *Langmuir* **2002**, *18*, 9947.
(364) Zhong, C.-J.; Zheng, W. X.; Leibowitz, F. L. *Electrochem. Commun.* **1999**, *1*, 72.
(365) Porter, M. D.; Bright, T. B.; Allara, D. L.; Chidsey, C. E. *J. Am. Chem. Soc.* **1987**, *109*, 3559.
(366) Brown, K. R.; Fox, A. P.; Natan, M. J. *J. Am. Chem. Soc.* **1996**, *118*, 1154.
(367) Baum, T.; Bethell, D.; Brust, M.; Schiffrin, D. J. *Langmuir* **1999**, *15*, 866.
(368) Musick, M. D.; Peña, D. J.; Botsko, S. L.; McEvoy, T. M.; Richardson, J. N.; Natan, M. J. *Langmuir* **1999**, *15*, 844.
(369) Bharathi, S.; Nogami, M.; Ikeda, S. *Langmuir* **2001**, *17*, 1.
(370) Lu, M.; Li, X. H.; Yu, B. Z.; Li, H. L. *J. Colloid Interface Sci.* **2002**, *248*, 376.
(371) Cheng, W.; Dong, S.; Wang, E. *Anal. Chem.* **2002**, *74*, 3599.
(372) Kariuki, N. N.; Luo, J.; Han, L.; Maye, M. M.; Moussa, L.; Patterson, M.; Lin, Y.; Engelhard, M. H.; Zhong, C.-J. *Electroanalysis* **2004**, *16*, 120.
(373) Stolarczyk, K.; Bilewicz, R. *Electrochim. Acta* **2006**, *51*, 2358.
(374) Tian, R.; Rao, T. N.; Einaga, Y.; Zhi, J. *Chem. Mater.* **2006**, *18*, 939.
(375) Bard, A. J.; Faulkner, L. R. *Electrochemical Methods*; Wiley: New York, 1980.
(376) Nicholson, R. S. *Anal. Chem.* **1965**, *37*, 1351.
(377) Horswell, S. L.; O'Niel, I. A.; Schiffrin, D. J. *J. Phys. Chem. B* **2003**, *107*, 4844.
(378) Zhang, J.; Kambayashi, M.; Oyama, M. *Electrochem. Commun.* **2004**, *6*, 683.
(379) Zhang, J.; Kambayashi, M.; Oyama, M. *Electroanalysis* **2005**, *17*, 408.
(380) Zhang, J.; Oyama, M. *Anal. Chim. Acta* **2005**, *540*, 299.
(381) Willner, I.; Katz, E. *Angew. Chem., Int. Ed.* **2000**, *39*, 1180.
(382) Armstrong, F. A.; Wilson, G. S. *Electrochim. Acta* **2000**, *45*, 2623.
(383) Zhang, S.; Yang, W.; Niu, Y.; Sun, C. *Sens. Actuators, B* **2004**, *101*, 387.
(384) Nakai, H.; Yoshihara, M.; Fujihara, H. *Langmuir* **1999**, *15*, 8574.
(385) Cheng, W.; Jiang, J.; Dong, S.; Wang, E. *Chem. Commun.* **2002**, 1706.
(386) Peerce, P. J.; Bard, A. J. *J. Electroanal. Chem.* **1980**, *114*, 89.
(387) Laviron, E. *J. Electroanal. Chem.* **1979**, *191*, 19.
(388) Seydack, M. *Biosens. Bioelectron.* **2005**, *20*, 2454.
(389) Franke, M. E.; Koplin, T. J.; Simon, U. *Small* **2006**, *2*, 301.
(390) Wohltjen, H.; Snow, A. W. *Anal. Chem.* **1998**, *70*, 2856.
(391) Foos, E. E.; Snow, A. W.; Twigg, M. E.; Ancona, M. G. *Chem. Mater.* **2002**, *14*, 2401.
(392) Grate, J. W.; Nelson, D. A.; Skaggs, R. *Anal. Chem.* **2003**, *75*, 1868.
(393) Ahn, H.; Chandekar, A.; Kang, B.; Sung, C.; Whitten, J. E. *Chem. Mater.* **2004**, *16*, 3274.
(394) Kim, Y. J.; Yang, Y. S.; Ha, S.-C.; Cho, S. M.; Kim, Y. S.; Kim, H. Y.; Yang, H.; Kim, Y. T. *Sens. Actuators, B* **2005**, *106*, 189.
(395) Pang, P.; Guo, Z.; Cai, Q. *Talanta* **2005**, *65*, 1343.
(396) Ibañez, F. J.; Growrishetty, U.; Crain, M. M.; Walsh, K. M.; Zamborini, F. P. *Anal. Chem.* **2006**, *78*, 753.
(397) Ibañez, F. J.; Zamborini, F. P. *Langmuir* **2006**, *22*, 9789.
(398) Hanwell, M. D.; Heriot, S. Y.; Richardson, T. H.; Cowlam, N.; Ross, I. M. *Colloids Surf., A* **2006**, *284*, 379.
(399) Evans, S. D.; Johnson, S. R.; Cheng, Y. L.; Shen, T. *J. Mater. Chem.* **2000**, *10*, 183.
(400) Zhang, H.-L.; Evans, S. D.; Henderson, J. R.; Miles, R. E.; Shen, T.-H. *Nanotechnology* **2002**, *13*, 439.
(401) Yang, C.-Y.; Li, C.-L.; Lu, C.-J. *Anal. Chim. Acta* **2006**, *565*, 17.
(402) Briglin, S. M.; Gao, T.; Lewis, N. S. *Langmuir* **2004**, *20*, 299.
(403) Han, L.; Daniel, D. R.; Maye, M. M.; Zhong, C.-J. *Anal. Chem.* **2001**, *73*, 4441.
(404) Joseph, Y.; Besnard, I.; Rosenberger, M.; Guse, B.; Nothofer, H.-G.; Wessels, J. M.; Wild, U.; Knop-Gericke, A.; Su, D.; Schlogl, R.; Yasuda, A.; Vossmeyer, T. *J. Phys. Chem. B* **2003**, *107*, 7406.
(405) Joseph, Y.; Guse, B.; Yasuda, A.; Vossmeyer, T. *Sens. Actuators, B* **2004**, *98*, 188.
(406) Han, L.; Shi, X.; Wu, W.; Kirk, F. L.; Luo, J.; Wang, L.; Mott, D.; Cousineau, L.; Lim, S. I.-I.; Lu, S.; Zhong, C.-J. *Sens. Actuators, B* **2005**, *106*, 431.
(407) Pang, P.; Guo, Z.; Cai, Q. *Sens. Actuators, B* **2006**, *114*, 799.
(408) Wang, L.; Shi, X.; Kariuki, N. N.; Schadt, M.; Wang, G. R.; Rendeng, Q.; Choi, J.; Luo, J.; Lu, S.; Zhong, C.-J. *J. Am. Chem. Soc.* **2007**, *129*, 2161.
(409) Guo, J.; Pang, P.; Cai, Q. *Sens. Actuators, B* **2007**, *120*, 521.
(410) Leopold, M. C.; Donkers, R. L.; Georganopoulou, D.; Fisher, M.; Zamborini, F. P.; Murray, R. W. *Faraday Discuss.* **2004**, *125*, 63.
(411) Tognarelli, D. J.; Miller, R. B.; Pompano, R. R.; Loftus, A. F.; Sheibley, D. J.; Leopold, M. C. *Langmuir* **2005**, *21*, 11119.
(412) Singh, A.; Chaudhari, M.; Sastry, M. *Nanotechnology* **2006**, *17*, 2399.
(413) Joseph, Y.; Pieæ, A.; Chen, X.; Michl, J.; Vossmeyer, T.; Yasuda, A. *J. Phys. Chem. C* **2007**, *111*, 12855.
(414) Krasteva, N.; Krustev, R.; Yasuda, A.; Vossmeyer, T. *Langmuir* **2003**, *19*, 7754.
(415) Steinecker, W. H.; Rowe, M. P.; Zellers, E. T. *Anal. Chem.* **2007**, *79*, 4977.
(416) Cai, Q.-Y.; Zellers, E. T. *Anal. Chem.* **2002**, *74*, 3533.
(417) Luo, X.; Morrin, A.; Killard, A. J.; Smyth, M. R. *Electroanalysis* **2006**, *18*, 319.

(418) Astruc, D.; Lu, F.; Aranzaes, J. R. *Angew. Chem., Int. Ed.* **2005**, *44*, 7852.
(419) Abdelrahman, A. I.; Mohammad, A. M.; Okajima, T.; Ohsaka, T. *J. Phys. Chem. B* **2006**, *110*, 2798.
(420) Yu, A.; Liang, Z.; Cho, J.; Caruso, F. *Nano Lett.* **2003**, *3*, 1203.
(421) Raj, C. R.; Okajima, T.; Ohsaka, T. *J. Electroanal. Chem.* **2003**, *543*, 127.
(422) Wang, H.; Huang, Y.; Tan, Z.; Hu, X. *Anal. Chim. Acta* **2004**, *526*, 13.
(423) Goyal, R. N.; Gupta, V. K.; Oyama, M.; Bachheti, N. *Electrochem. Commun.* **2005**, *7*, 803.
(424) Fiorito, P. A.; Gonçales, V. R.; Ponzio, E. A.; de Torresi, S. I. C. *Chem. Commun.* **2005**, 366.
(425) Niemeyer, C. M. *Angew. Chem., Int. Ed.* **2001**, *40*, 4128.
(426) Liu, S.; Leech, D.; Ju, H. *Anal. Lett.* **2003**, *36*, 1.
(427) Wang, J. *Small* **2005**, *1*, 1036.
(428) Wang, J. *Electroanalysis* **2007**, *19*, 769.
(429) Medintz, I. L.; Uyeda, H. T.; Goldman, E. R.; Mattoussi, H. *Nat. Mater.* **2005**, *4*, 435.
(430) Niemeyer, C. M.; Simon, U. *Eur. J. Inorg. Chem.* **2005**, 3641.
(431) Castañeda, M. T.; Alegret, S.; Merkoçi, A. *Electroanalysis* **2007**, *19*, 743.
(432) Mirkin, C. A. *Inorg. Chem.* **2000**, *39*, 2258.
(433) Sassolas, A.; Leca-Bouvier, B. D.; Blum, L. J. *Chem. Rev.* **2008**, *108*, 109.
(434) Willner, I.; Basnar, B.; Willner, B. *FEBS J.* **2007**, *274*, 302.
(435) Wang, H.; Li, J.; Ding, Y.; Lei, C.; Shen, G.; Yu, R. *Anal. Chim. Acta* **2004**, *501*, 37.
(436) Wang, M.; Wang, L.; Yuan, H.; Ji, X.; Sun, C.; Ma, L.; Bai, Y.; Li, T.; Li, J. *Electroanalysis* **2004**, *16*, 757.
(437) Tang, D.; Yuan, R.; Chai, Y.; Zhang, L.; Dai, J.; Liu, Y.; Zhong, X. *Electroanalysis* **2005**, *17*, 155.
(438) Zhuo, Y.; Yuan, R.; Chai, Y.; Tang, D.; Zhang, Y.; Wang, N.; Li, X.; Zhu, Q. *Electrochem. Commun.* **2005**, *7*, 355.
(439) Wang, J.; Profitt, J. A.; Pugia, M. J.; Suni, I. I. *Anal. Chem.* **2006**, *78*, 1769.
(440) Crumbliss, A. L.; Perine, S. C.; Stonehuerner, J.; Tubergen, K. R.; Zhao, J.; Henkens, R. W.; O'Daly, J. P. *Biotechnol. Bioeng.* **1992**, *40*, 483.
(441) Zhao, J.; Henkens, R. W.; Stonehuerner, J.; O'Daly, J. P.; Crumbliss, A. L. *J. Electroanal. Chem.* **1992**, *327*, 109.
(442) Xiao, Y.; Ju, H.-X.; Chen, H.-Y. *Anal. Chim. Acta* **1999**, *391*, 73.
(443) Jia, J.; Wang, B.; Wu, A.; Cheng, G.; Li, Z.; Dong, S. *Anal. Chem.* **2002**, *74*, 2217.
(444) He, P.; He, N. *Electroanalysis* **2004**, *16*, 1122.
(445) Wang, L.; Wang, E. *Electrochem. Commun.* **2004**, *6*, 225.
(446) Zhang, Y.; He, P.; Hu, N. *Electrochim. Acta* **2004**, *49*, 1981.
(447) Xu, S.; Han, X. *Biosens. Bioelectron.* **2004**, *19*, 1117.
(448) Yuan, R.; Liu, Y.; Li, Q.-F.; Chai, Y.-A.; Mo, C.-L.; Zhong, X.; Tang, D.-P.; Dai, J.-Y. *Anal. Bioanal. Chem.* **2005**, *381*, 762.
(449) Luo, X.-L.; Xu, J.-J.; Zhang, Q.; Yang, G.-J.; Chen, H.-Y. *Biosens. Bioelectron.* **2005**, *21*, 190.
(450) Li, X.; Wu, J.; Gao, N.; Shen, G.; Yu, R. *Sens. Actuators, B* **2006**, *117*, 35.
(451) Chen, S.; Yuan, R.; Chai, Y.; Xu, L.; Wang, N.; Li, X.; Zhang, L. *Electroanalysis* **2006**, *18*, 471.
(452) Bharathi, S.; Nogami, M.; Lev, O. *Langmuir* **2001**, *17*, 2602.
(453) Bharathi, S.; Nogami, M. *Analyst* **2001**, *126*, 1919.
(454) Xiao, Y.; Patolsky, F.; Katz, E.; Hainfeld, J. F.; Willner, I. *Science* **2003**, *299*, 1877.
(455) You, T.; Niwa, O.; Tomita, M.; Hirono, S. *Anal. Chem.* **2003**, *75*, 2080.
(456) Liu, S.; Ju, H. *Biosens. Bioelectron.* **2003**, *19*, 177.
(457) Mena, M. L.; Yáñez-Sedeño, P.; Pingarrón, J. M. *Anal. Biochem.* **2005**, *336*, 20.
(458) Zhang, S.; Wang, N.; Yu, H.; Niu, Y.; Sun, C. *Bioelectrochemistry* **2005**, *67*, 15.
(459) Zhang, S.; Wang, N.; Niu, Y.; Sun, C. *Sens. Actuators, B* **2005**, *109*, 367.
(460) Zhang, S.; Yang, W.; Niu, Y.; Li, Y.; Zhang, M.; Sun, C. *Anal. Bioanal. Chem.* **2006**, *384*, 736.
(461) Yang, W.; Wang, J.; Zhao, S.; Sun, Y.; Sun, C. *Electrochem. Commun.* **2006**, *8*, 665.
(462) Zhao, S.; Zhang, K.; Bai, Y.; Yang, W.; Sun, C. *Bioelectrochemistry* **2006**, *69*, 158.
(463) Sun, Y.; Yan, F.; Yang, W.; Zhang, S.; Yang, W.; Sun, C. *Anal. Bioanal. Chem.* **2007**, *387*, 1565.
(464) Liu, T.; Zhong, J.; Gan, X.; Fan, C.; Li, G.; Matsuda, N. *Chem. Phys. Chem* **2003**, *4*, 1364.
(465) Wang, L.; Wang, E. *Electrochem. Commun.* **2004**, *6*, 49.
(466) Zhao, J.; O'Daly, J. P.; Henkens, R. W.; Stonehuerner, J.; Crumbliss, A. L. *Biosens. Bioelectron.* **1996**, *11*, 493.
(467) Gu, H.-Y.; Yu, A.-M.; Chen, H.-Y. *J. Electroanal. Chem.* **2001**, *516*, 119.
(468) Han, X.; Cheng, W.; Zhang, Z.; Dong, S.; Wang, E. *Biochim. Biophys. Acta* **2002**, *1556*, 273.
(469) Liu, S.; Ju, H. *Analyst* **2003**, *128*, 1420.
(470) Liu, S.; Dai, Z.; Chen, H.; Ju, H. *Biosens. Bioelectron.* **2004**, *19*, 963.
(471) Zhou, H.; Gan, X.; Liu, T.; Yang, Q.; Li, G. *J. Biochem. Biophys. Methods* **2005**, *64*, 38.
(472) Liu, S.; Ju, H. *Electroanalysis* **2003**, *15*, 1488.
(473) Gan, X.; Liu, T.; Zhong, J.; Liu, X.; Li, G. *ChemBioChem* **2004**, *5*, 1686.
(474) Zhang, H.; Lu, H.; Hu, N. *J. Phys. Chem. B* **2006**, *110*, 2171.
(475) Patolsky, F.; Gabriel, T.; Willner, I. *J. Electroanal. Chem.* **1999**, *479*, 69.
(476) Yabuki, S.; Mizutani, F. *Electroanalysis* **1997**, *9*, 23.
(477) Talapin, D. V.; Murray, C. B. *Science* **2005**, *310*, 86.
(478) Tucker, J. R. *J. Appl. Phys.* **1992**, *72*, 4399.
(479) Likharev, K. K. *Proc. IEEE* **1999**, *87*, 606.
(480) Goodnick, S. M.; Bird, J. *IEEE Trans. Nanotechnol.* **2003**, *2*, 368.
(481) Ono, Y.; Fujiwara, A.; Nishiguchi, K.; Inokawa, H.; Takahashi, Y. *J. Appl. Phys.* **2005**, *97*, 031101.
(482) Feldheim, D. L.; Keating, C. D. *Chem. Soc. Rev.* **1998**, *27*, 1.
(483) Borini, S.; Boarino, L.; Amato, G. *Adv. Mater.* **2006**, *18*, 2422.
(484) Kharitonov, A. B.; Shipway, A. N.; Willner, I. *Anal. Chem.* **1999**, *71*, 5441.
(485) Xu, J.-J.; Zhao, W.; Luo, X.-L.; Chen, H.-Y. *Chem. Commun.* **2005**, 792.
(486) Simon, U.; Flesch, R.; Wiggers, H.; Schön, G.; Schmid, G. *J. Mater. Chem.* **1998**, *8*, 517.

CR0680134